MASTER'S DISSERTATION

ANALYTICAL AND FINITE-ELEMENT MODELLING OF INTERNAL FLOW IN NON-CIRCULAR DUCTS

VINÍCIUS COUTINHO DA SILVA

Brasília, February 2026

UNIVERSIDADE DE BRASÍLIA

UNIVERSIDADE DE BRASÍLIA
FACULDADE DE TECNOLOGIA
DEPARTAMENTO DE ENGENHARIA MECÂNICA

ANALYTICAL AND FINITE-ELEMENT MODELLING OF INTERNAL FLOW IN NON-CIRCULAR DUCTS

VINÍCIUS COUTINHO DA SILVA

Advisor: PROF. DR. ANDRÉ VON BORRIES LOPES, UNB
Co-advisor: PROF. DR. FRANCISCO RICARDO CUNHA, UNB

DISSERTATION IN MECHANICAL SCIENCES

PUBLICATION ENM.PG - XXX/AAAA
BRASÍLIA, FEBRUARY 2026.

UNIVERSIDADE DE BRASÍLIA
FACULDADE DE TECNOLOGIA
DEPARTAMENTO DE ENGENHARIA MECÂNICA

ANALYTICAL AND FINITE-ELEMENT MODELLING OF INTERNAL FLOW IN NON-CIRCULAR DUCTS

VINÍCIUS COUTINHO DA SILVA

A DISSERTATION SUBMITTED TO THE DEPARTMENT OF MECHANICAL ENGINEERING OF UNIVERSITY OF BRASILIA, IN PARTIAL FULFILLMENT OF THE REQUIREMENTS FOR THE DEGREE OF MASTER OF SCIENCE IN MECHANICAL SCIENCES.

APPROVED BY:

Prof. Dr. André von Borries Lopes, UnB
Advisor

Prof. Dr. Francisco Ricardo Cunha, UnB
Co-Advisor

Prof. Dr. Eder Lima de Albuquerque, UnB
Internal Examiner

Prof. Dr. Roberto Carlos Moro Filho, UTFPR
External Examiner

BRASÍLIA, FEBRUARY 2026.

CARD CATALOG
VINÍCIUS COUTINHO DA SILVA
ANALYTICAL AND FINITE-ELEMENT MODELLING OF INTERNAL FLOW IN NON-CIRCULAR DUCTS
2026xv, 115p., 201x297 mm
(ENM/FT/UnB, MSc in Mechanical Sciences, Engenharia Mecânica, 2026)
Master's Dissertation - Universidade de Brasília
Faculdade de Tecnologia - Departamento de Engenharia Mecânica

BIBLIOGRAPHIC REFERENCE

VINÍCIUS COUTINHO DA SILVA (2026) ANALYTICAL AND FINITE-ELEMENT MODELLING OF INTERNAL FLOW IN NON-CIRCULAR DUCTS. Master's Dissertation em Engenharia Mecânica, Publicação xxx/AAAA, Departamento de Engenharia Mecânica, Universidade de Brasília, Brasília, DF, 115p.

ASSIGNMENT OF RIGHTS

AUTHOR: VINÍCIUS COUTINHO DA SILVA
TITLE: ANALYTICAL AND FINITE-ELEMENT MODELLING OF INTERNAL FLOW IN NON-CIRCULAR DUCTS.
DEGREE: MSc in Mechanical Sciences YEAR: 2026

_____

VINÍCIUS COUTINHO DA SILVA
viniciuscoutinho04@gmail.com

Agradecimentos

Agradeço a Deus. Pela vida, pela saúde, pela força nos momentos difíceis e também por me permitir exercer diariamente aquilo que escolhi com o coração, sendo feliz a cada passo e tendo ao meu lado pessoas que amo.

Aos meus pais, Azenilda e Francisco, minha mais profunda gratidão. Tudo o que sou e tudo o que alcancei é reflexo do que vocês me ensinaram e me proporcionaram ao longo da vida. Sei o quanto vocês se sacrificaram, e ainda se sacrificam, para nos oferecer sempre o melhor. Este trabalho também é de vocês. Amo vocês.

Aos meus irmãos Samuel, Diego e Fabiano. Agradeço pelo companheirismo e pelo apoio ao longo de toda essa jornada. Em especial, agradeço ao Diego, e sempre foi minha maior inspiração para que eu seguisse no meio acadêmico e me deu todo o apoio possível. Seu exemplo de paixão pelo conhecimento foi determinante para que eu escolhesse esse caminho. Muito da minha trajetória vem do suporte que você me deu. Muito obrigado.

À minha namorada, Juliana, agradeço pelo amor, pela paciência e pelo apoio diário, nada disso seria possível sem você. Sua presença faz meus dias melhores e minhas conquistas mais felizes. Te amo cada dia mais, meu amor.

Aos meus sogros, Marcelo e Marlene, agradeço pelo carinho, pelo acolhimento e pelo apoio sincero. Obrigado por torcerem por mim e por estarem presentes em cada passo dessa caminhada.

Aos meus amigos, deixo meu agradecimento pela amizade, pelas conversas, pelas risadas e pelo apoio em cada etapa dessa trajetória. Cada um de vocês teve sua importância e parte fundamental na minha vida. Porque cada incentivo e cada momento compartilhado contribuíram, de alguma forma, para que esta jornada fosse possível.

Por último, mas não menos importante, agradeço ao André. O título de orientador é apenas para formalizar um papel acadêmico, mas ele está longe de descrever a nossa amizade e colaboração. Desde os primeiros passos no PIBIC até o nosso primeiro artigo, obrigado pela confiança, pela liberdade, intelectual, de trabalho e de caminho, e por sempre acreditar. Obrigado pelas conversas francas, pelas dicas, pelas viagens e até pelos shows de rock.

Resumo

A análise do escoamento laminar interno em dutos é um tema central da engenharia, com implicações práticas e teóricas. Embora o avanço de métodos numéricos e do poder computacional tenha impulsionado referências numéricas de alta precisão, ainda persistem lacunas na literatura analítica para geometrias específicas. Esta dissertação contribui para esse cenário ao desenvolver novos resultados e metodologias para os escoamentos de Poiseuille e Darcy–Brinkman, combinando soluções analíticas (exatas e assintóticas) com simulações via Método dos Elementos Finitos (MEF).

O texto é estruturado como uma coletânea de quatro artigos já publicados, de autoria do autor e colaboradores. O primeiro investiga o escoamento de Poiseuille permanente em dutos com seções de segmento parabólico e lente parabólica, obtendo soluções analíticas e assintóticas por perturbação e separação de variáveis, usadas como referência para validação numérica ao longo de uma faixa ampla de parâmetros geométricos. O segundo trata de dutos com seções do tipo lente e figura-oito em coordenadas bipolares, derivando expressões explícitas para a vazão volumétrica e o número de Poiseuille em toda a família geométrica, recuperando casos clássicos e fornecendo avaliações em forma fechada para ângulos racionais. O terceiro apresenta soluções em série para o escoamento transiente de Poiseuille em triângulos hemi-equiláteros e isósceles retângulos, via superposição de autofunções, incluindo o campo de velocidade e a tensão de cisalhamento na parede, com aplicações diretas em validação de simulações transientes. Por fim, o quarto artigo aborda o escoamento de Darcy–Brinkman em tubos elípticos, obtendo uma nova expressão em série para o número de Poiseuille com funções de Mathieu, em excelente concordância com resultados de MEF. Em conjunto, os trabalhos ampliam a base analítica e numérica para escoamentos laminares em dutos de geometrias não convencionais.

Palavras-chave: Escoamento de Poiseuille; Escoamento de Darcy–Brinkman; Método dos Elementos Finitos; Soluções exatas; Dutos não circulares.

Título: Modelagem de escoamentos internos em dutos não circulares por métodos analíticos e elementos finitos.

Abstract

Internal laminar flow in ducts is a central topic in engineering, with both practical and theoretical relevance. Although advances in numerical methods and computational power have fostered high-accuracy numerical benchmarks, important gaps remain in the analytical literature for specific geometries. This dissertation addresses this need by developing new results and methodologies for Poiseuille and Darcy–Brinkman flows, combining analytical solutions (exact and asymptotic) with finite-element simulations (FEM).

The dissertation is organized as a collection of four peer-reviewed articles, authored by the candidate and collaborators, all previously published. The first paper investigates steady Poiseuille flow in ducts with parabolic-segment and parabolic-lens cross-sections, deriving new analytical and asymptotic solutions via perturbation methods and separation of variables, which are then used as reference data to validate numerical simulations across a broad range of geometric parameters. The second paper examines lens- and figure-eight-shaped ducts using bipolar coordinates, obtaining explicit analytical expressions for the volumetric flow rate and the Poiseuille number throughout the entire geometric family; the approach recovers classical solutions for circular ducts and right-angle lenses and provides closed-form evaluations for rational angles. The third paper focuses on transient Poiseuille flow in hemi-equilateral and right-isosceles triangular ducts, employing eigenfunction superposition to derive exact series solutions for the time-dependent velocity field and wall shear stress, offering valuable benchmark data for validating unsteady simulations. Finally, the fourth paper addresses Darcy–Brinkman flow in elliptic tubes, deriving a new exact series expression for the Poiseuille number in terms of Mathieu functions, with excellent agreement against FEM results. Taken together, these contributions broaden the analytical and numerical characterization of laminar duct flows in non-conventional geometries.

Key-words: Poiseuille flow; Darcy–Brinkman flow; Finite Element Method; Exact solutions; Non-circular ducts.

CONTENTS

LIST OF FIGURES

LIST OF TABLES

Chapter 1

Introduction

Pipes are fundamental components in a wide range of engineering systems involving the transport of fluids [4] (Figure 1.1), including energy conversion [5], chemical processing [6], thermal management [7], and large-scale distribution networks such as pipelines [8, 9, 10]. In this context, the cross-sectional geometry of a duct plays a decisive role in determining its hydraulic performance, directly affecting the system project regarding velocity distribution, pressure losses, wall shear stresses, and heat transfer characteristics. Although circular pipes are commonly adopted as a reference configuration due to their geometric simplicity, practical systems frequently employ non-circular cross-sections (Figure 1.2) arising from manufacturing constraints [11], structural reinforcement [12], or functional design requirements [13] (Figure 1.3). In parallel, the study of flow in porous media, governed, for example, by Darcy's law and extensions such as the Darcy–Brinkman model, plays a central role in many applications involving pipes containing porous materials (Figure 1.4). Including petroleum reservoir engineering, where predicting the mobility and recovery of hydrocarbons in subsurface formations is essential, groundwater management and environmental remediation [14, 15, 16, 17], as well as filtration and purification processes in chemical and biomedical engineering, for instance flows through filter media and membranes [18, 19, 20, 21].

Thus, it is evident that a solid understanding of heat and mass transfer in ducts is fundamental to scientific progress and industrial development. Consequently, significant research effort has been dedicated to refining the techniques used to analyze these phenomena. Over the past decades, the applicability of high–order computational simulations of ducts has been significantly expanded by advances in computational power, mesh generation techniques, and numerical solvers. Since its emergence in the 1940s as a numerical technique for structural analysis, the finite element method (FEM) has evolved into one of the most powerful and versatile computational frameworks for the solution of partial differential equations [22, 23]. Through the systematic organization of the variational formulation, a generalization from solid mechanics to areas including heat transfer, electromagnetism, and fluid mechanics [24]. In particular, one of the main advantages of the finite element method over other

Figure 1.1: Placement of circular pipes for gas transportation.

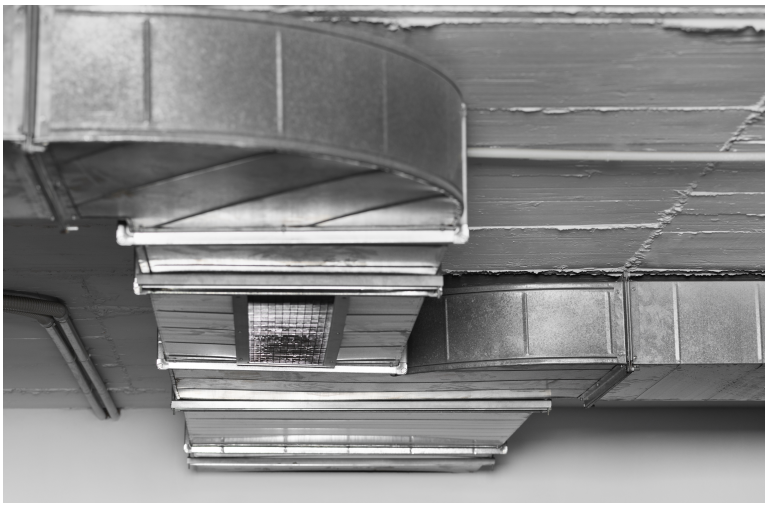

Figure 1.2: Rectangular cross–section ductwork for HVAC applications.

Figure 1.3: Flat–oval ductwork employed in installations with limited vertical clearance.

Figure 1.4: Pipe filled with porous metal foam. (Amani et al. [1])

numerical approaches is its ability to naturally handle complex domains and complicated boundary conditions, and it possesses a solid mathematical foundation [25].

In this context, the objective of this dissertation is to investigate the modelling of internal flows in various pipe geometries through the finite element method, emphasizing the validation against analytical reference solutions. The study aims to present novel solutions and quantify the influence of cross-sectional shape on hydraulic performance parameters, as well as to provide reliable benchmarks that may support further theoretical developments and engineering design applications.

1.1 Outline

This thesis is organized into seven main chapters. Chapter 2 provides a comprehensive literature review on laminar internal flows in ducts and related analytical, numerical and experimental developments. The discussion extends to a variety of internal flow problems, addressed through classical exact solutions, eigenfunction expansions, and conformal mappings.

Chapter 3 investigates the steady, laminar, two-dimensional Poiseuille flow of a Newtonian fluid through ducts whose cross-sections are described by parabolic segments and lens-shaped configurations. The governing Navier–Stokes equations under pressure-driven conditions are solved by combining numerical methods and analytical techniques. Parabolic coordinates and the method of separation of variables are used to derive special analytical solutions, while perturbation methods are applied for small aspect ratios and classical empirical formulas are employed for large aspect ratios. The study presents computed flow rates and friction factor–Reynolds number products across a range of geometric parameters, illustrat-

ing excellent agreement between analytical and numerical results and providing benchmark data for laminar flow in complex duct shapes.

The focus of Chapter 4 is the steady, fully developed Poiseuille flow of a Newtonian fluid in lens-shaped and figure-eight duct geometries, which arise in bipolar coordinates. The work derives explicit analytical expressions for the volumetric flow rate and associated Poiseuille number across a continuum of shapes. Closed-form solutions and asymptotic analyses are provided for distinct regimes, including thin lens, near circular, and strongly constricted figure-eight shapes. For practical applicability, a compact Padé approximant for the Poiseuille number is also introduced, yielding accurate approximations suitable for design calculations and for code verification.

Chapter 5 addresses the transient behavior of Poiseuille flow in ducts with triangular cross sections. Exact analytical solutions for the time-dependent velocity field, volumetric flow rate, and wall shear stress distribution are obtained by employing the eigenfunction superposition method for selected triangular geometries, specifically, the hemi-equilateral and right-angled isosceles triangles, which admit trigonometric eigenfunctions under Dirichlet boundary conditions. These solutions extend the classical steady-state results to the startup regime and provide benchmark for transient duct flow simulations in non-circular domains, filling a gap in the literature where only a limited set of triangular startup solutions had previously been treated.

In Chapter 6, the Darcy–Brinkman flow through a tube of elliptic cross section is revisited with an emphasis on deriving exact expressions for the fully developed velocity field and associated Poiseuille number in the presence of porous resistance. By building on classical analytical results for elliptic geometries and incorporating the additional drag term characteristic of Darcy–Brinkman flows, the chapter presents an exact series representation for the Poiseuille number. The analytical results are validated against finite-element solutions and classical Ritz approximations, demonstrating close agreement and extending theoretical benchmarks for porous-media internal flows in noncircular ducts.

Chapter 7 presents the numerical implementation adopted throughout this work using the FreeFEM framework. The procedures for domain definition, mesh generation, finite element discretization, time integration, and post-processing are detailed in order to further clarify the computational steps underlying the published results. Special attention is given to geometric aspects, mesh construction strategies, and numerical integration. The implementation is illustrated through representative problems addressed in the associated publications.

Finally, Chapter 8 summarizes the main findings of the thesis and outlines perspectives for future research, including possible extensions to heat transfer, unsteady and non–Newtonian flows, and further generalizations to complex duct geometries.

1.2 Publications

The following publications in international journals have been based on the work contained in this thesis:

1. **Silva, V. C.**; Gonçalves, M.; Lopes, A. B.; Alassar, R. S. *Poiseuille flow through parabolic segment and lens-shaped ducts.* **IMA Journal of Applied Mathematics**, Vol. 90, No. 4, pp. 347–369, 2025. [26]

2. **Silva, V. C.**; Lopes, A.B. *Revisiting Poiseuille flow through lens-shaped and figure-eight ducts.* **Mechanics Research Communications**, Vol. 150, Article 104570, 2025. [27]

3. **Silva, V. C.**; Lustosa, B. P.; Lopes, A.B. *Startup of Poiseuille flow in triangular ducts.* **Zeitschrift für Angewandte Mathematik und Physik (ZAMP)**, Vol. 76, No. 6, Article 241, 2025. [28]

4. Lopes, A. B.; Far, M. E. F.; **Silva, V. C.** *Revisiting Darcy–Brinkman Flow Through an Elliptic Tube.* **Transport in Porous Media**, Vol. 153, No. 1, pp. 13, 2025. [29]

The following works presented at international conferences originated from the research developed in this thesis:

1. Lopes, A.B., Moreira, G. G., & **Silva, V. C.** (2025).*Poiseuille flow through parabolic segment and lens-shaped ducts.* Presented at the **British Applied Mathematics Colloquium (BAMC 2025)**, Exeter, United Kingdom.

Chapter 2

Literature Review

2.1 Contextualization

One of the earliest studies of laminar flow in channels was carried out by the French physician and physicist Jean Louis Marie Poiseuille, whose work was motivated by the study of blood circulation in the arteries and veins of the human body [30]. His interest in understanding the mechanisms governing flow in capillary vessels led to a series of carefully designed experiments, resulting in the formulation of one of the most important laws describing laminar flow of viscous fluids. In his 1844 work, Poiseuille demonstrated that the volumetric flow rate through a circular tube is directly proportional to the pressure drop along the tube and to the fourth power of its diameter, and inversely proportional to its length. The experimental apparatus employed by Poiseuille consisted of a glass reservoir connected to a vertical copper tube and several glass capillaries, allowing precise measurements of flow under controlled conditions.

Nearly simultaneously, the German hydraulic engineer Gotthilf Heinrich Ludwig Hagen conducted experimental studies on laminar flow in circular ducts using brass tubes [31]. In 1839, Hagen identified the relationship between pressure drop and tube diameter and also observed a strong dependence of the results on fluid temperature. Although their experiments were conducted separately, the findings of Poiseuille and Hagen were complementary. Their combined contributions gave rise to the classical Hagen–Poiseuille law, which constitutes a fundamental result in fluid mechanics and in the analysis of laminar viscous flow in circular pipes.

As engineering applications evolved and diversified, the demand for predictive models applicable to non-circular ducts grew substantially. This increasing demand stimulated a large body of theoretical, experimental, and numerical studies aimed at extending classical results to numerous cross-sectional geometries, giving rise to a wide range of new formulations and problems.

Motivated by this need, Shah and London [32] produced a seminal compendium of ana-

lytical, numerical, and experimental results gathered from numerous authors on the laminar flow and forced convection of Newtonian fluids with constant properties in straight, steady, non-porous ducts of constant cross section. The main goal of this work was to present a comprehensive understanding of how geometric parameters influence hydrodynamic and thermal performance is essential for both design and benchmarking purposes. This monograph remains a standard reference to this day and represents a milestone in duct-flow research, being an essential reference for all subsequent works published.

At present, there exists a broad and continuously expanding body of literature devoted to internal flows in ducts, encompassing both geometric and physical generalizations of the classical Poiseuille problem. A significant fraction of these studies focuses on ducts with non-circular or spatially varying cross-sections, motivated by the strong influence of geometry on hydraulic resistance, velocity distributions, and heat transfer characteristics [33, 34]. Beyond geometric variations, many works investigate different thermal boundary conditions, commonly referred to as H1 and H2 problems, where H1 corresponds to a constant wall temperature and H2 to a constant wall heat flux, leading to distinct Nusselt numbers and thermal development behaviors [35, 36, 37, 38]. In micro- and nano-scale applications, the classical no-slip boundary condition becomes invalid, giving rise to slip-flow regimes in which a finite tangential velocity exists at the wall; such effects are typically modeled through slip-length boundary conditions and are governed by the Knudsen number, playing a central role in microfluidics and rarefied gas flows [39, 40]. Another active line of research concerns non-Newtonian fluids in ducts, where constitutive models such as power-law, Carreau, Cross, Bingham, Herschel–Bulkley, and viscoelastic models like Maxwell and Oldroyd-B are employed to capture shear-thinning, yield-stress, and elastic effects, substantially modifying pressure drops, velocity profiles, and transient responses compared to Newtonian flows [41, 42]. Unsteady internal flows driven by oscillatory pressure gradients have also received considerable attention due to their relevance in physiological flows, pulsatile transport, and flow control; these studies analyze frequency-dependent responses, phase lags, and viscous penetration depths in oscillatory Poiseuille flow [43, 44, 45]. Closely related canonical problems include Couette flow, driven by moving boundaries, and the Rayleigh–Stokes or Stokes' second problem, which describes the transient and oscillatory response of a viscous fluid to wall motion; these problems provide exact solutions that are widely used as benchmarks for transient solvers and for understanding viscous diffusion mechanisms [46]. Additional extensions reported in the literature include flows in porous ducts modeled by Darcy–Brinkman equations, conjugate heat transfer, mixed boundary conditions, and stability and transition analyses, collectively illustrating the richness and ongoing relevance of duct-flow research across engineering and applied mathematics [47, 48].

In this dissertation, we investigate three model problems, which are addressed in the subsequent chapters: transient Poiseuille flow, steady Poiseuille flow, and Darcy–Brinkman flow in porous media. In this chapter, we present the mathematical formulation of these problems.

2.2 Problem Statement

Let a duct of generic cross-sectional shape defined by a border $\partial\Omega$ and characteristic lenght ℓ be fully filled with an incompressible Newtonian fluid laminar flow set into motion by a constant pressure gradient in the absence of body forces, as illustrated in Fig. 2.1.

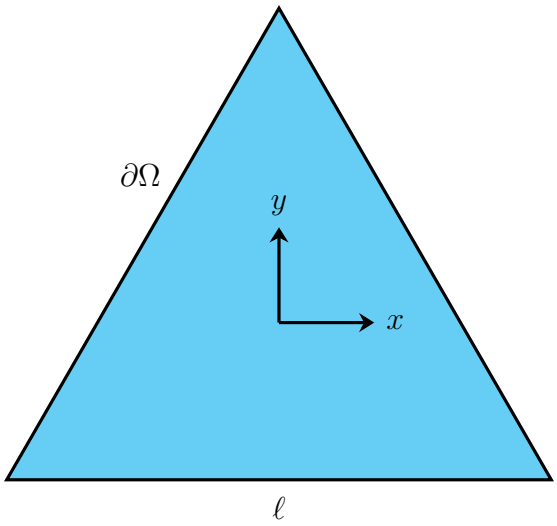

Figure 2.1: Example of a duct cross-section.

With these considerations, the governing equations of the problem are the continuity equation

$$\nabla \cdot \mathbf{u} = 0, \tag{2.1}$$

and the Navier–Stokes equation

$$\rho\left[\frac{\partial \mathbf{u}}{\partial t} + (\mathbf{u}\cdot\nabla)\,\mathbf{u}\right] = -\nabla p + \mu\nabla^2\mathbf{u}, \tag{2.2}$$

where $\mathbf{u}$ is the velocity field, p is the pressure field, μ is the dynamic viscosity of the fluid, ρ is the fluid density, and t denotes time.

In Cartesian coordinates (x, y, z), the continuity equation (2.1) can be written as

$$\frac{\partial u}{\partial x} + \frac{\partial v}{\partial y} + \frac{\partial w}{\partial z} = 0, \tag{2.3}$$

and the components of the Navier–Stokes equation (2.2) in the x, y, and z directions are given by

$$\rho\left(\frac{\partial u}{\partial t} + u\frac{\partial u}{\partial x} + v\frac{\partial u}{\partial y} + w\frac{\partial u}{\partial z}\right) = -\frac{\partial p}{\partial x} + \mu\left(\frac{\partial^2 u}{\partial x^2} + \frac{\partial^2 u}{\partial y^2} + \frac{\partial^2 u}{\partial z^2}\right), \tag{2.4}$$

$$\rho\left(\frac{\partial v}{\partial t}+u\frac{\partial v}{\partial x}+v\frac{\partial v}{\partial y}+w\frac{\partial v}{\partial z}\right)=-\frac{\partial p}{\partial y}+\mu\left(\frac{\partial^2 v}{\partial x^2}+\frac{\partial^2 v}{\partial y^2}+\frac{\partial^2 v}{\partial z^2}\right), \tag{2.5}$$

$$\rho\left(\frac{\partial w}{\partial t}+u\frac{\partial w}{\partial x}+v\frac{\partial w}{\partial y}+w\frac{\partial w}{\partial z}\right)=-\frac{\partial p}{\partial z}+\mu\left(\frac{\partial^2 w}{\partial x^2}+\frac{\partial^2 w}{\partial y^2}+\frac{\partial^2 w}{\partial z^2}\right), \tag{2.6}$$

respectively. Here u, v, and w denote the three velocity components.

Assuming unidirectional flow in the positive z-direction, the velocity field can be written as

$$\mathbf{u}=(0,0,w(x,y,z,t)). \tag{2.7}$$

Thus, the continuity equation (2.3) reduces to

$$\frac{\partial w}{\partial z}=0, \tag{2.8}$$

and consequently

$$w=w(x,y,t). \tag{2.9}$$

Therefore, in addition to being unidirectional, the flow is also two-dimensional in space.

Substituting (2.7) and (2.9) into (2.4), (2.5), and (2.6), one obtains

$$\frac{\partial p}{\partial x}=0, \tag{2.10}$$

$$\frac{\partial p}{\partial y}=0, \tag{2.11}$$

$$\mu\left(\frac{\partial^2 w}{\partial x^2}+\frac{\partial^2 w}{\partial y^2}\right)=\frac{\partial p}{\partial z}+\rho\frac{\partial w}{\partial t}. \tag{2.12}$$

From Eqs. (2.10) and (2.11), it follows that

$$p=p(z,t), \tag{2.13}$$

and therefore (2.12) becomes

$$\frac{\partial^2 w}{\partial x^2}+\frac{\partial^2 w}{\partial y^2}=\frac{1}{\mu}\frac{\mathrm{d}p}{\mathrm{d}z}+\frac{\rho}{\mu}\frac{\partial w}{\partial t}. \tag{2.14}$$

Since the nonzero velocity component depends on the coordinates x, y and time t, whereas the pressure field depends solely on the axial coordinate z and t, Eq. (2.14) can be satisfied only if the axial velocity and the pressure admit at most a temporal dependence.

Let Ω denote the cross-sectional region bounded by the duct contour $\partial\Omega$. The no-slip

boundary condition at the wall requires that

$$w = 0 \tag{2.15}$$

on $\partial\Omega$, the boundary of the domain.

To render the governing equation parameter-free, a nondimensionalisation of the characteristic length and velocity scales is performed, while preserving its original structure as a Poisson equation. Introducing

$$\tilde{x} = \frac{x}{\ell}, \quad \tilde{y} = \frac{y}{\ell}, \quad \tilde{w} = \frac{w}{U}, \quad \tilde{t} = \frac{\rho \ell^2 t}{\mu} \tag{2.16}$$

into Eq. (2.14), one obtains

$$\left(\frac{\partial^2 \tilde{w}}{\partial \tilde{x}^2} + \frac{\partial^2 \tilde{w}}{\partial \tilde{y}^2} \right) = \frac{\ell^2}{U\mu} \frac{\mathrm{d}p}{\mathrm{d}z} + \frac{\partial \tilde{w}}{\partial \tilde{t}}. \tag{2.17}$$

Following Shah & London [33], we choose

$$U = -\frac{\ell^2}{\mu} \frac{\mathrm{d}p}{\mathrm{d}z}, \tag{2.18}$$

so that the previous equation reduces to

$$\frac{\partial^2 \tilde{w}}{\partial \tilde{x}^2} + \frac{\partial^2 \tilde{w}}{\partial \tilde{y}^2} + 1 = \frac{\partial \tilde{w}}{\partial \tilde{t}}. \tag{2.19}$$

Since it was previously assumed that the flow takes place in the positive z-direction, the negative sign in Eq. (2.18) is required in order to satisfy this condition. Equation (2.19) therefore corresponds to the transient Poiseuille problem. The steady Poiseuille equation is readily recovered by suppressing the local acceleration term; that is, by setting

$$\frac{\partial \tilde{w}}{\partial \tilde{t}} = 0. \tag{2.20}$$

2.2.1 Darcy–Brinkman formulation

We now consider the flow of an incompressible Newtonian fluid through a homogeneous porous medium inside a pipe, which is governed by the Darcy-Brinkman equations

$$\nabla \cdot \mathbf{u} = 0, \tag{2.21}$$

$$\rho \left[\frac{\partial \mathbf{u}}{\partial t} + (\mathbf{u} \cdot \nabla)\mathbf{u} \right] = -\nabla p + \mu_e \nabla^2 \mathbf{u} - \frac{\mu}{K}\mathbf{u}, \tag{2.22}$$

where $\mathbf{u}$ in this equation is the Darcy velocity, μ_e is the effective viscosity of the porous medium, μ is the dynamic viscosity of the fluid, and K is the permeability. Although the Darcy-–Brinkman model is mathematically similar to the Navier–Stokes equations, it introduces an additional material parameter associated with the porous matrix. In contrast, the Navier—Stokes formulation depends solely on fluid properties such as density and viscosity, whereas the Darcy—Brinkman formulation also incorporates the permeability of the medium.

Assuming fully developed unidirectional flow in the positive z-direction,

$$\mathbf{u} = (0, 0, w(x, y)), \qquad p = p(z), \tag{2.23}$$

Similarly, the continuity equation (2.21) reduces to

$$\frac{\partial w}{\partial z} = 0, \tag{2.24}$$

and therefore

$$w = w(x, y). \tag{2.25}$$

The axial momentum balance reduces to

$$\mu_e \left(\frac{\partial^2 w}{\partial x^2} + \frac{\partial^2 w}{\partial y^2} \right) - \frac{\mu}{K} w = \frac{dp}{dz}. \tag{2.26}$$

Introducing the dimensionless variables

$$\tilde{x} = \frac{x}{\ell}, \qquad \tilde{y} = \frac{y}{\ell}, \qquad \tilde{w} = \frac{w}{U}, \tag{2.27}$$

and choosing the velocity scale based on the effective viscosity of the porous medium

$$U = -\frac{\ell^2}{\mu_e} \frac{\mathrm{d}p}{\mathrm{d}z}, \tag{2.28}$$

Eq. (2.26) becomes

$$\frac{\partial^2 \tilde{w}}{\partial \tilde{x}^2} + \frac{\partial^2 \tilde{w}}{\partial \tilde{y}^2} - s^2 \tilde{w} + 1 = 0, \tag{2.29}$$

where the porous medium parameter s is defined by

$$s = \frac{\ell}{\sqrt{K}} \sqrt{\frac{\mu}{\mu_e}}. \tag{2.30}$$

The no-slip boundary condition at the duct wall reads

$$\tilde{w} = 0 \qquad \text{on } \partial\Omega. \tag{2.31}$$

2.3 Parameters

2.3.1 Volumetric Flow Rate

The volumetric flow rate is a quantity of fundamental importance in the study of internal flows. Throughout this work, it plays a central role in the derivation of the results, where it is used in the computation of the product of the Fanning friction factor and the Reynolds number, the Poiseuille number. Therefore, it is necessary to define the calculation of this quantity, which, in Cartesian coordinates, is given by

$$\tilde{Q}(t) = \iint_{\Omega} \tilde{w}(x, y, t)\mathrm{d}x\mathrm{d}y. \tag{2.32}$$

2.3.2 Poiseuille number

In order to compare the results obtained in this work for steady flows with those reported in the literature and to assess the global accuracy of the numerical method employed, a fundamental dimensionless indicator is considered: the product of the Fanning friction factor and the Reynolds number fRe, also known as the Poiseuille number Po.

The Poiseuille number is a proportionality constant relating the pressure gradient to the mean velocity. Accordingly, for a given fluid flowing with a fixed mean velocity in ducts with the same hydraulic diameter, an increase in the Poiseuille number implies a corresponding increase in the pressure gradient [49].

This constant results from the product of the Fanning friction factor and the Reynolds number, two parameters widely used in fluid mechanics that provide useful insight, for instance, in the design of compact heat exchangers. Wang [50] define the dimensionless form of the Poiseuille number for ducts as

$$fRe = Po = \frac{8\tilde{A}^3}{\tilde{P}^2\tilde{Q}}. \tag{2.33}$$

For the sake of notational simplicity, the tildes are omitted hereafter to avoid an excessive accumulation of symbols.

2.4 Finite Element Formulation

The finite element method is a numerical technique for constructing approximate solutions of differential equations posed on bounded domains with prescribed boundary conditions. Essentialy, the computational domain is partitioned into a finite number of elements, over which the unknown field is approximated by locally defined basis functions. The governing equations are expressed in a variational (weak) formulation, which allows the solution

to be sought in an appropriate function space while incorporating the boundary conditions [51, 52, 53].

Let $\Omega \subset \mathbb{R}^2$ be the cross-sectional domain of a straight duct with boundary $\partial\Omega$. The governing equation is the dimensionless transient Poiseuille flow

$$\frac{\partial w}{\partial t} - \nabla^2 w = 1, \tag{2.34}$$

where $w(x, y, t)$ denotes the axial velocity field.

The no-slip boundary condition is imposed on the duct wall,

$$w = 0 \qquad \text{on } \partial\Omega \times (0, T], \tag{2.35}$$

together with the initial time condition

$$w(x, y, 0) = 0. \tag{2.36}$$

2.4.1 Weak formulation

Let V_h be a functional space of admissible trial and test functions. The approximate solution is sought within V_h, which is a finite-dimensional subspace of a larger space V. The space V represents the continuous function space in which the exact solution of the problem exists. The space V_h should be constructed as a very close approximation of the space V. With this approximation in place, the weak formulation is then derived step by step, closely following the formulation proposed by Johnson [53]. Multiplying (2.34) by a test function $\phi \in V_h$ and integrating over Ω gives

$$\int_\Omega \frac{\partial w}{\partial t}\,\phi\, d\Omega - \int_\Omega \nabla^2 w\,\phi\, d\Omega = \int_\Omega \phi\, d\Omega. \tag{2.37}$$

Applying Green's formula (integration by parts) to the Laplacian term:

$$-\int_\Omega (\nabla^2 w)\phi\, d\Omega = \int_\Omega \nabla w \cdot \nabla\phi\, d\Omega - \int_{\partial\Omega} \frac{\partial w}{\partial n}\phi\, d\Gamma.$$

Since the boundary condition is homogeneous Dirichlet ($w = 0$), we choose the space of test functions such that $\phi = 0$ on the boundary $\partial\Omega$. Consequently, the surface integral vanishes. The variational problem is:

$$\int_\Omega \frac{\partial w}{\partial t}\phi\, d\Omega + \int_\Omega \nabla w \cdot \nabla\phi\, d\Omega = \int_\Omega \nabla\phi\, d\Omega, \quad \forall \phi \in V_h \tag{2.38}$$

3. Time Integration

For numerical implementation, we approximate the time derivative using the implicit Euler method, also known as backward Euler method:

$$\frac{\partial u}{\partial t} \approx \frac{w^{n+1} - w^n}{\Delta t}$$

where w^{n+1} is the solution at the current time step and w^n is the known solution from the previous step. Substituting this into the weak form, we get

$$\int_\Omega \frac{w^{n+1} - w^n}{\Delta t} \phi \, d\Omega + \int_\Omega \nabla w^{n+1} \cdot \nabla \phi \, d\Omega = \int_\Omega \phi \, d\Omega. \tag{2.39}$$

Rearranging to separate unknown terms (w^{n+1}) from known terms (w^n), it follows that

$$\int_\Omega w^{n+1} \phi \, d\Omega + \Delta t \int_\Omega \nabla w^{n+1} \cdot \nabla \phi \, d\Omega = \int_\Omega w^n \phi \, d\Omega + \Delta t \int_\Omega \phi \, d\Omega \tag{2.40}$$

At each time step, equation (2.40) is solved to compute the updated solution u^{n+1}. Since the unknown appears implicitly in the variational form, a linear system must be solved at every time increment. The backward Euler scheme is unconditionally stable for diffusion-type problems and provides a consistent approximation of the transient evolution toward the steady Poisson solution [54, 55].

It is important to note that in the limit $t \to \infty$, the transient solution converges to the steady Poisson problem

$$\nabla^2 w = -1, \tag{2.41}$$

which corresponds to the fully developed Poiseuille flow in dimensionless form.

2.4.2 Finite Elements Discretization

The domain Ω is discretized into a conforming triangular mesh $\mathcal{T}_h$, composed of non-overlapping elements. In this work, the spatial discretization is performed using Lagrangian continuous piecewise polynomial finite elements of degree two (P2). This element has only degrees of freedom wich corresponds to the value of the function on a node. Each P2 triangular element has six local degrees of freedom, associated with the three vertices and the three edge midpoints.

The finite element approximation of the velocity field is written as

$$w_h(\mathbf{x}) = \sum_{j=1}^{N} W_j \phi_j(\mathbf{x}),$$

where ϕ_j are the global basis functions and W_j are the corresponding nodal values. The spa-

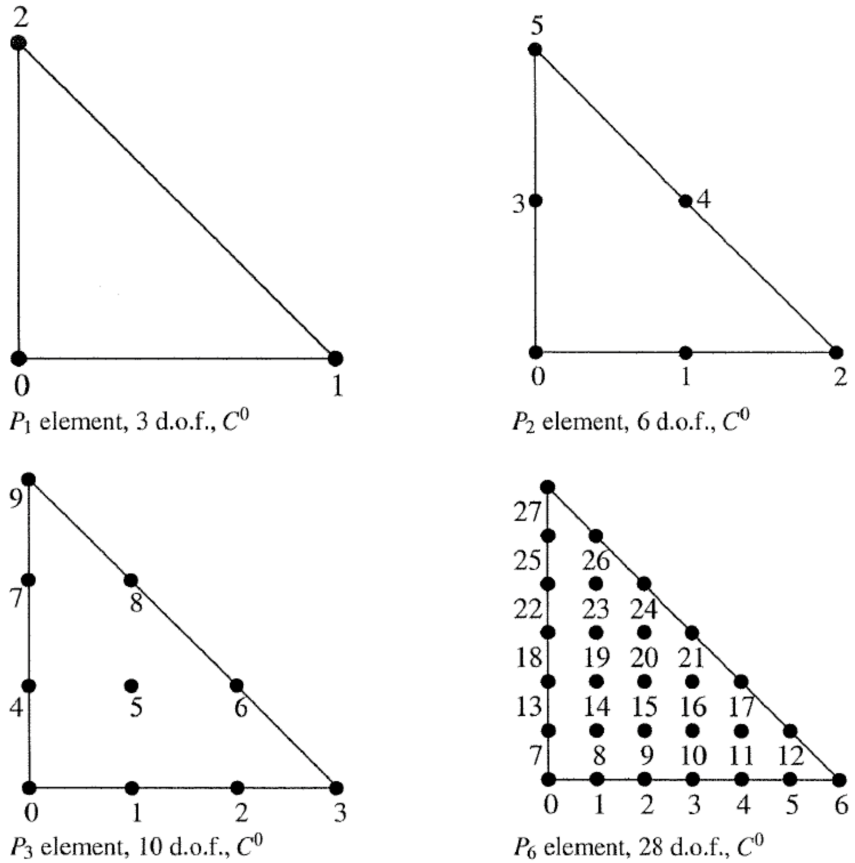

Figure 2.2: Examples of classical P_k Lagrange elements on a triangle. (Dhahbi et al. [2])

tial discretization and matrix assembly procedures are implemented using the FreeFEM software, which employs a classical Galerkin formulation with identical trial and test spaces. The discrete solution is expressed in terms of local Lagrangian shape functions associated with the nodal degrees of freedom, ensuring continuity across element interfaces. The Galerkin projection of the weak formulation onto the finite-dimensional space leads, after assembly over all elements, to a global sparse linear system for the nodal unknowns.

Chapter 3

Poiseuille flow through parabolic segment and lens-shaped ducts

This chapter is a reproduction of the following publication:

Silva, V. C.; Gonçalves, M.; Lopes, A. B.; Alassar, R. S. Poiseuille flow through parabolic segment and lens-shaped ducts. IMA Journal of Applied Mathematics, Vol. 90, No. 4, pp. 347–369, 2025.

3.1 Introduction

Ducts with constant cross-sections play a crucial role in the refrigeration and air conditioning industries, where they are extensively used in heat exchangers [56, 57]. Furthermore, these ducts have a wide range of applications in diverse fields, such as electronic cooling [58] and blood filtration through haemodialysis [59]. In the oil industry, for instance, understanding fluid flow behaviour is fundamental for optimizing extraction and transportation processes [60]. As such, the study of fluid flow through ducts is essential not only for advancing technologies across various sectors but also for driving innovations in critical areas, from medicine to electronics and petroleum engineering.

While circular ducts are the most commonly employed in various industries due to their structural efficiency and ease of manufacturing, natural phenomena can alter the shape of their cross-sections. One such phenomenon is the deposition of paraffin in pipelines, which poses a significant challenge in the oil industry [61]. This process leads to changes in the duct's geometry, subsequently affecting both the flow pressure and heat transfer between the oil and the duct walls. Similarly, alterations in cross-sectional shape are observed in blood vessels, where the accumulation of fat plaques results in blockages, as seen in conditions like atherosclerosis [62].

All the cross-sections shown in Table 3.1 have exact analytical solutions for Poiseuille

flows, which are crucial for advancing our understanding of the phenomena described by the Navier-Stokes equations, as discussed in [63]. These solutions serve as essential benchmarks for validating numerical, asymptotic, and empirical models, which are key to solving more complex problems. Although the main orthogonal two-dimensional coordinate systems used in mathematical physics to derive these solutions are Cartesian, polar, parabolic, bipolar, and elliptic coordinates [64], most solutions for ducts with convex cross-sections have been derived in Cartesian coordinates. It is worth noting that not all exact solutions were originally obtained for Poiseuille flow in ducts; however, many can be deduced by analogy. For instance, the solutions presented in [65, 66, 67] pertain to open-channel flows, while those in [68, 69, 70] address the torsion of prismatic bars, and the work of [71] concerns the motion of a liquid in a rotating vessel.

In the case of polar coordinates, several non-convex cross-sections have been investigated, including moon-shaped [33], cardioid [50], and concentric annular geometries [72]. Similarly, bipolar coordinates have been employed to analyse eccentric annular cross-sections [73]. Building on the work of Alassar & Abushoshah on ducts with semi-elliptical cross-sections [74], there was a significant expansion in the use of elliptic coordinates to obtain exact solutions for both isothermal and non-isothermal Poiseuille flows in elliptic-related geometries [75, 76, 77, 78, 79, 80].

Table 3.1: Exact solutions for Poiseuille flow through constant convex cross-sectional ducts.

Cross section	Coordinate system(s)	Reference(s)
Circle	Cartesian coordinates / Polar coordinates	[81, 82]
Circular lens	Cartesian coordinates / Bipolar coordinates	[68, 66, 67]
Circular sector	Polar coordinates	[83, 84, 85]
Ellipse	Cartesian coordinates / Elliptic coordinates	[86, 87]
Equilateral triangle	Cartesian coordinates	[86]
Hemi-equilateral triangle	Cartesian coordinates	[71, 69]
Hyperbolic segment	Cartesian coordinates	[70]
Isosceles right triangle	Cartesian coordinates	[65]
Parabolic lens	Parabolic coordinates	[65]
Quarter-ellipse	Elliptic coordinates	[80]
Rectangle	Cartesian coordinates	[86]
Semi-ellipse	Elliptic coordinates	[74, 75, 77]
Two parabolas	Parabolic coordinates	[88]

While parabolic coordinates are widely utilised in theoretical and applied physics—playing a key role in the study of wave phenomena in quantum mechanics and acoustics [89], the Stark and Zeeman effects [90], electrostatic ion traps [91], and

elasticity problems [92]—their application in the context of Poiseuille flow remains scarce, with notable exceptions being the works listed in Table 3.1. Outside of Poiseuille flow, parabolic coordinates have been employed in other fluid mechanics problems, such as liquid surface waves in parabolic tanks [93] and steady water flow around parabolic cavities and through parabolic inclusions in unsaturated and saturated soils [94].

In this context, the present study investigates Poiseuille flow through parabolic segment and lens-shaped ducts. The lens-shaped duct, mathematically equivalent to open-channel flow in a parabolic channel, was previously examined by Proudman [65]. Moshinskii's work [88], although focused on liquid flow in a channel bounded by two parabolas, is conceptually related to the lens-shaped duct. Meanwhile, the parabolic segment duct remains unexplored in the literature. This study extends their work by providing an asymptotic solution via perturbation methods, valid for ducts with small aspect ratios, and a numerical solution using the finite element method, applicable to ducts of any aspect ratio. For ducts with large aspect ratios, the Maclaine–Cross approximate formula is employed to directly evaluate the limiting value of the friction factor–Reynolds number product. Additionally, alternative solutions to theirs are obtained using the eigenfunction expansion method. For both cases, we calculate the flow rate and the friction factor–Reynolds number product—key parameters of interest for engineers.

A prominent application of the parabolic geometries and flows discussed in this work is found in infiltration trenches used in domestic wastewater treatment systems, where treated effluent percolates naturally through the soil. Parabolic geometries are particularly suited for these systems due to their structural and hydraulic advantages. Ref. [95] argued that since riverbeds and irrigation furrows tend to adopt a parabolic shape, this geometry is more hydraulically and structurally stable than the conventional trapezoidal design, as exemplified by the Pehur High Level Canal in Pakistan. The advantages of parabolic sections over trapezoidal ones, highlighted by [96], include ease and speed of construction, reduced stress concentration, a 2% reduction in concrete volume, and improved sediment transport capacity. Furthermore, parabolic trenches are used in urban stormwater drainage systems to mitigate flooding and address the impacts of climate change [97].

Additionally, the study of flow in narrow ducts with parabolic and lens-shaped geometries has applications in fields such as oil and gas recovery during hydraulic fracturing, where narrow fractures are propped by proppants like sand or ceramics, and in the modelling of inter-endothelial clefts between cells, which serve as filters for large molecules. These applications, although not directly explored in this work, highlight the broader relevance of the flow behaviour in such geometries, as discussed in [98].

Our work is structured as follows: In Sec. 3.2, we introduce the formulation, presenting the governing equations and boundary conditions in Cartesian coordinates for Poiseuille flow through parabolic segment and lens-shaped ducts. In Sec. 3.3, we present special analytical solutions for both geometries in parabolic coordinates using the method of separation of variables, and apply perturbation methods for small aspect ratios. For large aspect ratios,

the Maclaine–Cross approximate method [99] is employed. In Sec. 3.4, we briefly discuss the numerical solution of these problems using the finite element method. In Sec. 3.5, we present and discuss the results. Finally, in Sec. 3.6, we provide the main conclusions of the study.

3.2 Formulation

Consider the steady, laminar, two-dimensional Poiseuille flow of a Newtonian fluid through ducts with cross-sectional shapes of either a parabolic segment or a lens, both characterized by a width 2ℓ and aspect ratio λ. We normalise all lengths by ℓ, and the axial velocity by $G\ell^2/\mu$, where G is the constant pressure gradient in the axial direction and μ is the dynamic viscosity of the fluid. Both configurations are sketched in Figure 3.1.

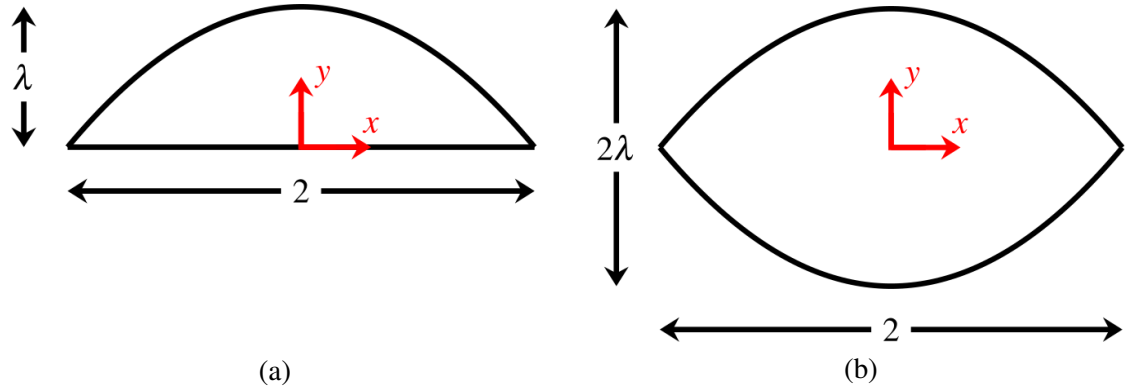

Figure 3.1: Sketch of a parabolic segment in panel (a) and a lens in panel (b).

The flow is governed by the Poisson equation

$$\nabla^2 w = -1, \tag{3.1}$$

where $w = w(x, y)$ is the dimensionless axial velocity and

$$\nabla^2 = \frac{\partial^2}{\partial x^2} + \frac{\partial^2}{\partial y^2} \tag{3.2}$$

is the Laplace operator.

3.2.1 Parabolic segment

For the parabolic segment duct, the boundary conditions are the no-slip conditions

$$w(x, y = 0) = 0, \tag{3.3}$$

and

$$w\left(x, y = \lambda\left(1 - x^2\right)\right) = 0. \tag{3.4}$$

The dimensionless volumetric flow rate is given by

$$Q = \int_{-1}^{1} \int_{0}^{\lambda(1-x^2)} w \, \mathrm{d}y \, \mathrm{d}x. \tag{3.5}$$

By definition, the Fanning friction factor–Reynolds number product, fRe, can be computed as follows

$$fRe = \frac{8A^3}{P^2 Q}, \tag{3.6}$$

where A is the dimensionless area enclosed by the parabolic segment, and P is the dimensionless wetted perimeter (see, e.g., [33]). It is straightforward to verify that

$$A = \frac{4\lambda}{3} \tag{3.7}$$

and

$$P = 2 + \frac{\sinh^{-1}(2\lambda)}{2\lambda} + \sqrt{1 + 4\lambda^2}. \tag{3.8}$$

3.2.2 Parabolic lens

For the lens-shaped duct, Eq. (3.3) is replaced by

$$w\left(x, y = -\lambda\left(1 - x^2\right)\right) = 0, \tag{3.9}$$

and the dimensionless volumetric flow rate is expressed as

$$Q = \int_{-1}^{1} \int_{-\lambda(1-x^2)}^{\lambda(1-x^2)} w \, \mathrm{d}y \, \mathrm{d}x. \tag{3.10}$$

Similarly, the dimensionless area is

$$A = \frac{8\lambda}{3} \tag{3.11}$$

and

$$P = \frac{\sinh^{-1}(2\lambda)}{\lambda} + 2\sqrt{1 + 4\lambda^2} \tag{3.12}$$

is the wetted perimeter.

3.3 Special analytical solutions

Analytical solutions for Poiseuille flow through parabolic segment and lens-shaped ducts can be obtained using perturbation methods for $\lambda \to 0$, separation of variables in parabolic coordinates for $\lambda = 0.5$, and the Maclaine–Cross approximate method for $\lambda \to \infty$.

3.3.1 Parabolic segment

3.3.1.1 $\lambda \ll 1$ or $\lambda \gg 1$

For a parabolic segment with $\lambda \ll 1$, we follow the framework of Ref. [100]. Let

$$y = \lambda\eta \tag{3.13}$$

and

$$w = \lambda^2 \left[w_0 (x, \eta) + \lambda^2 w_2 (x, \eta) + \ldots \right], \tag{3.14}$$

where $\eta = O(1)$. Substitution of Eqs. (3.13) and (3.14) into Eq. (3.1) yields the successive orders

$$\frac{\partial^2 w_0}{\partial \eta^2} = -1 \tag{3.15}$$

and

$$\frac{\partial^2 w_2}{\partial \eta^2} = -\frac{\partial^2 w_0}{\partial x^2}. \tag{3.16}$$

The boundary condition (3.3) gives

$$w_0(x, \eta = 0) = 0 \tag{3.17}$$

and

$$w_2(x, \eta = 0) = 0, \tag{3.18}$$

while the boundary condition (3.4) leads to

$$w_0(x, \eta = 1 - x^2) = 0 \tag{3.19}$$

and

$$w_2(x, \eta = 1 - x^2) = 0. \tag{3.20}$$

The solution of Eq. (3.15), subject to the boundary conditions in Eqs. (3.17) and (3.19), is given by

$$w_0 = -\frac{\eta}{2} \left[\eta - \left(1 - x^2 \right) \right]. \tag{3.21}$$

Similarly, solving Eq. (3.16) under the boundary conditions in Eqs. (3.18) and (3.20), we obtain

$$w_2 = \frac{\eta}{6} \left[\eta^2 - \left(1 - x^2 \right)^2 \right]. \tag{3.22}$$

From Eqs. (3.5), (3.14), (3.21) and (3.22), the dimensionless volumetric flow rate is

$$Q = \lambda^3 \int_{-1}^{1} \int_{0}^{1-x^2} \left[w_0(x,\eta) + \lambda^2 w_2(x,\eta) + \ldots \right] \mathrm{d}\eta \, \mathrm{d}x = \frac{8\lambda^3}{105} - \frac{32\lambda^5}{945} + O\left(\lambda^7\right). \tag{3.23}$$

Finally, by substituting Eqs. (3.7), (3.8), and (3.23) into (3.6) and expanding in powers of λ, we find that

$$fRe = \frac{140}{9} - \frac{280\lambda^2}{81} + O\left(\lambda^4\right), \tag{3.24}$$

from which follows that

$$\lim_{\lambda \to 0} fRe = \frac{140}{9} \approx 15.5556. \tag{3.25}$$

To determine the limiting value of fRe as $\lambda \to \infty$, we focus directly on our primary quantity of interest, fRe, and employ the Maclaine–Cross formula [99], which in our variables reads

$$\lim_{\lambda \to \infty} fRe = \lim_{\lambda \to \infty} \frac{96}{P^2} \frac{\left(\int_0^\lambda 2\sqrt{1 - \frac{y}{\lambda}} \, \mathrm{d}y \right)^3}{\int_0^\lambda \left(2\sqrt{1 - \frac{y}{\lambda}} \right)^3 \mathrm{d}y} = \frac{160}{9} \approx 17.7778. \tag{3.26}$$

3.3.1.2 $\lambda = 0.5$

The natural orthogonal coordinate system for the special case of $\lambda = 0.5$ is the parabolic coordinate system (σ, τ), which is related to the Cartesian coordinate system (x, y) via

$$x = \sigma\tau, \quad y = \frac{1}{2}\left(\tau^2 - \sigma^2\right), \tag{3.27}$$

where $-\infty < \sigma < \infty$ and $0 \leq \tau < \infty$ [101]. The scale factors are given by

$$h_\sigma = h_\tau = \sqrt{\sigma^2 + \tau^2}, \tag{3.28}$$

which allows the Laplace operator (3.2) to be written as

$$\nabla^2 = \frac{1}{h_\tau h_\sigma} \left(\frac{\partial^2}{\partial \sigma^2} + \frac{\partial^2}{\partial \tau^2} \right) = \frac{1}{(\sigma^2 + \tau^2)} \left(\frac{\partial^2}{\partial \sigma^2} + \frac{\partial^2}{\partial \tau^2} \right). \tag{3.29}$$

The differential element of area then becomes

$$\mathrm{d}A = h_\sigma h_\tau \, \mathrm{d}\sigma \, \mathrm{d}\tau = \left(\sigma^2 + \tau^2\right) \mathrm{d}\sigma \, \mathrm{d}\tau. \tag{3.30}$$

In parabolic coordinates, the problem of Eqs. (3.1), (3.3) and (3.4) reduces to solving

$$\frac{1}{(\sigma^2 + \tau^2)} \left(\frac{\partial^2 w}{\partial \sigma^2} + \frac{\partial^2 w}{\partial \tau^2} \right) = -1, \tag{3.31}$$

subjected to the boundary conditions

$$w\left(\sigma = \pm\tau, \tau\right) = 0, \tag{3.32}$$

and

$$w\left(\sigma, \tau = 1\right) = 0, \tag{3.33}$$

Note that the parabolic segment in the (x, y)-plane is mapped onto a right isosceles triangle in the (σ, τ)-plane, as shown in Figure 3.2.

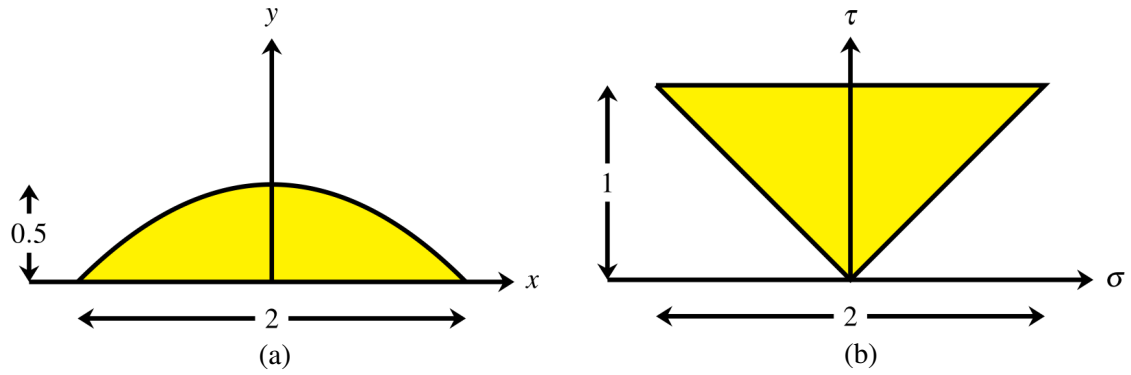

Figure 3.2: Mapping of the parabolic segment in the (x, y)-plane (a) to a right isosceles triangle in the (σ, τ)-plane (b).

The dimensionless volumetric flow rate (3.5) takes the form

$$Q = \int_0^1 \int_{-\tau}^{\tau} w\left(\sigma^2 + \tau^2\right) \mathrm{d}\sigma \, \mathrm{d}\tau. \tag{3.34}$$

For $\lambda = 0.5$, Eqs. (3.7) and (3.8) give

$$A = \frac{2}{3}, \tag{3.35}$$

and

$$P = 2 + \sqrt{2} + \ln\left(1 + \sqrt{2}\right). \tag{3.36}$$

Let us seek a solution to Eq. (3.31) of the form

$$w = -\frac{1}{8}\left(\tau^2 - \sigma^2\right)^2 + \sum_{m=1}^{\infty} W_m \left[\cos\left(\alpha_m \sigma\right) \cosh\left(\alpha_m \tau\right) - \cosh\left(\alpha_m \sigma\right) \cos\left(\alpha_m \tau\right)\right], \tag{3.37}$$

where

$$\alpha_m = \frac{\pi\left(2m - 1\right)}{2} \tag{3.38}$$

It is important to observe that the first term on the right-hand side of Eq. (3.37) represents a particular solution of Eq. (3.31), while the second term corresponds to a harmonic function. Furthermore, it can be readily verified that the solution satisfies Eq. (3.32), so the coefficients

W_m must be determined using the remaining boundary condition (3.33), which leads to

$$-\frac{1}{8}\left(1-\sigma^2\right)^2+\sum_{m=1}^{\infty} W_m \cos\left(\alpha_m \sigma\right) \cosh\left(\alpha_m\right)=0. \tag{3.39}$$

Multiplying both sides of Eq. (3.39) by $\cos\left(\alpha_n \sigma\right)$ and integrating with respect to σ from 0 to 1 and solving the resulting equation for W_m, we obtain

$$W_m=-\frac{2(-1)^m\left(3-\alpha_m^2\right)}{\alpha_m^5 \cosh\left(\alpha_m\right)}. \tag{3.40}$$

Thus, the solution to the problem described by Eqs. (3.31) to (3.33) is now fully determined. An alternative solution, expressed in the form of a double series, is provided in the Appendix A.1.

Substituting Eq. (3.40) into Eq. (3.37), and subsequently using the result in Eq. (3.34), we get

$$Q=\frac{8}{7}-72 \sum_{m=1}^{\infty} \frac{\tanh\left(\alpha_m\right)}{\alpha_m^9} \approx 0.0086. \tag{3.41}$$

Finally, using relations in Eqs. (3.35), (3.36), and (3.41), the friction factor–Reynolds number product (3.6) can be computed as

$$fRe \approx 14.9731. \tag{3.42}$$

3.3.2 Parabolic lens

3.3.2.1 $\lambda \ll 1$ or $\lambda \gg 1$

For the parabolic lens-shaped duct, in the limit as $\lambda \to 0$, the perturbation approach is analogous to that used for the parabolic segment. Consequently, equations (3.13) through (3.20) remain valid, with the exception of the boundary conditions (3.17) and (3.18), which, in this case, are replaced by

$$w_0\left(x, \eta=-\left(1-x^2\right)\right)=0 \tag{3.43}$$

and

$$w_2\left(x, \eta=-\left(1-x^2\right)\right)=0. \tag{3.44}$$

Solving Eqs. (3.15) and (3.16) subject to the boundary conditions (3.19), (3.20), (3.43), and (3.44), we obtain

$$w_0=-\frac{1}{2}\left[\eta^2-\left(1-x^2\right)^2\right] \tag{3.45}$$

and

$$w_2 = \left(1 - 3x^2\right)\left[\eta^2 - \left(1 - x^2\right)^2\right]. \tag{3.46}$$

Consequently,

$$Q = \lambda^3 \int_{-1}^{1} \int_{-(1-x^2)}^{1-x^2} \left[w_0\left(x,\eta\right) + \lambda^2 w_2\left(x,\eta\right) + \ldots\right] \mathrm{d}\eta\, \mathrm{d}x = \frac{64\lambda^3}{105} - \frac{256\lambda^5}{315} + O\left(\lambda^7\right). \tag{3.47}$$

and, using Eqs. (3.6), (3.11) and (3.12), we get

$$fRe = \frac{140}{9} + O\left(\lambda^4\right), \tag{3.48}$$

from which follows that

$$\lim_{\lambda\to 0} fRe = \frac{140}{9} \approx 15.5556. \tag{3.49}$$

Likewise, for the parabolic lens in the limit $\lambda \gg 1$, we employ the Maclaine–Cross formula [99] to obtain

$$\lim_{\lambda\to\infty} fRe = \lim_{\lambda\to\infty} \frac{96}{P^2} \frac{\left(\int_{-\lambda}^{0} 2\sqrt{1+\frac{y}{\lambda}}\,\mathrm{d}y + \int_{0}^{\lambda} 2\sqrt{1-\frac{y}{\lambda}}\,\mathrm{d}y\right)^3}{\int_{-\lambda}^{0}\left(2\sqrt{1+\frac{y}{\lambda}}\right)^3 \mathrm{d}y + \int_{0}^{\lambda}\left(2\sqrt{1-\frac{y}{\lambda}}\right)^3 \mathrm{d}y} = \frac{160}{9} \approx 17.7778. \tag{3.50}$$

3.3.2.2 $\lambda = 0.5$

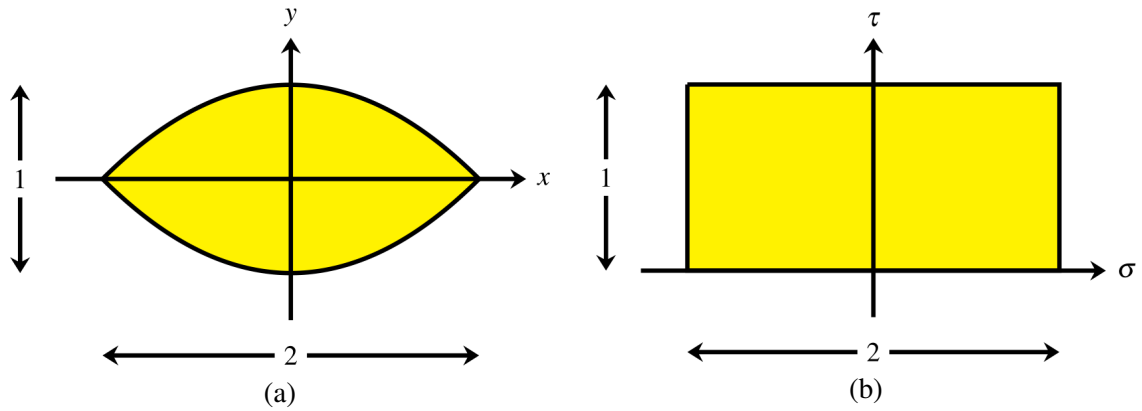

Figure 3.3: Mapping of the parabolic lens in the (x, y)-plane (a) to a rectangle in the (σ, τ)-plane (b).

By employing parabolic coordinates (3.27), the parabolic lens in the (x, y)-plane is mapped onto a rectangle in the (σ, τ)-plane, as depicted in Figure 3.3. The governing equation is the Poisson equation (3.31), and the boundary conditions (3.4) and (3.9) are instead given by

$$\frac{\partial w}{\partial \tau}\left(\sigma, \tau = 0\right) = 0, \tag{3.51}$$

$$w\left(\sigma = \pm 1, \tau\right) = 0, \tag{3.52}$$

and

$$w\left(\sigma, \tau = 1\right) = 0. \tag{3.53}$$

It is important to draw attention to the fact that the boundary condition (3.51) arises from the symmetry of the flow about the y-axis. This time we seek a solution to Eq. (3.31) of the form

$$w = \frac{1}{2}\left(1 + \sigma^2\right)\left(1 - \tau^2\right) + \sum_{m=1}^{\infty} W_m \cosh\left(\alpha_m \sigma\right) \cos\left(\alpha_m \tau\right), \tag{3.54}$$

where α_m is given by Eq. (3.38). As in the previous case, the first term in Eq. (3.54) is a particular solution of Eq. (3.31), while the second term has zero Laplacian. Moreover, it is straightforward to verify that this solution satisfies the boundary conditions (3.51) and (3.53). The no-slip condition (3.52) requires that

$$1 - \tau^2 + \sum_{m=1}^{\infty} W_m \cosh\left(\alpha_m\right) \cos\left(\alpha_m \tau\right) = 0. \tag{3.55}$$

From the orthogonality of the cosine function, it follows that

$$W_m = \frac{4(-1)^m}{\alpha_m^3 \cosh \alpha_m}. \tag{3.56}$$

Appendix A.2 provides an alternative solution to this problem, expressed as a double series.

The dimensionless volumetric flow rate (3.5) becomes

$$Q = \int_0^1 \int_{-1}^1 w\left(\sigma^2 + \tau^2\right) \mathrm{d}\sigma \, \mathrm{d}\tau, \tag{3.57}$$

and by substituting (3.54) into it, we find

$$Q = \frac{8}{5} - 16 \sum_{m=1}^{\infty} \frac{\tanh\left(\alpha_m\right)}{\alpha_m^5} \approx 0.0579. \tag{3.58}$$

Since

$$A = \frac{4}{3}, \tag{3.59}$$

and

$$P = 2\left[\sqrt{2} + \ln\left(1 + \sqrt{2}\right)\right], \tag{3.60}$$

for $\lambda = 0.5$, the corresponding friction factor–Reynolds number product (3.6) is

$$fRe \approx 15.5242. \tag{3.61}$$

3.4 Numerical solution

The Poisson equation (3.1), subject to Dirichlet boundary conditions for the parabolic segment (Eqs. (3.3) and (3.4)) and the lens (Eqs. (3.4) and (3.9)), was solved using the finite element method (FEM) implemented in the open-source software FreeFem [102]. The two-dimensional fluid domains depicted in Figure 3.1 were discretized using P_2 triangular finite elements. FreeFem's automatic mesh generation, based on the Delaunay-Voronoi algorithm, was employed. The volumetric flow rate (Eqs. (3.5) and (3.10)) was computed using Gaussian quadrature via the `int2d` function in FreeFem.

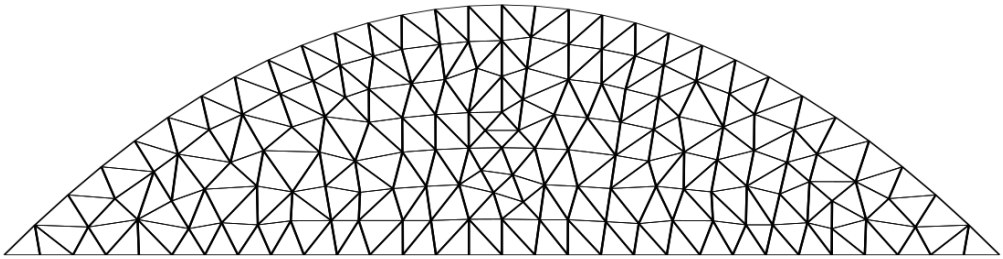

Figure 3.4: Example of a coarse triangular mesh for the parabolic segment duct at $\lambda = 0.5$.

Table 3.2: Absolute (ϵ_{abs}) and relative errors (ϵ_{rel}) as a function of the number of elements (N) at $\lambda = 0.5$ for the fRe for the parabolic segment duct.

N	1,012	10,092	100,470	200,076	400,295	800,891
ϵ_{abs}	2.80×10^{-3}	2.87×10^{-4}	2.42×10^{-5}	9.42×10^{-6}	2.01×10^{-6}	1.78×10^{-6}
ϵ_{rel} (%)	1.87×10^{-2}	1.92×10^{-3}	1.62×10^{-4}	6.28×10^{-5}	1.34×10^{-5}	1.20×10^{-5}

Table 3.3: Absolute (ϵ_{abs}) and relative errors (ϵ_{rel}) as a function of the number of elements (N) at $\lambda = 0.5$ for the fRe for the lens-shaped duct.

N	1,004	10,062	101,098	201,306	401,440	800,134
ϵ_{abs}	5.59×10^{-3}	5.71×10^{-4}	4.78×10^{-5}	1.76×10^{-5}	2.40×10^{-6}	1.79×10^{-6}
ϵ_{rel} (%)	3.60×10^{-2}	3.68×10^{-3}	3.08×10^{-4}	1.13×10^{-4}	1.54×10^{-5}	1.19×10^{-5}

The problem was solved using LU decomposition. Figure 3.4 presents an example of a computational mesh used in the simulations. For visualization purposes, a coarse mesh with only 288 triangles is shown. However, to ensure the robustness of the results, approximately 800,000 triangular elements were initially employed. Further analysis revealed that the desired level of precision could be achieved with significantly fewer elements, with around 100,000 being sufficient to guarantee four-digit accuracy.

To validate our numerical solution, we compared it against the analytical values of the friction factor–Reynolds product presented in Sec. 3.3 for $\lambda = 0.5$ for both parabolic segment and lens-shaped ducts (Eqs. (3.49) and (3.61), respectively). This comparison is documented in Table 3.2 and Table 3.3, which illustrate the behaviour of the parameter of interest, fRe, as the number of triangular elements increases.

A slight variation in error was observed for the lens-shaped duct beyond 100,000 elements, suggesting a potential convergence threshold for the numerical solution. Nonetheless, for the purposes of this study, this level of accuracy is deemed sufficient.

3.5 Results

The normalised velocity contours for $\lambda = 1$ are shown in panels (a) and (b) of Figure 3.5 for the parabolic segment duct and the lens-shaped duct, respectively. The contours range from 0 to $0.9w_{\max}$ in increments of $0.1w_{\max}$, where $w_{\max}$ is the maximum dimensionless axial velocity.

The relationship between the dimensionless volumetric flow rate (Q) and the aspect ratio (λ) for the parabolic segment duct is shown in panel (a) of Figure 3.6, while for the lens-shaped duct it is shown in panel (b). In both cases, Q starts at zero when $\lambda = 0$ and increases monotonically as λ rises, reaching its maximum value at $\lambda = 1$. Notably, the maximum flow rate in the lens-shaped duct (0.2776) is substantially higher than that in the parabolic segment duct (0.0533), reflecting the greater flow capacity of the lens geometry. For small values of λ, the growth in Q is gradual for both geometries, becoming more pronounced as λ approaches 1. For instance, in the parabolic segment duct, Q increases from 0.0086 at $\lambda = 0.5$ to 0.0411 at $\lambda = 0.9$, while in the lens-shaped duct, the growth follows a similar pattern, rising from 0.0579 at $\lambda = 0.5$ to 0.2237 at $\lambda = 0.9$. Despite these differences, the asymptotic solution derived using perturbation methods performs well in both cases for small λ. While its accuracy decreases as λ increases, it remains reasonably close to the numerical solution even beyond its theoretical range of validity. For example, in the parabolic segment duct, the error is approximately 5% at $\lambda = 0.7$ and below 15% at $\lambda = 0.9$, similarly, for the lens-shaped duct, the error is around 1% at $\lambda = 0.3$ and remains under 13% at $\lambda = 0.5$. Both geometries demonstrate excellent agreement between numerical and analytical solutions for the analytical results at $\lambda = 0.5$, as expected.

The friction factor–Reynolds number product (fRe) as a function of the aspect ratio (λ) is shown in panels (a) and (b) of Figure 3.7 for the parabolic segment duct and the lens-shaped duct, respectively. The corresponding values for the parabolic segment duct are tabulated in Table 3.4, while those for the lens-shaped duct are in Table 3.5. For the parabolic segment duct, the relationship starts at $fRe = 15.5556$ when $\lambda = 0$ and follows a monotonically decreasing trend as λ increases, reaching a minimum of 14.4807 at $\lambda = 1$, with intermediate values such as 14.9731 at $\lambda = 0.5$. In contrast, for the lens-shaped duct, the fRe product also starts at 15.5556 for $\lambda = 0$, but decreases until it reaches a minimum of 15.5241 at $\lambda = 0.49$ (noting that λ was varied in increments of 0.01, so this was the lowest value found), after which fRe increases, reaching a maximum of 15.7264 at $\lambda = 1$. However, the overall variation of fRe in the lens-shaped duct is quite small, which is consistent with observations in [100], where the fRe product was found to be insensitive to aspect ratio

for a circular lens duct. For both ducts, the solid line represents the numerical solution obtained via the finite element method, while the dashed line corresponds to the asymptotic solution. Although the graphical appearance in Figure 3.6 might suggest that the asymptotic solution has a broader validity range for the dimensionless volumetric flow rate, its accuracy diminishes as λ increases. In the parabolic segment duct, the error is less than 1% at $\lambda = 0.4$, grows to around 6% at $\lambda = 0.7$, and reaches approximately 12% at $\lambda = 0.9$. For the lens-shaped duct, the variation in the fRe error is relatively small, with values of approximately 0.2% at $\lambda = 0.4$, decreasing to 0.03% at $\lambda = 0.7$, and then increasing to 0.7% at $\lambda = 0.9$. The circle marker in the parabolic segment duct analysis indicates the analytical solution at $\lambda = 0$, derived from Eq. (3.25), and the square marker at $\lambda = 0.5$ corresponds to Eq. (3.42). For the lens-shaped duct, the analytical solutions at $\lambda = 0$ and $\lambda = 0.5$ are given by Eq. (3.49) and Eq. (3.61), respectively. For context, for singly connected ducts, the friction factor–Reynolds number product ranges from 6.486 for an n-sided cusped duct (as n approaches infinity) to 24 for parallel plates [103]. For a circular duct, the value of fRe is 16 (see, e.g., [104]).

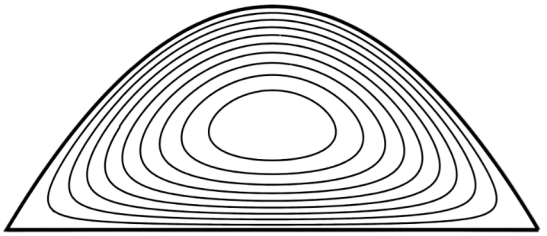

(a)

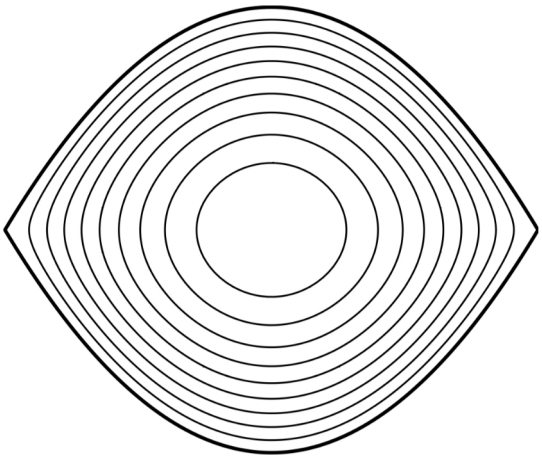

(b)

Figure 3.5: Normalised velocity contour lines for $\lambda = 1$, shown for the parabolic segment duct in panel (a) and the lens-shaped duct in panel (b). Contour levels from the outermost to the innermost are 0.1, 0.2, . . ., 0.9.

To improve the precision of the fRe approximation for both the parabolic segment duct and the lens-shaped duct, the values presented in Tables 3.4 and 3.5 respectively can be accurately represented by fifth-degree polynomial fits. Both polynomials share the factor $\frac{140}{9}$, which originates from the analytical solution at $\lambda = 0$. The coefficients of the polynomials were determined using the least squares method. For the parabolic segment duct, the

polynomial is given by

$$fRe = \frac{140}{9}\left(1 + 0.0047\lambda - 0.2862\lambda^2 + 0.2830\lambda^3 - 0.0435\lambda^4 - 0.0273\lambda^5\right), \tag{3.62}$$

which achieves an error margin of less than 0.03% across the entire range of aspect ratios λ. Similarly, for the lens-shaped duct, the friction factor–Reynolds number product (fRe) is approximated by the polynomial

$$fRe = \frac{140}{9}\left(1 + 0.0027\lambda - 0.0197\lambda^2 - 0.0394\lambda^3 + 0.1421\lambda^4 - 0.0749\lambda^5\right), \tag{3.63}$$

which approximates the values in Table 3.5 with a deviation of less than 0.02%.

Following the analysis for $\lambda < 1$, we now turn to the case of large aspect ratios ($\lambda > 1$). The behaviour of the friction factor–Reynolds number product was investigated numerically for both geometries. The results are summarised in Tables 3.6 and 3.7 and plotted in Figure 3.8. In both cases, the numerical data were fitted with fifth-degree polynomials in λ^{-1} that accurately reproduce the tabulated values. For the parabolic segment duct, the fitted polynomial is

$$fRe = \frac{160}{9}\left(1 - 0.4643\lambda^{-1} - 0.3131\lambda^{-2} + 2.0729\lambda^{-3} - 2.3351\lambda^{-4} + 0.8551\lambda^{-5}\right), \tag{3.64}$$

while for the lens-shaped duct it is

$$fRe = \frac{160}{9}\left(1 - 0.0284\lambda^{-1} - 0.7452\lambda^{-2} + 1.5761\lambda^{-3} - 1.3568\lambda^{-4} + 0.4394\lambda^{-5}\right). \tag{3.65}$$

The maximum relative error between each polynomial and the corresponding numerical data is 0.13% for the parabolic segment duct and 0.06% for the lens-shaped duct. The analytical value at $\lambda^{-1} = 0$ ($\lambda \to \infty$), obtained from the Maclaine–Cross formula [99], is $fRe = 160/9 \approx 17.7778$ for both geometries, as indicated by the triangular markers. In the parabolic segment duct, fRe decreases as λ^{-1} increases from 0 to 0.8, reaching 14.4474, and then rises slightly to 14.4806 at $\lambda^{-1} = 1$. In the lens-shaped duct, fRe decreases more gradually with λ^{-1}, from 17.7778 at $\lambda^{-1} = 0$ to 15.7263 at $\lambda^{-1} = 1$.

For practical applications, it may be of interest to compare the values of fRe for the two geometries across the full range of λ. Both geometries yield the same value in the limiting cases $\lambda \to 0$ and $\lambda \to \infty$, but the value for the lens-shaped duct is never smaller than that for the parabolic segment duct at the same λ. The largest difference occurs at $\lambda \approx 1.90$, where the lens-shaped duct exhibits about 11.54% higher fRe.

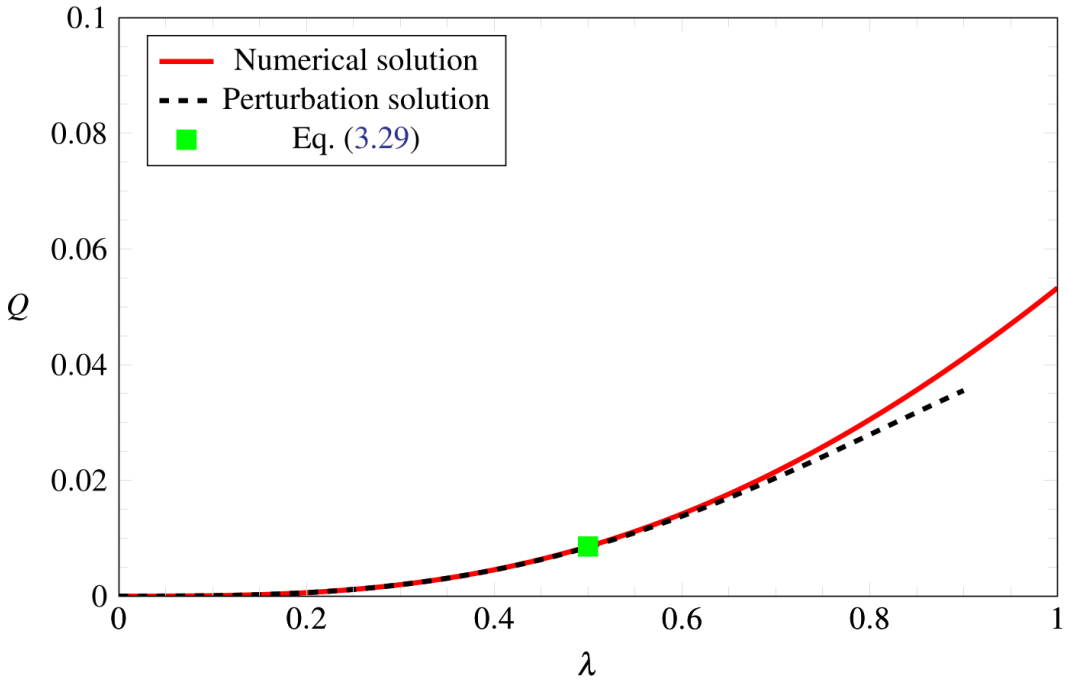

(a)

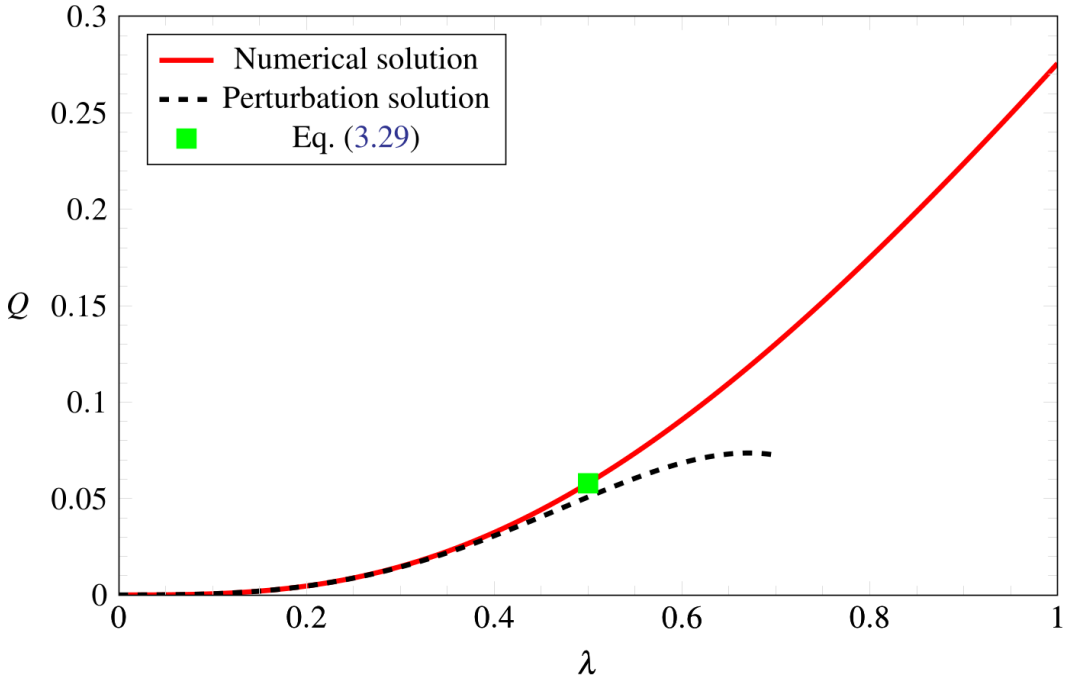

(b)

Figure 3.6: Dimensionless volumetric flow rate as a function of λ for the parabolic segment duct in panel (a) and the lens-shaped duct in panel (b).

3.6 Conclusion

A novel solution has been presented for steady Poiseuille flow in parabolic segment and lens-shaped ducts. In both cases, asymptotic solutions were derived for $\lambda \to 0$ (thin ducts), while analytical solutions in parabolic coordinates were obtained for $\lambda = 0.5$. For $\lambda \to \infty$, the analysis was reformulated in terms of λ^{-1}, and corresponding limiting values of the friction

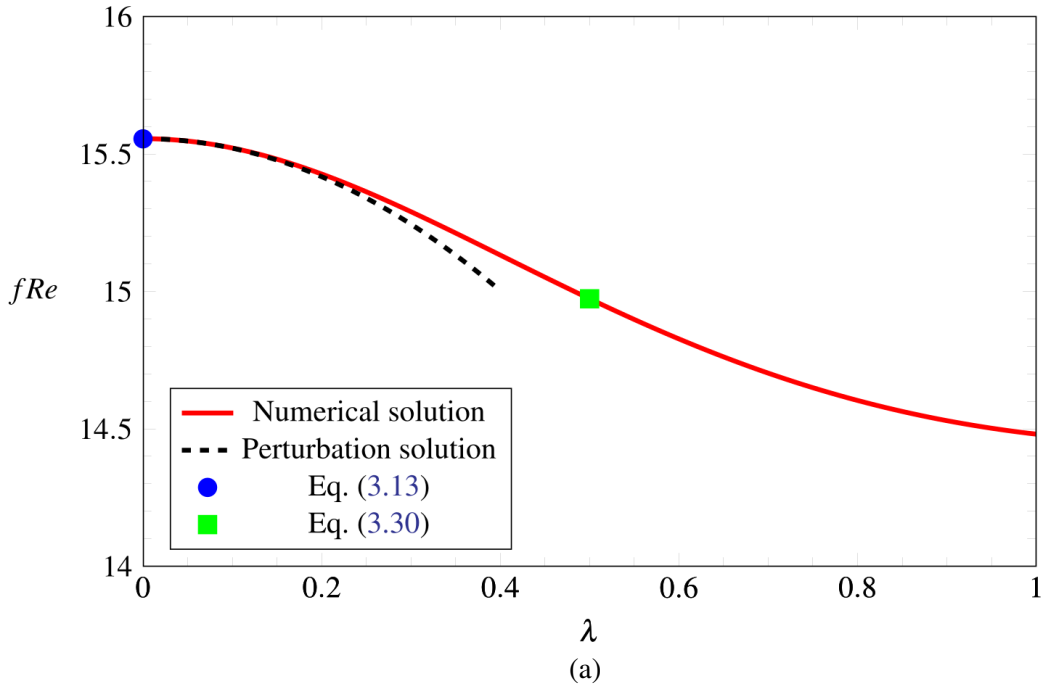

(a)

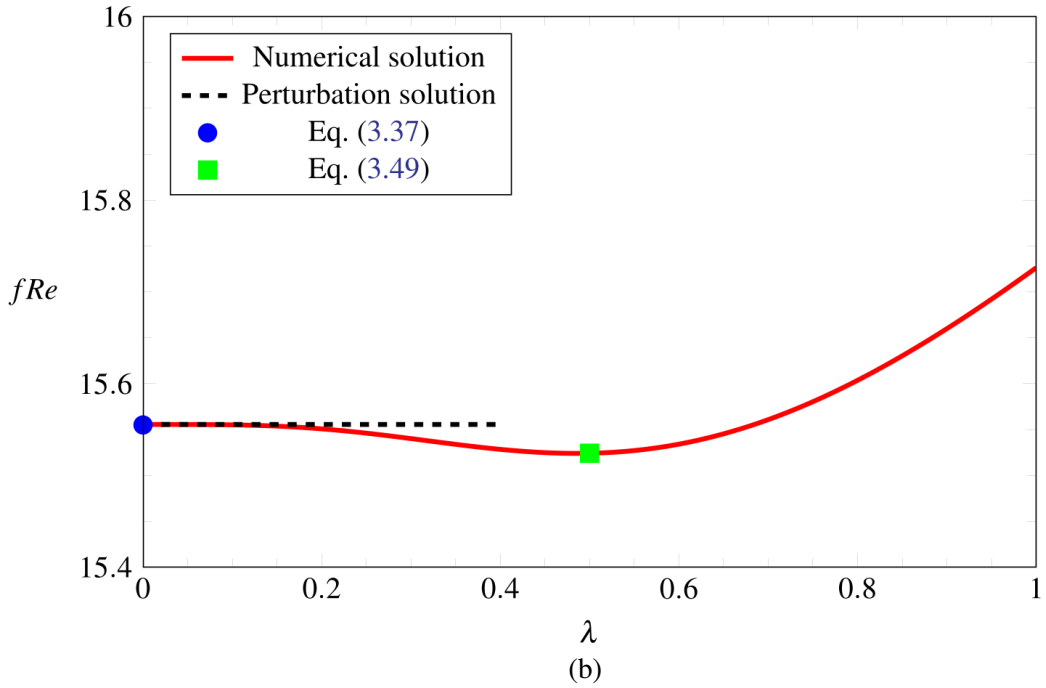

(b)

Figure 3.7: Friction factor–Reynolds number product as a function of λ for the parabolic segment duct in panel (a) and the lens-shaped duct in panel (b).

factor–Reynolds number product were computed using the Maclaine–Cross formula [99]. Explicit expressions have been provided for the velocity field, volumetric flow rate, and the friction factor–Reynolds number product. To investigate other aspect ratios, the finite element method was employed. The results confirm the effectiveness of the proposed solutions across a wide range of aspect ratios. In both geometries, the volumetric flow rate increases monotonically with λ. In contrast, the friction factor–Reynolds number product follows distinct trends: for the parabolic segment duct, it decreases monotonically for $0 < \lambda \leq 1$ and then

Table 3.4: fRe values for parabolic segment ducts as a function of λ.

λ	fRe
0	15.5556*
0.1	15.5217
0.2	15.4270
0.3	15.2899
0.4	15.1321
0.5	14.9731*
0.6	14.8272
0.7	14.7026
0.8	14.6033
0.9	14.5298
1	14.4807

Analytic solutions are indicated by asterisks.

Table 3.5: fRe values for parabolic lens-shaped ducts as a function of λ.

λ	fRe
0	15.5556*
0.1	15.5551
0.2	15.5508
0.3	15.5402
0.4	15.5284
0.5	15.5242*
0.6	15.5341
0.7	15.5608
0.8	15.6037
0.9	15.6599
1	15.7264

Analytic solutions are indicated by asterisks.

increases, non-monotonically, for $\lambda \geq 1$, reaching a maximum of 14.4806 at $\lambda = 1$; for the lens-shaped duct, it increases non-monotonically for $0 < \lambda \leq 1$ and increases monotonically for $\lambda \geq 1$, attaining a maximum of 17.7778 as $\lambda \to \infty$. Polynomial approximations were obtained separately for $0 < \lambda \leq 1$ and for $\lambda \geq 1$ (expressed in terms of λ^{-1}), achieving relative errors below 0.02% and 0.12% for the parabolic segment, and below 0.5% and 0.05% for the lens-shaped duct. The perturbation solution, developed for $0 < \lambda \leq 1$, remains accurate even

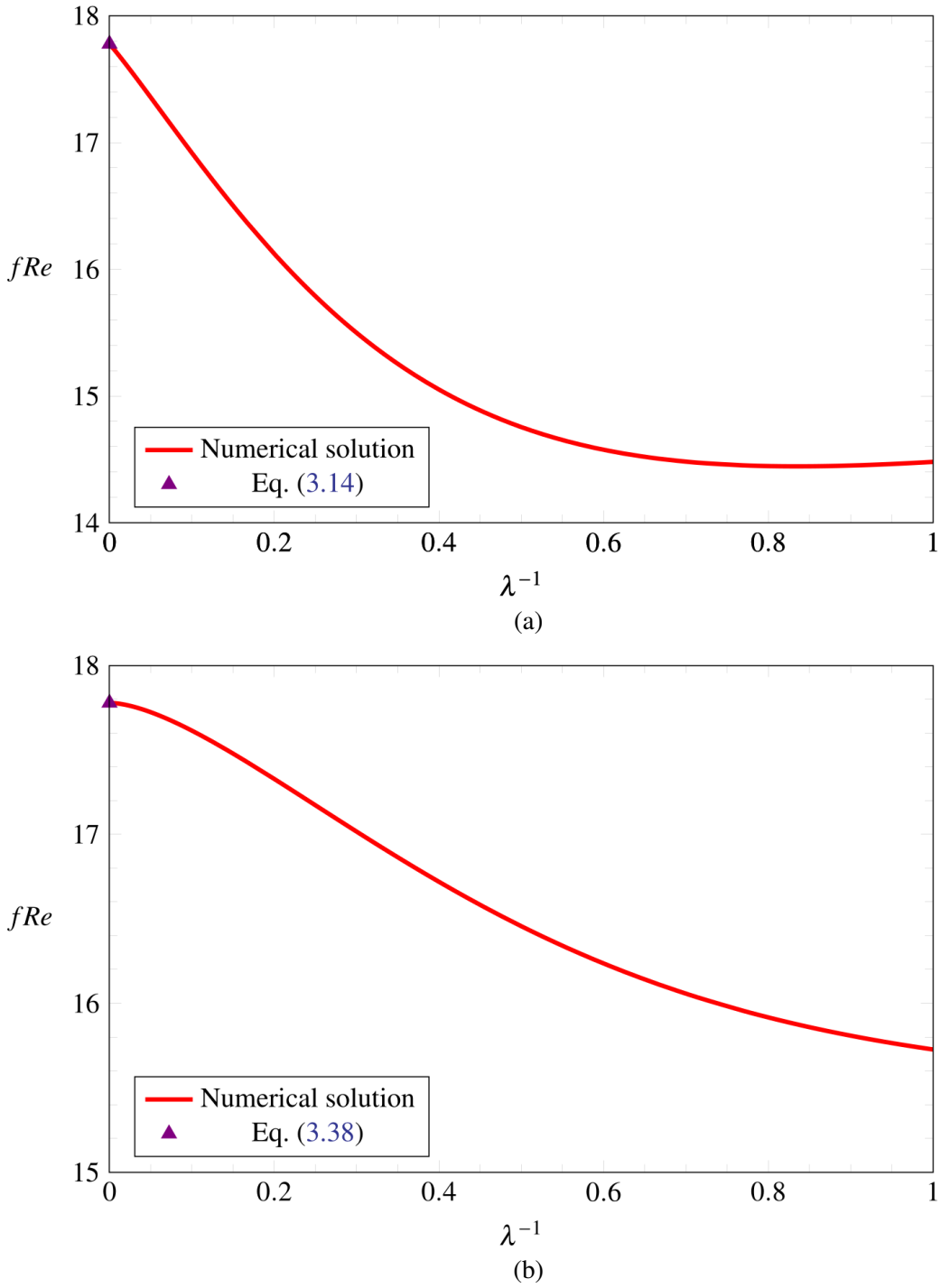

Figure 3.8: Friction factor–Reynolds number product as a function of λ^{-1} for the parabolic segment duct in panel (a) and the lens-shaped duct in panel (b).

beyond its theoretical range of validity.

It is important to emphasise that the results presented in this study extend beyond the specific context of Poiseuille flow. Governed by the two-dimensional Poisson equation with a constant source term and homogeneous Dirichlet boundary conditions, these findings apply broadly to analogous physical phenomena across disciplines. In fluid mechanics, they offer insights into circulating flows in tubes of constant vorticity and groundwater flows driven

Table 3.6: fRe values for parabolic segment ducts as a function of λ^{-1}.

λ^{-1}	fRe
0	17.7778*
0.1	16.9185
0.2	16.1229
0.3	15.4988
0.4	15.0514
0.5	14.7550
0.6	14.5760
0.7	14.4822
0.8	14.4474
0.9	14.4517
1	14.4806

Analytic solutions are indicated by asterisks.

Table 3.7: fRe values for parabolic lens-shaped ducts as a function of λ^{-1}.

λ^{-1}	fRe
0	17.7778*
0.1	17.6138
0.2	17.3279
0.3	17.0161
0.4	16.7189
0.5	16.4561
0.6	16.2353
0.7	16.0566
0.8	15.9161
0.9	15.8080
1	15.7263

Analytic solutions are indicated by asterisks.

by precipitation. In solid mechanics, they describe torsion and bending of elastic beams as well as the deflection of membranes, menisci, and soap bubbles. In heat and mass transfer, the results address resistive heating in electrical wires, viscous dissipation, and reaction-diffusion in catalyst rods. They also extend to stochastic processes, such as first-passage times and diffusion-controlled reactions, and to electromagnetism, modelling electrostatic and magnetic vector potentials. Furthermore, they inform studies of electrokinetic phenom-

ena, including electro-osmotic flow and streaming currents in porous media. Inspired by Bazant's classification of analogous problems [105], these diverse applications highlight the broad applicability and interdisciplinary significance of the solutions presented in this work.

Finally, we note that the analytical framework developed here can also be applied to flows in ducts with slowly varying cross-sections, which have been extensively studied in the literature [106, 107, 108, 109, 110].

A Alternative solutions

In this appendix, we solve the Poiseuille flow through parabolic segment and lens-shaped ducts using an alternative approach: the eigenfunction expansion method.

A.1 Parabolic segment

The general solution to the Poisson equation in the right isosceles triangle shown in panel (b) of Figure 3.2, with homogeneous Dirichlet boundary conditions, is given by (e.g., [111])

$$w = \sum_{m=1}^{\infty}\sum_{n=1}^{\infty} W_{mn}\varphi_{mn}, \tag{3.66}$$

where W_{mn} are unknown coefficients, and

$$\varphi_{mn} = \cos\left[\left(\alpha_m + \beta_n\right)\sigma\right]\cos\left[\left(\alpha_m - \beta_n\right)\tau\right] - \cos\left[\left(\alpha_m - \beta_n\right)\sigma\right]\cos\left[\left(\alpha_m + \beta_n\right)\tau\right]. \tag{3.67}$$

Here, α_m is given by Eq. (3.38) and

$$\beta_n = \pi n. \tag{3.68}$$

Now, we substitute Eq. (3.66) into the Poisson equation (3.31), to find that

$$2\sum_{m=1}^{\infty}\sum_{n=1}^{\infty}\left(\alpha_m^2 + \beta_n^2\right) W_{mn}\varphi_{mn} = \sigma^2 + \tau^2. \tag{3.69}$$

After multiplying Eq. (3.69) by φ_{ij}, integrating over the cross-section, and using orthogonality, W_{mn} is isolated in the equation, giving

$$W_{mn} = -\frac{2}{\left(\alpha_m^2 - \beta_n^2\right)}\left[\frac{1}{\alpha_m\beta_n} - \frac{\beta_n}{\alpha_m^3\left(\alpha_m^2 + \beta_n^2\right)} - \frac{\alpha_m\beta_n}{2\left(\alpha_m^2 + \beta_n^2\right)\left(\alpha_m^2 - \beta_n^2\right)^2}\right]. \tag{3.70}$$

Plugging Eq. (3.70) into Eq. (3.66) and then applying the resulting expression to Eq. (3.34), we obtain

$$Q = 4\sum_{m=1}^{\infty}\sum_{n=1}^{\infty}\frac{\alpha_m^2 + \beta_n^2}{\left(\alpha_m^2 - \beta_n^2\right)^2}\left[\frac{1}{\alpha_m\beta_n} - \frac{\beta_n}{\alpha_m^3\left(\alpha_m^2 + \beta_n^2\right)} - \frac{8\alpha_m\beta_n}{\left(\alpha_m^2 + \beta_n^2\right)\left(\alpha_m^2 - \beta_n^2\right)^2}\right]^2, \tag{3.71}$$

or, equivalently,

$$Q = \frac{11}{1260} - \frac{9}{2}\sum_{n=1}^{\infty}\frac{\tanh\left(\beta_n\right)}{\beta_n^9} \approx 0.0086, \tag{3.72}$$

in agreement with Eq. (3.41), as expected.

A.2 Parabolic lens

To satisfy all four boundary conditions in Eqs. (3.51) to (3.53), we propose a solution of the form

$$w = \sum_{m=1}^{\infty}\sum_{n=1}^{\infty} W_{mn}\varphi_{mn}, \tag{3.73}$$

where

$$\varphi_{mn} = \cos\left(\alpha_m\sigma\right)\cos\left(\alpha_n\tau\right), \tag{3.74}$$

and α_m is defined as in Eq. (3.38). To find W_{mn}, we substitute Eq. (3.73) into the Poisson equation (3.31), yielding

$$\sum_{m=1}^{\infty}\sum_{n=1}^{\infty}\left(\alpha_m^2 + \alpha_n^2\right)W_{mn}\varphi_{mn} = \sigma^2 + \tau^2. \tag{3.75}$$

By multiplying both sides of the previous equation by φ_{ij} and integrating over the rectangle shown in panel (b) of Figure 3.3, we can isolate W_{mn}, yielding

$$W_{mn} = \frac{8\left(-1\right)^{m+n}}{\alpha_m\alpha_n\left(\alpha_m^2 + \alpha_n^2\right)}\left(1 - \frac{1}{\alpha_m^2} - \frac{1}{\alpha_n^2}\right). \tag{3.76}$$

From Eqs. (3.57), (3.73), and (3.76), we obtain the following expression for the volumetric flow rate

$$Q = 32\sum_{m=1}^{\infty}\sum_{n=1}^{\infty}\frac{\alpha_m^2 + \alpha_n^2}{\alpha_m^4\alpha_n^4}\left[\frac{1}{\alpha_m^2\alpha_n^2} - \frac{2}{\alpha_m^2 + \alpha_n^2} + \frac{\alpha_m^2\alpha_n^2}{\left(\alpha_m^2 + \alpha_n^2\right)^2}\right], \tag{3.77}$$

which can be rewritten as

$$Q = \frac{8}{5} - 16\sum_{m=1}^{\infty}\frac{\tanh\left(\alpha_m\right)}{\alpha_m^5} \approx 0.0579, \tag{3.78}$$

in accordance with Eq. (3.58).

Chapter 4

Revisiting Poiseuille flow through lens-shaped and figure-eight ducts

This chapter is a reproduction of the following publication:

Silva, V. C.; Lopes, A.B. Revisiting Poiseuille flow through lens-shaped and figure-eight ducts. Mechanics Research Communications, Vol. 150, Article 104570, 2025.

4.1 Introduction

Lens-shaped ducts are bounded by two equal circular arcs that meet at two points to form a single lobe, whereas figure-eight ducts consist of two lobes joined at a waist [3, 112]. In practice, the former arise in compact internal-flow hardware such as conformal-cooling channels and tightly packed heat-exchanger passages; related narrow-gap configurations also occur in subsurface hydraulics and physiology (e.g. fissures in hydraulic fracturing and inter-endothelial clefts lined with adhesive and protein layers), providing a practical context for lens-type passages and for crevice formulations developed in recent analyses [113, 114]. The latter belong to a broader class of multi-lobed passages for which recent studies have mapped thermo-hydraulic trade-offs [115, 116, 117]. More broadly, Poiseuille flow in non-circular ducts is part of a well-developed class of exact steady Navier–Stokes solutions governed by the Dirichlet problem for Poisson's equation with constant forcing; in this setting, Bazant [118] identifies seventeen physical analogies spanning fluid/solid mechanics, heat and mass transfer, stochastic processes, electromagnetism and electrokinetics. Wang's review [119] emphasises that such solutions, though scarce, represent fundamental flows whose uniformly valid structure clarifies basic phenomena and serves as a standard for assessing numerical, asymptotic and empirical methods.

The fully filled literature for these geometries is sparse compared with the partially filled case. In the antecedent problem of a partially filled circular pipe, Guo and Meroney [120] used bipolar coordinates, enforced no-slip at the wall and zero shear at the free surface,

applied a cosine Fourier transform, and obtained integral representations for the velocity field, the volumetric flow rate and wall stresses. Fullard and Wake [121] worked in the same bipolar setting but solved the strip problem differently, using an exponential Fourier transform to obtain an analytical series for the velocity distribution. Experimentally, Ng et al. [122] examined laminar and turbulent flows in partially filled pipes, observing strong agreement with theory in laminar flow. In the fully filled setting, Wang [3] analysed the lens geometry using an accurate Ritz method and perturbations about the circular and thin limits, reported the volumetric flow rate, and tabulated the Poiseuille number as a function of thickness ratio. Using the series of Fullard and Wake [121], together with a symmetry argument, Irvine and Fullard [112] showed that the no-slip solution extends to fully filled lens and figure-eight ducts and discussed applications in compact internal flows employing non-circular passages.

The aim of this paper is to revisit fully filled lens-shaped and figure-eight ducts and close several gaps. We derive, for the first time, an explicit analytical representation for the volumetric flow rate across the lens–figure-eight family and, from it, an explicit form for the Poiseuille number. We also report rare closed-form evaluations at special angles; because such closed forms are uncommon, we propose their use as stringent benchmarks for numerical solvers and verification studies. In addition, we present the Poiseuille number for the figure-eight geometry, extending prior lens-only tabulations [3]. By the same symmetry considerations described by Irvine and Fullard [112], the representation obtained here also informs the partially filled circular-pipe problem. From a practical standpoint, we emphasise the Poiseuille number because, in steady, fully developed laminar flow, it equals the product of the Fanning friction factor and the Reynolds number; this quantity is used directly for pressure-drop prediction and is the form tabulated in standard design compilations such as Shah and London [33] and Rohsenow, Hartnett and Cho [123], and it underpins modern scaling and modelling of laminar pressure drop in non-circular ducts [124]. In microchannel studies, geometry exerts a systematic influence on hydraulic resistance across broad families of shapes [125], and practical correlations estimate friction losses from simple geometric measures, including area, perimeter and the polar moment of inertia of the cross-section [126]. Our exact analysis establishes benchmarks for lens and figure-eight sections and enables the assessment and calibration of geometry-based correlations.

This work is organised as follows. Section 4.2 formulates the lens–figure-eight problem in bipolar coordinates. Section 4.3 presents an explicit analytical representation for the volumetric flow rate, derives the associated Poiseuille number, and records closed-form evaluations at special angles together with asymptotic expansions about limiting geometries. Section 4.4 analyses and discusses the results and proposes a compact Padé approximant for the Poiseuille number. Section 4.5 summarises the main conclusions.

4.2 Formulation

We consider steady, fully developed flow of an incompressible Newtonian fluid with viscosity μ through a duct of width $2L$ and aspect ratio b, whose cross-section is lens-shaped for $b < 1$, circular at $b = 1$, and figure-eight for $b > 1$. The axial pressure gradient is uniform, $G = -\mathrm{d}p/\mathrm{d}z > 0$. Lengths are scaled by L and the velocity by GL^2/μ. The axial velocity $w(x, y)$ is governed by the Poisson equation

$$\nabla^2 w = -1, \tag{4.1}$$

subject to the no-slip condition

$$w = 0 \tag{4.2}$$

on the arcs

$$x^2 + (y \pm c)^2 = c^2 + 1, \tag{4.3}$$

where

$$c = \frac{1 - b^2}{2b}. \tag{4.4}$$

Introduce bipolar coordinates (ξ, η) by

$$x + iy = i \cot\left(\frac{\eta + i\xi}{2}\right), \tag{4.5}$$

whose scale factors are

$$h_\xi = h_\eta = \frac{1}{\cosh\xi - \cos\eta}. \tag{4.6}$$

The arcs map to the straight lines $\eta = \pi \pm \alpha$, where

$$\alpha = \cos^{-1}\left(\frac{c}{\sqrt{c^2 + 1}}\right). \tag{4.7}$$

By symmetry, we work in the half-strip $\xi \geq 0$, $\pi \leq \eta \leq \pi + \alpha$. The geometry of the flow is sketched in Figure 4.1.

Using Eqs. (4.5) and (4.6), the problem described by Eqs. (4.1) and (4.2) becomes

$$(\cosh\xi - \cos\eta)^2 \left(\frac{\partial^2 w}{\partial \xi^2} + \frac{\partial^2 w}{\partial \eta^2}\right) = -1, \tag{4.8}$$

with boundary conditions

$$\begin{cases} w(\xi, \pi + \alpha) = 0, \\ \dfrac{\partial w}{\partial \eta}(\xi, \pi) = 0, \\ \dfrac{\partial w}{\partial \xi}(0, \eta) = 0, \\ w(\infty, \eta) = 0. \end{cases} \tag{4.9}$$

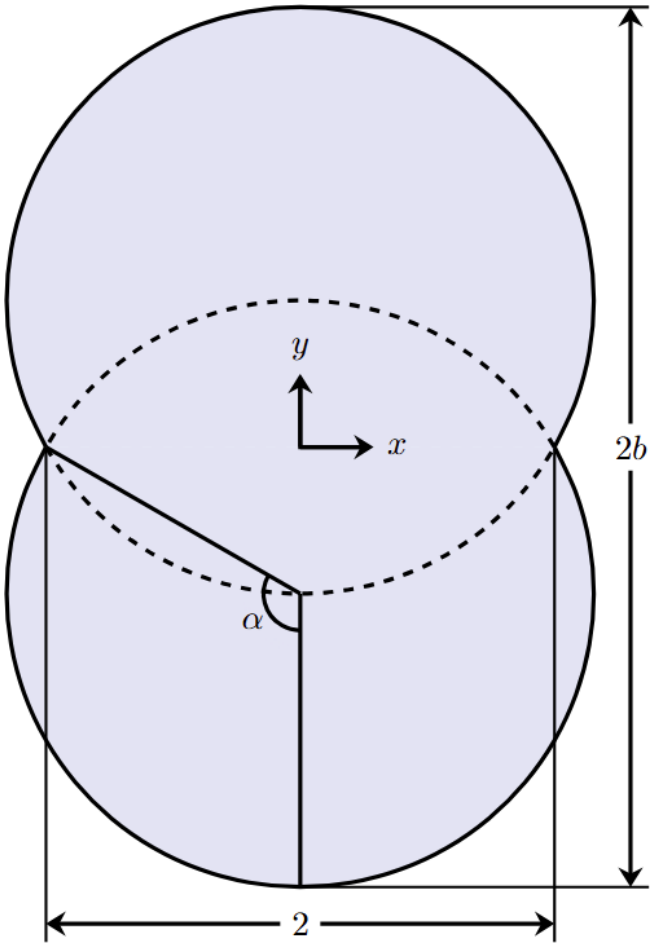

Figure 4.1: Flow geometry.

The Poiseuille number is given by

$$Po\,(\alpha) = \frac{8A^3}{P^2 Q}, \tag{4.10}$$

where A is the cross-sectional area,

$$A\,(\alpha) = 2\left(\alpha \csc^2 \alpha - \cot \alpha\right), \tag{4.11}$$

P is the wetted perimeter,

$$P\,(\alpha) = \frac{4\alpha}{\sin \alpha}, \tag{4.12}$$

and Q is the volumetric flow rate,

$$Q\,(\alpha) = 4 \int_0^{\pi+\alpha} \int_0^{\infty} \frac{w\,(\xi, \eta; \alpha)}{(\cosh \xi - \cos \eta)^2}\, \mathrm{d}\xi\, \mathrm{d}\eta, \tag{4.13}$$

respectively.

4.3 Solution

Before turning to the general lens-to-figure-eight family, we recall two benchmark solutions from the literature that we will use as reference. We begin with the circular limit $\alpha = \pi/2$ $(b = 1)$. In the unit disc $x^2 + y^2 < 1$, the solution of Eqs. (4.1) and (4.2) is the classical parabolic profile [82]:

$$w(x, y) = \frac{1 - x^2 - y^2}{4}. \tag{4.14}$$

The corresponding volumetric flow rate obtained from Eq. (4.13) is

$$Q\left(\frac{\pi}{2}\right) = \frac{\pi}{8}. \tag{4.15}$$

Evaluating Eqs. (4.11) and (4.12) at $\alpha = \pi/2$ gives

$$A\left(\frac{\pi}{2}\right) = \pi, \tag{4.16}$$

$$P\left(\frac{\pi}{2}\right) = 2\pi. \tag{4.17}$$

Substituting A, P, and Q into Eq. (4.10) yields

$$Po\left(\frac{\pi}{2}\right) = 16, \tag{4.18}$$

in agreement with Shah and London [33].

A second benchmark is the right-angle lens obtained in the context of the St. Venant torsion problem in elasticity by Sokolnikoff and Sokolnikoff [127] and later reported for duct flows by Wang [3]. It corresponds to $\alpha = \pi/4$ $\left(b = \sqrt{2} - 1\right)$ and is bounded by the arcs $x^2 + (y \pm 1)^2 = 2$. The solution reads

$$\begin{aligned} w(x, y) = {} & \frac{1 - x^2 - y^2}{4} + \frac{1}{2\pi\left(x^2 + y^2\right)\left[(1 + x^2 + y^2)^2 - 4y^2\right]} \\ & \times \Big\{\pi\left(x^2 + y^2\right)\left[\left(x^2 + y^2\right)^2 - 1\right] + x\left(1 + x^2 + y^2\right) \\ & \times \left[4y^2 - \left(1 - x^2 - y^2\right)^2\right]\ln R \\ & + y\left(1 - x^2 - y^2\right)\left[\left(1 + x^2 + y^2\right)^2 + 4x^2\right]\phi\Big\}, \end{aligned} \tag{4.19}$$

where

$$R = \frac{\sqrt{(1 - x^2 - y^2)^2 + 4y^2}}{(1 + x)^2 + y^2} \tag{4.20}$$

and

$$\phi = \tan^{-1}\left(\frac{2y}{1 - x^2 - y^2}\right). \tag{4.21}$$

From Eqs. (4.11) and (4.12) we obtain

$$A\left(\frac{\pi}{4}\right) = \pi - 2 \tag{4.22}$$

and

$$P\left(\frac{\pi}{4}\right) = \sqrt{2}\pi. \tag{4.23}$$

The volumetric flow rate is

$$Q\left(\frac{\pi}{4}\right) = \frac{3\pi}{4} - 2 - \frac{1}{\pi}, \tag{4.24}$$

and substitution into Eq. (4.10) yields

$$Po\left(\frac{\pi}{4}\right) = \frac{16\,(\pi-2)^3}{\pi\,(3\pi^2 - 8\pi - 4)} \approx 15.9159. \tag{4.25}$$

For completeness, we note that Greenwell and Wang [128] obtained a semi-analytical solution for the figure-eight configuration with $\alpha = 3\pi/4$ ($b = 1 + \sqrt{2}$) by mapping the boundary to the unit disc and solving a Poisson boundary integral equation. The associated volumetric flow rate was evaluated numerically using an adaptive Simpson's rule and is therefore not included here. We now turn to the general solution.

Following Fullard and Wake [121], a solution to Eq. (4.8) subject to (4.9) is

$$w\,(\xi,\eta) = \frac{\sin\alpha\sin(\eta-\alpha)}{2\,(\cosh\xi - \cos\eta)} - \frac{\sin 2\alpha}{2\pi}\sum_{n=0}^{\infty}\frac{(-1)^n}{2n+1}\sin\left[A_n(\alpha+\pi-\eta)\right]F_n(\xi), \tag{4.26}$$

where

$$\begin{aligned} F_n\,(\xi) &= {}_2F_1\left(1, A_n; A_n+1; -\mathrm{e}^{-\xi}\right) + {}_2F_1\left(1, A_n; A_n+1; -\mathrm{e}^{\xi}\right) \\ &\quad - \frac{A_n}{A_n+1}\left[\mathrm{e}^{-\xi}\cdot{}_2F_1\left(1, A_n+1; A_n+2; -\mathrm{e}^{-\xi}\right) + \mathrm{e}^{\xi}\cdot{}_2F_1\left(1, A_n+1; A_n+2; -\mathrm{e}^{\xi}\right)\right], \end{aligned} \tag{4.27}$$

and

$$A_n = \frac{(2n+1)\,\pi}{2\alpha}. \tag{4.28}$$

In Eq. (4.27), ${}_2F_1(a,b;c;z)$ is the Gauss hypergeometric function [129]. We note that this analogy had already been employed by Irvine and Fullard in their study of slip-affected discharge in circular, lens, and figure-eight ducts [112]. Beyond the compact cases in Eqs. (4.14) ($\alpha = \pi/2$) and (4.19) ($\alpha = \pi/4$), we found no further closed forms for w from Eq. (4.26). We therefore derive an explicit double-series representation of the velocity field starting from Guo and Meroney's integral expression [120]. This addresses Fullard and Wake's observation that the Guo–Meroney form is not in closed form [121].

Guo and Meroney's integral representation [120] is

$$w(\xi,\eta) = \frac{\sin\alpha\,\sin(\eta-\alpha)}{2\,(\cosh\xi-\cos\eta)} - \frac{\sin 2\alpha}{2}\int_0^\infty \frac{\sinh\left[k(\pi+\alpha-\eta)\right]\cos k\xi}{\sinh k\pi\,\cosh(k\alpha)}\,\mathrm{d}k. \tag{4.29}$$

Using

$$\frac{1}{\sinh k\pi} = 2\sum_{n=1}^{\infty} \mathrm{e}^{-(2n-1)\pi k}, \tag{4.30}$$

$$\frac{1}{\cosh k\alpha} = 2\sum_{m=1}^{\infty} (-1)^{m-1}\,\mathrm{e}^{-(2m-1)\alpha k}, \tag{4.31}$$

and

$$\sinh[k(\pi+\alpha-\eta)] = \frac{1}{2}\left[\mathrm{e}^{k(\pi+\alpha-\eta)} - \mathrm{e}^{-k(\pi+\alpha-\eta)}\right], \tag{4.32}$$

and integrating termwise—termwise integration being justified by absolute convergence of the geometric expansions for $k > 0$—we obtain

$$w(\xi,\eta) = \frac{\sin\alpha\,\sin(\eta-\alpha)}{2\,(\cosh\xi-\cos\eta)} - \sin 2\alpha \sum_{m=1}^{\infty}\sum_{n=1}^{\infty}(-1)^{m-1}\left[\frac{B_{mn}(\eta)}{B_{mn}^2(\eta)+\xi^2} - \frac{C_{mn}(\eta)}{C_{mn}^2(\eta)+\xi^2}\right], \tag{4.33}$$

where

$$B_{mn}(\eta) = 2(n-1)\,\pi + 2(m-1)\,\alpha + \eta, \tag{4.34}$$

and

$$C_{mn}(\eta) = 2n\pi + 2m\alpha - \eta. \tag{4.35}$$

This yields an exact, integral-free double series for w, convenient for computation. We now turn to the volumetric flow rate.

Fullard and Wake [121] did not report the volumetric flow rate associated with Eq. (4.26). Although their velocity field is analytical, evaluating the volumetric flow rate directly from (4.13) is not straightforward. One may insert the double series in Eq. (4.33) into (4.13) and interchange summation and integration to obtain Q; a shorter and cleaner route is to recast Guo and Meroney's discharge integral for the fully filled, no-slip case [120]. In our variables it reads

$$Q(\alpha) = \frac{\csc^4\alpha}{4}\left[\left(\alpha - \sin 2\alpha + \frac{1}{4}\sin 4\alpha\right) + 2\pi\sin^2 2\alpha\int_0^\infty \frac{k\tanh k\alpha}{\sinh^2 k\pi}\,\mathrm{d}k\right]. \tag{4.36}$$

The improper integral (4.36) admits the series representation

$$\int_0^\infty \frac{k\tanh k\alpha}{\sinh^2 k\pi}\,\mathrm{d}k = \frac{1}{\alpha^2}\sum_{n=1}^{\infty} n\left[\psi_1\left(\frac{\pi n}{2\alpha}\right) - 2\,\psi_1\left(\frac{\pi n}{\alpha}\right) - \frac{\alpha^2}{\pi^2 n^2}\right], \tag{4.37}$$

where ψ_1 is the trigamma function [129]. Indeed, for $k > 0$ one can write

$$\frac{1}{\sinh^2 k\pi} = 4\sum_{n=1}^{\infty} n\, \mathrm{e}^{-2\pi n k} \tag{4.38}$$

and

$$\tanh k\alpha = 1 - 2\sum_{m=1}^{\infty} (-1)^{m-1}\, \mathrm{e}^{-2m\alpha k}. \tag{4.39}$$

Multiplying the series and integrating termwise yields

$$\int_0^{\infty} \frac{k\tanh k\alpha}{\sinh^2 k\pi}\,\mathrm{d}k = \sum_{n=1}^{\infty} n\left[\frac{1}{\pi^2 n^2} - 2\sum_{m=1}^{\infty} \frac{(-1)^{m-1}}{(\pi n + m\alpha)^2}\right]. \tag{4.40}$$

At this point, standard duplication/shift identities for the trigamma function [129] reduce the alternating inner sum to a linear combination of ψ_1 evaluated at $\pi n/(2\alpha)$ and $\pi n/\alpha$, which, after a short simplification, gives exactly (4.37). Despite appearances, the series converges: the bracketed term is $O(n^{-3})$ as $n \to \infty$, hence the summand is $O(n^{-2})$.

As a result, the Poiseuille number in (4.10) admits the explicit analytical form

$$Po\,(\alpha) = \frac{(2\alpha - \sin 2\alpha)^3}{2\,\alpha^2 \sin^4\alpha\, Q\,(\alpha)}, \tag{4.41}$$

where

$$Q\,(\alpha) = \frac{\csc^4\alpha}{4}\left\{\left(\alpha - \sin 2\alpha + \frac{1}{4}\sin 4\alpha\right) + \frac{2\pi\sin^2 2\alpha}{\alpha^2}\sum_{n=1}^{\infty} n\left[\psi_1\left(\frac{\pi n}{2\alpha}\right) - 2\,\psi_1\left(\frac{\pi n}{\alpha}\right) - \frac{\alpha^2}{\pi^2 n^2}\right]\right\}. \tag{4.42}$$

With this analytical backbone, several rational angles admit closed forms for the discharge; consequently $Q(\alpha)$ and $Po(\alpha)$ do as well. For example,

$$\begin{aligned}
Q\left(\frac{\pi}{8}\right) &= \frac{\pi}{2}\left(8 + 5\sqrt{2}\right) - \frac{21}{2} - 8\sqrt{2} - \frac{1}{\pi}\left(3 + 2\sqrt{2}\right),\\
Q\left(\frac{\pi}{6}\right) &= \frac{107\,\pi}{36} - \frac{29\sqrt{3}}{6} - \frac{3}{\pi},\\
Q\left(\frac{\pi}{4}\right) &= \frac{3\pi}{4} - 2 - \frac{1}{\pi},\\
Q\left(\frac{\pi}{3}\right) &= \frac{11\pi}{36} - \frac{\sqrt{3}}{2},\\
Q\left(\frac{2\pi}{3}\right) &= \frac{17\pi}{72} + \frac{\sqrt{3}}{2},\\
Q\left(\frac{3\pi}{4}\right) &= \frac{217\pi}{324} + 2 - \frac{1}{3\pi},\\
Q\left(\frac{5\pi}{6}\right) &= \frac{271\pi}{36} - \frac{53\sqrt{3}}{6} - \frac{3}{\pi} + \frac{24V}{\pi},
\end{aligned} \tag{4.43}$$

where V is the Gieseking constant [130]. These closed forms follow by specialising α to rational fractions of π, regrouping the trigamma series into finitely many congruence classes, and then applying standard reduction formulae for ψ_1 so that the infinite sum collapses to a finite trigonometric combination; routine simplifications yield expressions in radicals and π (with the Gieseking constant V arising naturally at $\alpha = 5\pi/6$). Symbolic steps were carried out in Maple 2025.1 [131] and Wolfram Mathematica 14.3 [132]; high-precision checks used Python 3.14.0 with `mpmath` 1.3.0 [133, 134], agreeing with (4.36) to all reported digits.

The corresponding Poiseuille numbers are

$$
\begin{aligned}
Po\left(\frac{\pi}{8}\right) &= \frac{8(\pi - 2\sqrt{2})^3}{\pi\left[4\pi^2 + \pi - 2 - \sqrt{2}\,(\pi^2 + 6\pi)\right]} \approx 15.691, \\
Po\left(\frac{\pi}{6}\right) &= \frac{48\,(2\pi - 3\sqrt{3})^3}{\pi\left(107\pi^2 - 174\sqrt{3}\,\pi - 108\right)} \approx 15.771, \\
Po\left(\frac{\pi}{4}\right) &= \frac{16\,(\pi - 2)^3}{\pi\,(3\pi^2 - 8\pi - 4)} \approx 15.916, \\
Po\left(\frac{\pi}{3}\right) &= \frac{4\,(4\pi - 3\sqrt{3})^3}{3\pi^2\left(11\pi - 18\sqrt{3}\right)} \approx 15.999, \\
Po\left(\frac{2\pi}{3}\right) &= \frac{2\,(8\pi + 3\sqrt{3})^3}{3\pi^2\left(17\pi + 36\sqrt{3}\right)} \approx 16.279, \\
Po\left(\frac{3\pi}{4}\right) &= \frac{144\,(3\pi + 2)^3}{\pi\,(217\pi^2 + 648\pi - 108)} \approx 16.797, \\
Po\left(\frac{5\pi}{6}\right) &= \frac{48\,(10\pi + 3\sqrt{3})^3}{25\pi\left[864\,V - \pi\,\left(318\sqrt{3} - 271\pi\right) - 108\right]} \approx 17.507.
\end{aligned}
\tag{4.44}
$$

To the best of our knowledge, these closed-form evaluations of $Po(\alpha)$ at the listed angles have not been recorded previously.

Expansions about the endpoints and the circular case are

$$
Po(\alpha) \sim \begin{cases} \dfrac{140}{9} + \dfrac{28}{27}\,\varepsilon^2 + O\left(\varepsilon^4\right) & \alpha = \varepsilon \approx 0, \\[2ex] 16 + 32\left(\dfrac{10}{\pi^2} - 1\right)\varepsilon^2 + O\left(\varepsilon^4\right) & \alpha = \dfrac{\pi}{2} + \varepsilon \approx \dfrac{\pi}{2}, \\[2ex] 16 + \dfrac{32}{\pi}\,\varepsilon + O\left(\varepsilon^3\right) & \alpha = \pi - \varepsilon \approx \pi. \end{cases}
\tag{4.45}
$$

In particular, the endpoint values follow directly from (4.45): $Po(0) = 140/9$ and $Po(\pi) = 16$. The coefficients in (4.45) follow by Taylor expanding the elementary prefactors in $Q(\alpha)$ and using the large–argument expansion of the trigamma function in the series form of (4.36). Analogous expansions about other rational angles can be generated in the same way (by differentiating the corresponding closed forms for Q), but for brevity we restrict attention to

the endpoint and near-circular limits; the $\alpha \to 0$ and $\alpha \to \frac{\pi}{2}$ cases are consistent with Wang's results expressed in terms of the thickness ratio b [3], and we include the $\alpha \to \pi$ figure-eight endpoint here for completeness.

4.4 Results

In the lens-shaped domain, the case $\alpha = \frac{\pi}{3}$ corresponds to the classical *vesica piscis*, formed by the intersection of two circles of equal radius. Figure 4.2 shows the isovelocity contours for this configuration. The curves are nearly circular near the geometric centre, where the axial velocity attains its maximum, and they gradually stretch into lens-like shapes as they approach the boundary.

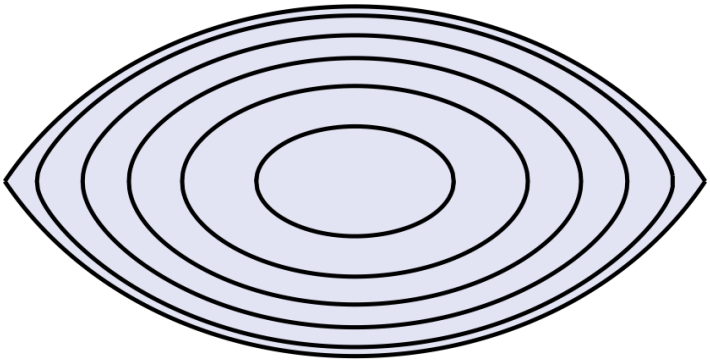

Figure 4.2: Isovelocity curves for $\alpha = \pi/3$, with normalised levels 0.1, 0.3, ..., 0.9 plotted from the outer to the inner curve.

For $\frac{\pi}{2} < \alpha < \pi$ the cross-section becomes a figure-eight. Figure 4.3 displays isovelocity contours for $\alpha = 2\pi/3$ (a) and $\alpha = 5\pi/6$ (b). Unlike circular, elliptical, or rectangular ducts, where the maximum velocity occurs at the geometric centre, figure-eight sections exhibit different behaviour: for $\alpha \gtrsim 0.76\pi$ the maximum shifts away from the waist towards the centres of the lobes, an effect analogous to the velocity dip [121]. This phenomenon is well documented in the literature [121, 112, 135, 136], so we do not examine it further here.

To our knowledge, this appears to be the first report of the Poiseuille number *Po* across the complete lens–figure-eight family. Wang [3] treated only the lens regime, parameterising the geometry by $b \in [0, 1]$, which corresponds to $\alpha \in [0, \pi/2]$. The Ritz method adopted there yields approximate values that depend on basis choice and truncation, and the tabulated results were given to two decimal places; moreover, Wang explicitly notes that the Ritz method performs poorly near the circular limit ($b \approx 1$) and also suffers convergence difficulties for very thin cross-sections ($b \approx 0$), for which perturbation methods were used [3]. By contrast, the present work derives an explicit analytical expression for the discharge and provides $Po(\alpha)$ over the whole interval $\alpha \in (0, \pi)$. Table 4.1 compares the present analytical values with those of [3] over the lens range and illustrates both the limitations of the Ritz method and the accuracy achieved here. The present treatment covers the full domain,

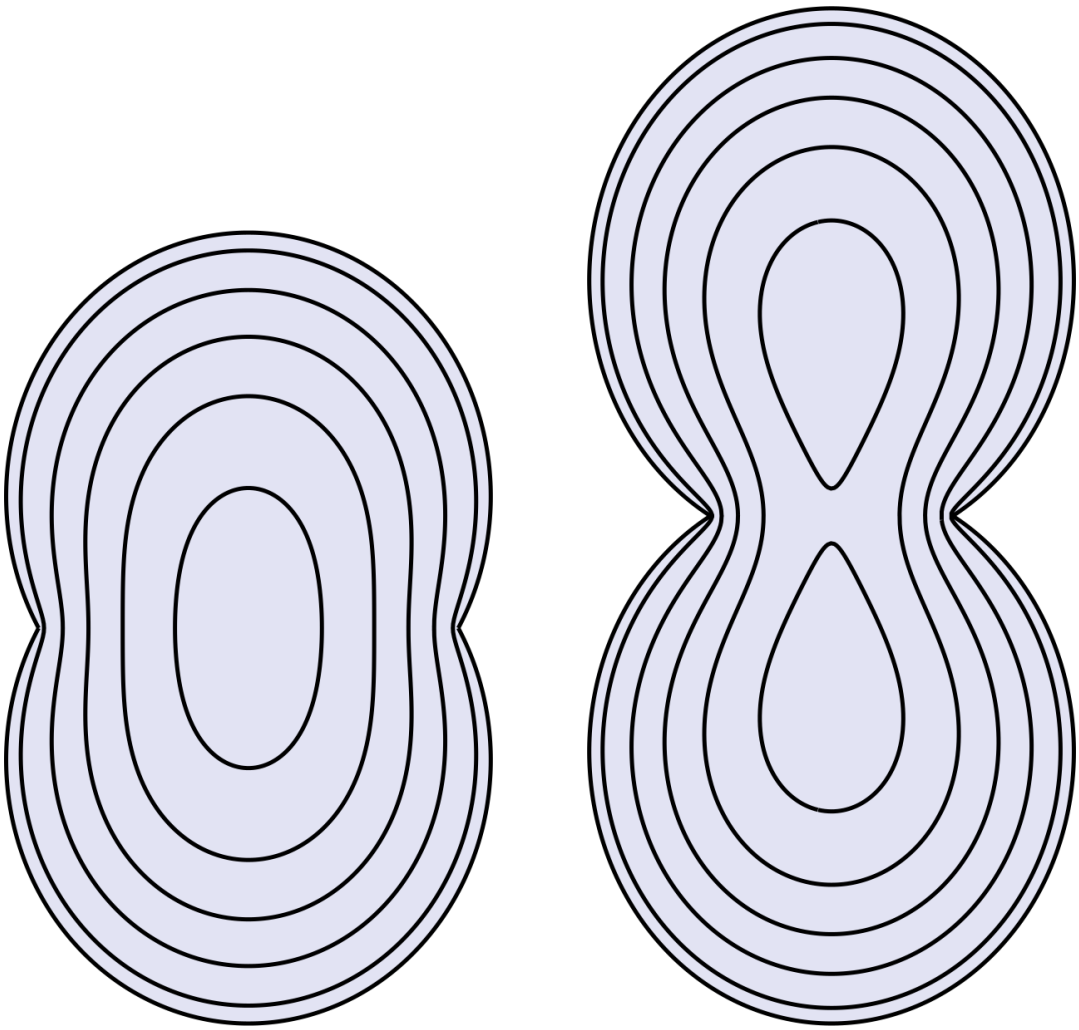

(a) (b)

Figure 4.3: Isovelocity curves for $\alpha = 2\pi/3$ (a) and $\alpha = 5\pi/6$ (b), with normalised levels 0.1, 0.3, …, 0.9 plotted from the outer to the inner curve.

and the results are mutually consistent. In addition, three asymptotic regimes are identified for this geometry, each in agreement with the general solution within its respective range of validity. In the present case the validity range is particularly broad, and perturbation methods yield an excellent approximation, as shown in Figure 4.4. Over $(0, \pi)$, $Po(\alpha)$ attains a unique global maximum at $\alpha \approx 0.89\pi$, where $Po(\alpha) \approx 17.76$; this does not coincide with the threshold at which the location of the maximum axial velocity splits from a single peak at the waist to two symmetric off-waist peaks. To provide a complete overview, Table 4.2 reports Po (to three decimal places) as a function of the angle α. For independent verification, the Poisson problem defined by Eqs. (4.1) and (4.2) was also solved in Cartesian coordinates using the finite element method (FEM) in FreeFEM++ [137]. Exploiting symmetry, computations were performed on one quarter of the cross-section with homogeneous Neumann conditions along the symmetry lines. Meshes were generated automatically by the Delaunay–Voronoi algorithm, and the domain was discretised with quadratic (P_2) triangular elements. The volumetric flow rate was evaluated by Gaussian quadrature via the `int2d` operator in FreeFEM++. The FEM results agree with the analytical values to all reported

digits.

Table 4.1: Poiseuille number Po as a function of b. Each entry shows our analytical value followed by Wang (2008) in parentheses.

b	Po
0	15.56 (15.56)
0.1	15.59 (15.60)
0.2	15.69 (15.69)
0.3	15.81 (15.80)
0.4	15.90 (15.90)
0.5	15.97 (15.98)
0.6	16.00 (16.00)
0.7	16.01 (16.03)
0.8	16.01 (16.03)
0.9	16.00 (16.01)
1	16.00 (16.00)

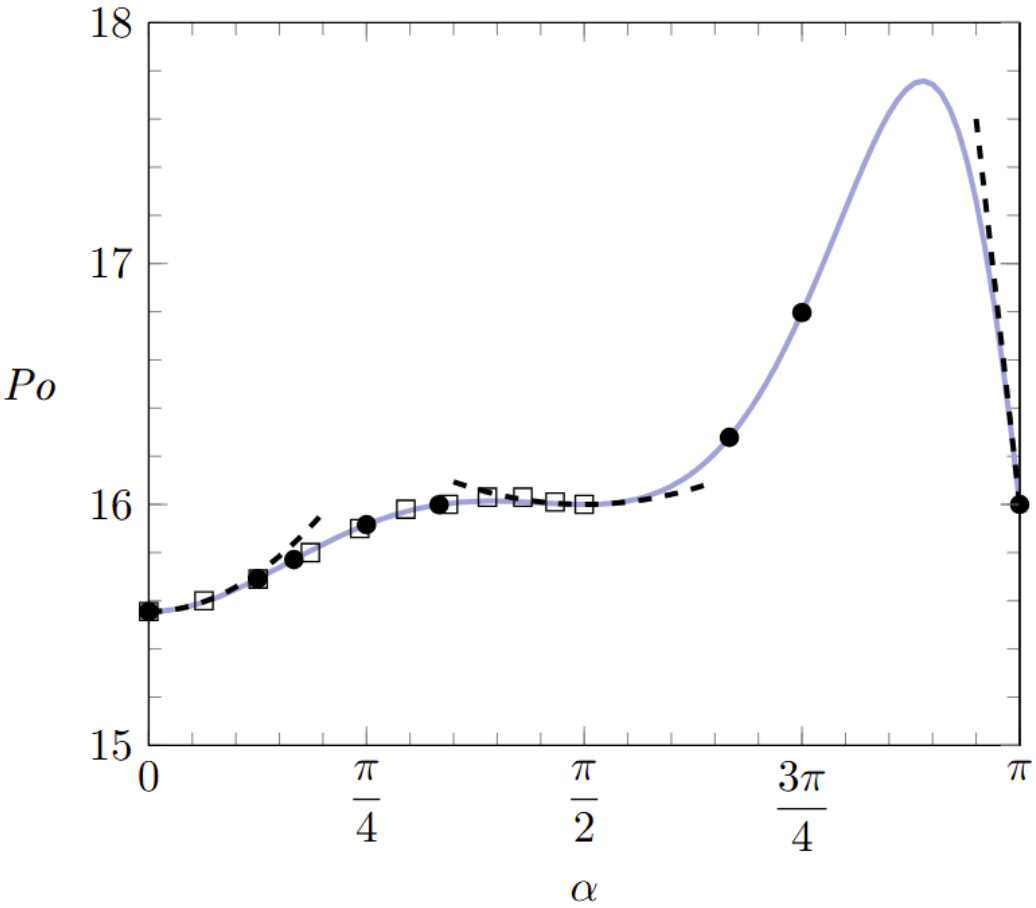

Figure 4.4: Poiseuille number Po as a function of α. The solid line is the analytical solution given by Eq. (4.41); the dashed line shows the perturbation solutions of Eq. (4.45). Squares denote Wang's Ritz-method results [3], and circles mark the closed-form evaluations from Eqs. (4.18), (4.25), and (4.44).

To obtain a domain-wide approximation, the traditional approach of fitting a single fifth-degree polynomial over the full interval [114, 80, 37] performs poorly for this curve and

Table 4.2: Poiseuille number *Po* as a function of α.

α	*Po*
0°	15.556
10°	15.586
20°	15.666
30°	15.771
40°	15.873
50°	15.952
60°	15.999
70°	16.014
80°	16.008
90°	16.000
100°	16.019
110°	16.099
120°	16.279
130°	16.590
140°	17.030
150°	17.507
160°	17.758
170°	17.352
180°	16.000

yields a much larger maximum error. We therefore use a Padé approximant [138] that is uniform on $0 \le \alpha \le \pi$, simple to evaluate, and consistent with the endpoint limits; in particular, it is exact at $\alpha = 0$. The $6/6$ form is

$$Po(\alpha) \approx \frac{140}{9} \frac{1 + \sum_{n=1}^{6} a_n \alpha^n}{1 + \sum_{n=1}^{6} b_n \alpha^n}, \tag{4.46}$$

where

$$\begin{aligned} a_1 &= -\frac{39100}{43459}, \quad a_2 = \frac{89051}{82273}, \quad a_3 = -\frac{27405}{33121}, \\ a_4 &= \frac{32765}{98949}, \quad a_5 = -\frac{3617}{53382}, \quad a_6 = \frac{257}{44277}, \end{aligned} \tag{4.47}$$

and

$$\begin{aligned} b_1 &= -\frac{56156}{62427}, \quad b_2 = \frac{95167}{93907}, \quad b_3 = -\frac{30911}{40904}, \\ b_4 &= \frac{9187}{29274}, \quad b_5 = -\frac{7122}{99331}, \quad b_6 = \frac{653}{90719}. \end{aligned} \tag{4.48}$$

This rational approximation has a maximum relative error of about 0.012%.

4.5 Conclusions

We revisit steady, fully developed Poiseuille flow in lens-shaped and figure-eight ducts. Building on an integral representation adapted from Guo and Meroney [120], we derive an explicit analytical expression for the volumetric flow rate $Q(\alpha)$ and, from it, the corresponding Poiseuille number $Po(\alpha)$. The formulation recovers the classical circular and right-angle lens benchmarks and extends prior lens-only treatments to the full lens–figure-eight family. Several closed-form evaluations at special angles were identified; these provide stringent benchmarks for analysis and numerical verification. An equivalent, rapidly convergent series in terms of the trigamma function was also recorded, which is convenient for computation.

Asymptotic expansions were obtained in three regimes—thin lens, near circular, and strongly constricted figure-eight—and were consistent with the general solution within their ranges of validity. For practical use, a compact $6/6$ Padé approximant for $Po(\alpha)$ was constructed; it is exact at $\alpha = 0$ and exhibits a maximum relative error of about 0.012%. The closed forms and the Padé approximant together provide ready-to-use references for design calculations and for code verification in noncircular, multi-lobed passages.

By direct analogy with the partially filled circular-pipe problem, the corresponding discharge–depth relations follow within the same framework; we simply note this connection here and refer to Ref. [112] for context.

Chapter 5

Startup of Poiseuille flow in triangular ducts

This chapter is a reproduction of the following publication:

Silva, V. C.; Lustosa, B. P.; Lopes, A.B. Startup of Poiseuille flow in triangular ducts. Zeitschrift für Angewandte Mathematik und Physik (ZAMP), Vol. 76, No. 6, Article 241, 2025.

5.1 Introduction

Although rare, exact solutions to the Navier–Stokes equations play a fundamental role in fluid mechanics, serving both as theoretical benchmarks and as tools for validating numerical methods [139, 140, 34].

Among classical flows, Poiseuille flow, defined as pressure-driven motion through an infinitely long duct of constant cross-section, is one of the most thoroughly studied. In the steady-state regime, numerous analytical solutions have been compiled, notably by Shah and London [33], the principal reference on fully developed duct flows. See also the works of Jog [141] and Berker [142]. Steady-state solutions continue to be an active subject of research, with new results regularly reported [79, 143, 144, 88].

In contrast, exact analytical solutions for the startup of Poiseuille flows remain remarkably scarce. Table 5.1 summarizes studies on the startup of Poiseuille flow in ducts reported in the literature.

In this work, we derive new exact solutions for the startup of Poiseuille flow in ducts with triangular cross-sections. In the steady-state regime, exact analytical solutions are known for three domains: the equilateral triangle, the hemi-equilateral triangle (30°–60°–90°), and the right-angled isosceles triangle (45°–45°–90°). However, among these, only the equilateral case has had its counterpart in startup of Poiseuille flow previously reported [154]. Here, we

Table 5.1: Studies in startup of Poiseuille flow in ducts.

Geometry	Method	Reference	Year
Circular duct	Separation of variables	Ref. [145]	1932
Annular sector duct	Separation of variables	Ref. [146]	1936
Rectangular duct	Separation of variables	Ref. [147]	2003
Semi-circular duct	Separation of variables	Ref. [148]	2005
Circular sector duct	Separation of variables	Ref. [149]	2011
Equilateral triangular duct	Eigenfunction superposition	Ref. [150]	2016
Regular polygonal duct	Eigenfunction superposition	Ref. [151]	2016
Elliptical duct	Eigenfunction superposition	Ref. [152]	2018
Stadium-shaped duct	Eigenfunction superposition	Ref. [153]	2020

address the startup problem for the two remaining configurations.

Triangular and other non-circular ducts arise in various engineering fields, including aerospace, nuclear, chemical, biomedical, and electronics sectors [155, 156]. Non-circular microchannels have also been employed in microfluidic devices, compact heat exchangers, and lab-on-a-chip systems such as DNA extraction, biosensors, blood sampling, and glucose monitoring [157, 158].

Sec. 5.2 presents the formulation of the startup problem. Sec. 5.3 outlines the general solution via eigenfunction superposition method. Applications to hemi-equilateral and right-angled isosceles triangular ducts are discussed in Sec. 5.4, followed by concluding remarks in Sec. 5.5.

5.2 Formulation

We consider the startup flow of an incompressible Newtonian fluid of viscosity μ and density ρ in a straight duct of uniform cross-section Γ. The fluid, initially at rest, is set into motion by the sudden application of a constant axial pressure gradient of magnitude $-G$, corresponding to a startup of Poiseuille flow. Assuming the motion remains unidirectional, the axial component of the Navier–Stokes equations reduces to a heat equation with a source term for the axial velocity. Introducing a characteristic length scale L, we scale velocities by GL^2/μ and time by $\rho L^2/\mu$, so that the governing equation becomes

$$\frac{\partial w}{\partial t} = \nabla^2 w + H(t), \tag{5.1}$$

where $w(x, y, t)$ is the axial velocity and $H(t)$ is the Heaviside step function. The boundary condition is $w = 0$ on $\partial\Gamma$, and the initial condition is $w = 0$ at $t = 0$.

5.3 Solution

The Laplace transform of Eq. (5.1) with respect to time yields

$$s\,\overline{w} = \nabla^2\overline{w} + \frac{1}{s}, \tag{5.2}$$

where $\overline{w}(x, y, s)$ denotes the Laplace transform of $w(x, y, t)$, and $s > 0$. The solution is written as

$$\overline{w} = \sum_j \overline{W}_j\,\phi_j, \tag{5.3}$$

where $\overline{W}_j(s)$ are unknown coefficients and $\phi_j(x, y)$ are eigenfunctions of the Laplacian satisfying

$$\nabla^2\phi_j + \lambda_j\phi_j = 0, \qquad \phi_j = 0 \quad \text{on } \partial\Gamma, \tag{5.4}$$

with eigenvalues λ_j ordered increasingly. It can be shown that the corresponding eigenfunctions are mutually orthogonal and form a complete orthogonal set [159].

Substitution into Eq. (5.2), followed by projection and use of orthogonality, gives

$$\overline{W}_j = \frac{\alpha_j}{\beta_j s\,(s + \lambda_j)}, \tag{5.5}$$

where

$$\alpha_j = \iint_\Gamma \phi_j\,\mathrm{d}x\,\mathrm{d}y, \qquad \beta_j = \iint_\Gamma \phi_j^2\,\mathrm{d}x\,\mathrm{d}y. \tag{5.6}$$

Inverting the transform term by term yields the solution

$$w = \sum_j \frac{\alpha_j}{\beta_j\lambda_j}\phi_j\left(1 - \mathrm{e}^{-\lambda_j t}\right). \tag{5.7}$$

The flow rate is then

$$Q = \iint_\Gamma w\,\mathrm{d}x\,\mathrm{d}y = \sum_j \frac{\alpha_j^2}{\beta_j\lambda_j}\left(1 - \mathrm{e}^{-\lambda_j t}\right), \tag{5.8}$$

and its steady limit as $t \to \infty$ is

$$Q_\infty = \sum_j \frac{\alpha_j^2}{\beta_j\lambda_j}. \tag{5.9}$$

A mathematically equivalent formulation, which avoids the use of Laplace transforms, was proposed by Wang [151] in his analysis of the startup of Poiseuille flow in regular polygonal ducts.

The Poiseuille number is

$$Po = \frac{8A^3}{P^2 Q_\infty}, \tag{5.10}$$

where A and P denote the cross-sectional area and wetted perimeter of the duct.

Scaled by $G\,L$, the mean shear stress is given by

$$\bar{\tau} = \frac{1}{P}\oint_{\partial\Gamma} \tau_{\mathrm{w}}\,\mathrm{d}s = -\frac{1}{P}\oint_{\partial\Gamma} \left(\tau_{xz}\,n_x + \tau_{yz}\,n_y\right)\,\mathrm{d}s, \tag{5.11}$$

where τ_w is the wall shear stress, $\mathbf{n} = (n_x, n_y)$ is the outward unit normal to $\partial\Gamma$, and

$$\tau_{xz} = \frac{\partial w}{\partial x} = \sum_j \frac{\alpha_j}{\beta_j\lambda_j}\frac{\partial \phi_j}{\partial x}\left(1 - \mathrm{e}^{-\lambda_j t}\right) \tag{5.12}$$

and

$$\tau_{yz} = \frac{\partial w}{\partial y} = \sum_j \frac{\alpha_j}{\beta_j\lambda_j}\frac{\partial \phi_j}{\partial y}\left(1 - \mathrm{e}^{-\lambda_j t}\right) \tag{5.13}$$

are the only nonzero shear-stress components.

5.4 Results

The approach presented in Sec. 5.3, based on the eigenfunction superposition method, is a powerful technique widely used to solve problems governed by Laplace-type operators. Its main limitation lies in the requirement of a complete set of eigenfunctions and eigenvalues for the associated Helmholtz problem, which is only available for a limited class of domains, including rectangles, circular and annular regions, and three triangular cross-sections: the hemi-equilateral triangle (30°–60°–90°), the right-angled isosceles triangle (45°–45°–90°), and the equilateral triangle (60°–60°–60°) [160].

We now present exact analytical solutions for the startup of Poiseuille flow in two right triangular ducts: the hemi-equilateral and the right-angled isosceles triangles. These domains are among the few for which the Laplace operator admits a complete set of trigonometric eigenfunctions under homogeneous Dirichlet conditions [161]. The equilateral case, not considered here, was treated by Wang [151].

5.4.1 Hemi-equilateral triangular duct

Consider the domain $\Gamma = \{(x, y) \in \mathbb{R}^2 : 0 < x < 1,\ 0 < y < x/\sqrt{3}\}$, which defines a hemi-equilateral triangular cross-section (Fig. 5.1).

The eigenfunctions of the Laplacian in this domain satisfy Eq. (5.4) and are indexed by pairs of positive integers $m, n \in \mathbb{Z}^+$. They are given by [162, 163]

$$\phi_{mn} = \sin(m\pi x)\sin\left[\frac{(3m+2n)\pi y}{\sqrt{3}}\right] + \sin[(2m+n)\pi x]\sin\left(\frac{n\pi y}{\sqrt{3}}\right) - \sin[(m+n)\pi x]\sin\left[\frac{(3m+n)\pi y}{\sqrt{3}}\right], \tag{5.14}$$

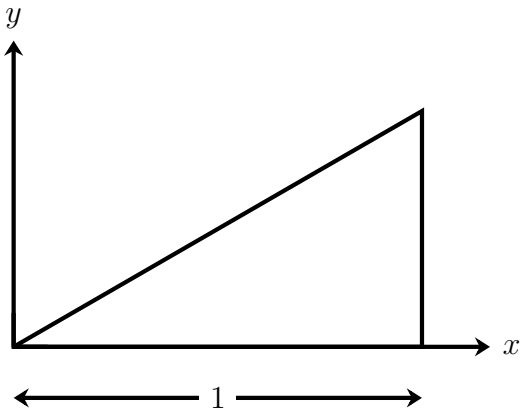

Figure 5.1: Hemi-equilateral triangular duct.

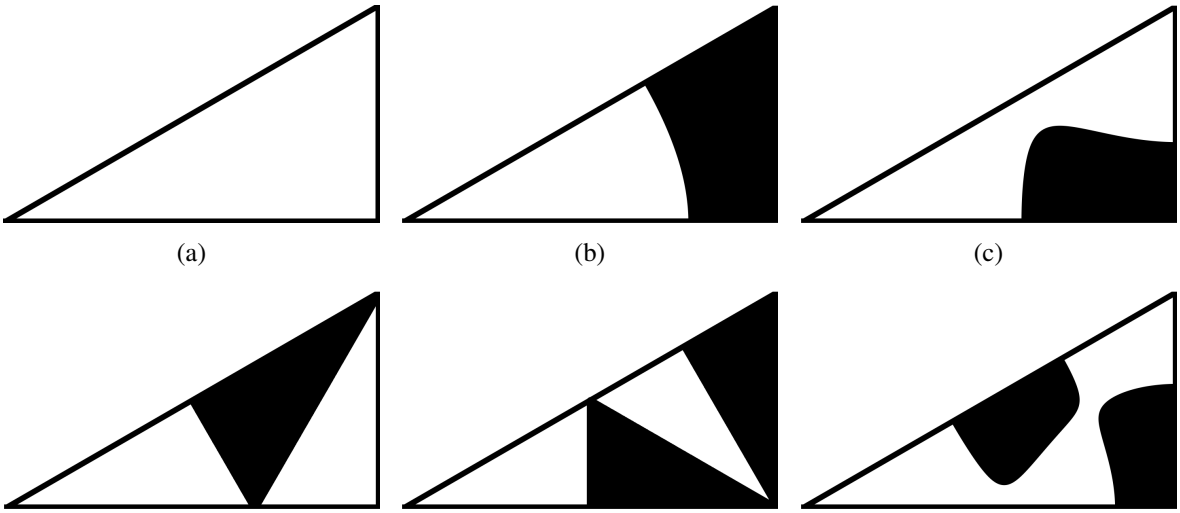

Figure 5.2: Dirichlet eigenfunction nodal domains for the hemi-equilateral triangle: (a) λ_{11}, (b) λ_{12} (c) λ_{21}, (d) λ_{13}, (e) λ_{22} and (f) λ_{14}.

with corresponding eigenvalues

$$\lambda_{mn} = \frac{4\pi^2}{3}(3m^2 + 3mn + n^2). \tag{5.15}$$

The first six eigenvalues, $\lambda_{11} \approx 92.1163$, $\lambda_{12} \approx 171.0731$, $\lambda_{21} \approx 250.0300$, $\lambda_{13} \approx 276.3489$, $\lambda_{22} \approx 368.4652$, and $\lambda_{14} \approx 407.9436$, correspond to the eigenfunctions whose nodal domains are shown in Fig. 5.2.

Eqs. (5.6) and (5.14) give

$$\alpha_{mn} = \frac{\sqrt{3}}{\pi^2}\left[\frac{1-(-1)^m}{m(3m+2n)} + \frac{1-(-1)^n}{n(2m+n)} - \frac{1-(-1)^{m+n}}{(m+n)(3m+n)}\right], \qquad \beta_{mn} = \frac{\sqrt{3}}{8}. \tag{5.16}$$

Substituting into Eq. (5.7), the velocity field becomes

$$w = \sum_{m=1}^{\infty}\sum_{n=1}^{\infty} \frac{8}{\lambda_{mn}\pi^2}\left[\frac{1-(-1)^m}{m(3m+2n)} + \frac{1-(-1)^n}{n(2m+n)} - \frac{1-(-1)^{m+n}}{(m+n)(3m+n)}\right]\phi_{mn}\left(1-\mathrm{e}^{-\lambda_{mn}t}\right). \tag{5.17}$$

The flow rate, from Eqs. (5.8) and (5.16), is

$$Q = \sum_{m=1}^{\infty}\sum_{n=1}^{\infty} \frac{8\sqrt{3}}{\lambda_{mn}\pi^4}\left[\frac{1-(-1)^m}{m(3m+2n)} + \frac{1-(-1)^n}{n(2m+n)} - \frac{1-(-1)^{m+n}}{(m+n)(3m+n)}\right]^2\left(1-\mathrm{e}^{-\lambda_{mn}t}\right), \tag{5.18}$$

which tends to

$$Q_\infty \approx 1.9785 \times 10^{-3}. \tag{5.19}$$

Fig. 5.3 shows the velocity field computed from Eq. (5.17).

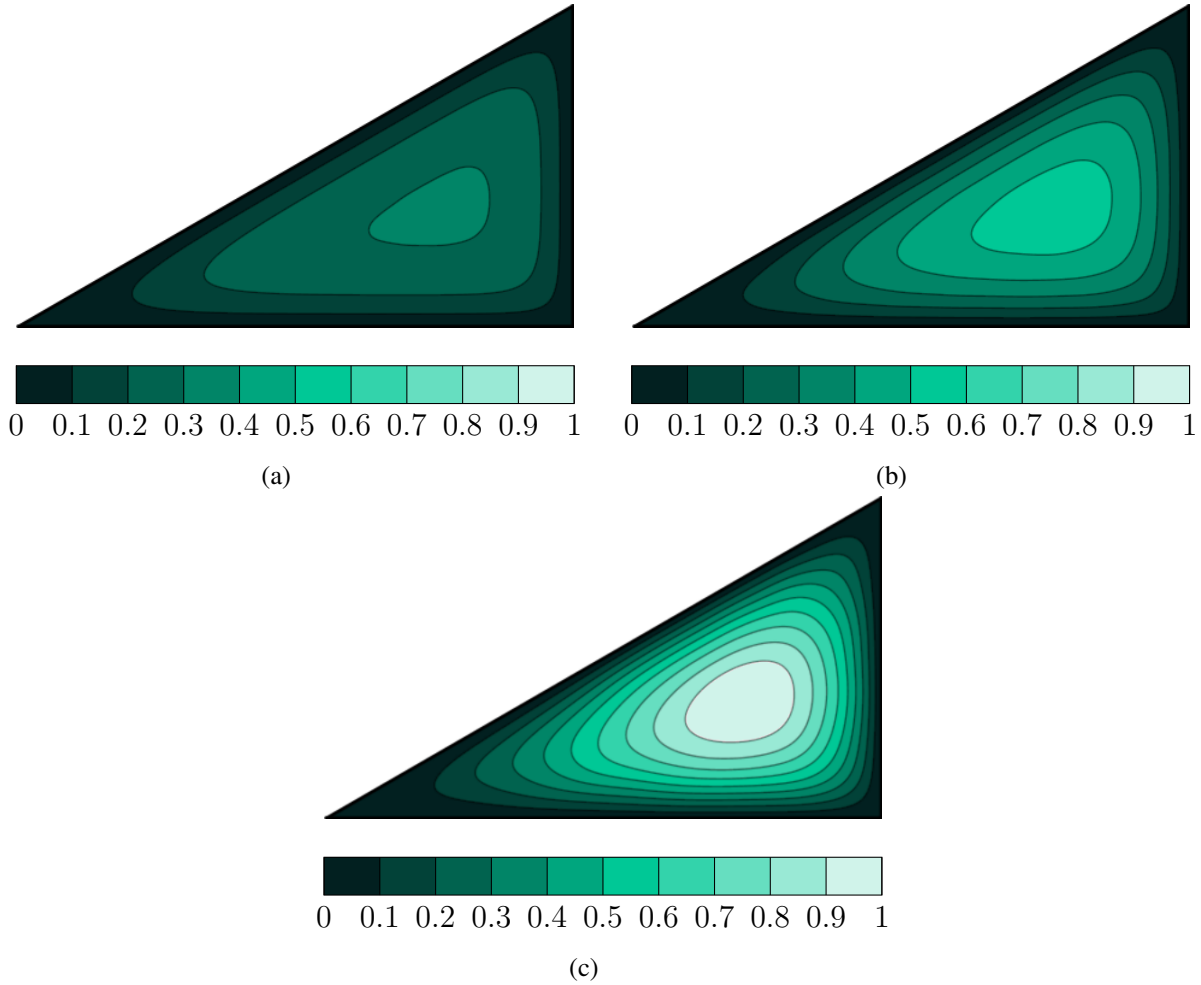

Figure 5.3: Velocity field in the hemi-equilateral triangular duct: (a) $t = 0.005$, (b) $t = 0.01$, and (c) $t = 0.1$. The colour scale is normalized by the steady-state maximum velocity, $w_{\max} \approx 0.0157$.

Substituting the cross-sectional area $A = \sqrt{3}/6$ and perimeter $P = 1 + \sqrt{3}$ into Eq. (5.10) gives

$$Po \approx 13.0317. \tag{5.20}$$

The steady solution for Poiseuille flow in the hemi-equilateral triangular duct may be obtained by analogy with two classical problems of identical mathematical form. Seth [164] employed conformal mapping to compute the velocity field in a rotating cylinder with a $30°$–$60°$–$90°$ triangular cross-section, while Hay [165] applied the method of images to determine the torsional stress in a beam with the same geometry. For the sake of comparison, we adopt the latter, as it yields a direct expression for the quantities of interest.

By identifying Hay's Prandtl stress function with the velocity field, the solution reads

$$w_\infty = \frac{(x-1)(-x^2-x+3y^2)}{6} - \sum_{n=1}^{\infty} \frac{2}{n^3\pi^3}\,\chi_n(x,y), \tag{5.21}$$

where

$$\chi_{2n-1} = \frac{\sin[(2n-1)\pi x]\left\{\sqrt{3}(-1)^{n+1}\sinh[(2n-1)\pi y] + \cosh\left[(2n-1)\pi(-2y+\sqrt{3})/2\right]\right\}}{\cosh[3(2n-1)\xi]}, \tag{5.22}$$

$$\chi_{2n} = -\frac{\sin(2n\pi x)\left[(-1)^n\cosh(2n\pi y) + \cosh\left[n\pi(-2y-\sqrt{3})\right]\right]}{(-1)^n + \cosh(6n\xi)}, \tag{5.23}$$

and

$$\xi = \frac{\pi}{2\sqrt{3}}. \tag{5.24}$$

A corresponding expression for the flow rate is obtained by identifying Hay's torsional rigidity with the volumetric flow rate:

$$Q_\infty = \frac{7\sqrt{3}}{1080} + \frac{1}{2\pi^5}\left[3\left(H_1+H_2+H_3+H_4+\sqrt{3}H_5\right) + 5\left(H_6+\sqrt{3}H_7\right)\right], \tag{5.25}$$

with

$$H_1 = \sum_{n=1}^{\infty} \frac{1}{(2n)^5}\frac{\sinh(2n\xi)}{(-1)^n+\cosh(6n\xi)}, \quad H_2 = \sum_{n=1}^{\infty} \frac{(-1)^{n+1}}{(2n)^5}\frac{\sinh(4n\xi)}{(-1)^n+\cosh(6n\xi)}, \tag{5.26}$$

$$H_3 = -\sum_{n=1}^{\infty} \frac{1}{(2n)^5}\frac{\sinh(6n\xi)}{(-1)^n+\cosh(6n\xi)}, \quad H_4 = \sum_{n=1}^{\infty} \frac{1}{(2n-1)^5}\frac{\sinh[(2n-1)\xi]}{\cosh[3(2n-1)\xi]}, \tag{5.27}$$

$$H_5 = \sum_{n=1}^{\infty} \frac{(-1)^n}{(2n-1)^5}\frac{\cosh[2(2n-1)\xi]}{\cosh[3(2n-1)\xi]}, \quad H_6 = -\sum_{n=1}^{\infty} \frac{1}{(2n-1)^5}\frac{\sinh[3(2n-1)\xi]}{\cosh[3(2n-1)\xi]}, \tag{5.28}$$

$$H_7 = \sum_{n=1}^{\infty} \frac{(-1)^{n+1}}{(2n-1)^5}\frac{1}{\cosh[3(2n-1)\xi]}. \tag{5.29}$$

Numerical evaluation of Eq. (5.25) agrees with the result obtained from the eigenfunction superposition method in Eq. (5.19).

On the horizontal segment $(0 \le x \le 1,\ y = 0)$, the shear stress is

$$\tau_{\mathrm{w},1} = \tau_{yz}(x,0) = \sum_{m=1}^{\infty}\sum_{n=1}^{\infty} \frac{\alpha_{mn}}{\beta_{mn}\,\lambda_{mn}} \frac{\partial \phi_{mn}}{\partial y}(x,0)\left(1 - \mathrm{e}^{-\lambda_{mn} t}\right). \tag{5.30}$$

On the vertical segment $\left(x = 1,\ 0 \le y \le 1/\sqrt{3}\right)$, the shear stress is

$$\tau_{\mathrm{w},2} = -\tau_{xz}(1,y) = -\sum_{m=1}^{\infty}\sum_{n=1}^{\infty} \frac{\alpha_{mn}}{\beta_{mn}\,\lambda_{mn}} \frac{\partial \phi_{mn}}{\partial x}(1,y)\left(1 - \mathrm{e}^{-\lambda_{mn} t}\right). \tag{5.31}$$

On the inclined segment $\left(0 \le x \le 1,\ y = x/\sqrt{3}\right)$, the shear stress is

$$\begin{aligned} \tau_{\mathrm{w},3} &= \frac{1}{2}\,\tau_{xz}\left(x, \frac{x}{\sqrt{3}}\right) - \frac{\sqrt{3}}{2}\,\tau_{yz}\left(x, \frac{x}{\sqrt{3}}\right) \\ &= \frac{1}{2}\sum_{m=1}^{\infty}\sum_{n=1}^{\infty} \frac{\alpha_{mn}}{\beta_{mn}\,\lambda_{mn}} \left[\frac{\partial \phi_{mn}}{\partial x}\left(x, \frac{x}{\sqrt{3}}\right) - \sqrt{3}\,\frac{\partial \phi_{mn}}{\partial y}\left(x, \frac{x}{\sqrt{3}}\right)\right]\left(1 - \mathrm{e}^{-\lambda_{mn} t}\right). \end{aligned} \tag{5.32}$$

From Eq. (5.11), one obtains

$$\bar{\tau} = \frac{1}{1+\sqrt{3}}\left[\int_0^1 \tau_{\mathrm{w},1}\,\mathrm{d}x + \int_0^{1/\sqrt{3}} \tau_{\mathrm{w},2}\,\mathrm{d}y + \frac{2}{\sqrt{3}}\int_0^1 \tau_{\mathrm{w},3}\,\mathrm{d}x\right]. \tag{5.33}$$

Each of the three integrals in (5.33) can be expressed in analytic form, but the resulting expressions are omitted for brevity. In the steady-state limit $t \to \infty$, one finds

$$\bar{\tau}_\infty = \frac{\sqrt{3}}{6\left(1+\sqrt{3}\right)} \approx 0.1057. \tag{5.34}$$

Fig. 5.4 shows the corresponding steady-state shear-stress distribution along the duct. Line segments depict relative shear magnitude, their lengths proportional to the local shear-stress intensity.

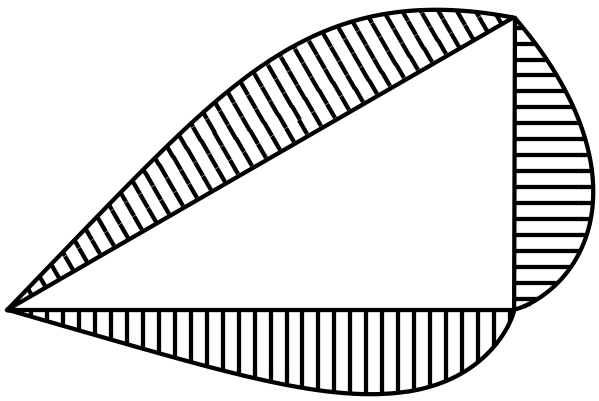

Figure 5.4: Steady-state shear stress distribution in a hemi-equilateral triangular duct.

5.4.2 Right-angled isosceles triangular duct

Now consider the right-angled isosceles triangular duct, whose cross-section is given by $\Gamma = \{(x, y) \in \mathbb{R}^2 : 0 < x < 1,\ 0 < y < 1 - x\}$, as illustrated in Fig. 5.5. The eigenfunctions and associated eigenvalues of Eq. (5.4) in this domain are given by [166]

$$\phi_{mn} = \sin\left[(m+n)\pi x\right]\sin(n\pi y) - (-1)^m \sin\left[(m+n)\pi y\right]\sin(n\pi x), \tag{5.35}$$

and

$$\lambda_{mn} = \left[(m+n)^2 + n^2\right]\pi^2, \tag{5.36}$$

where $m, n \in \mathbb{Z}^+$. The first six eigenvalues are $\lambda_{11} \approx 49.3480$, $\lambda_{21} \approx 98.6960$, $\lambda_{12} \approx 128.3049$, $\lambda_{31} \approx 167.7833$, $\lambda_{22} \approx 197.3921$, and $\lambda_{13} \approx 246.7401$. The nodal domains corresponding to these eigenfunctions are shown in Fig. 5.6.

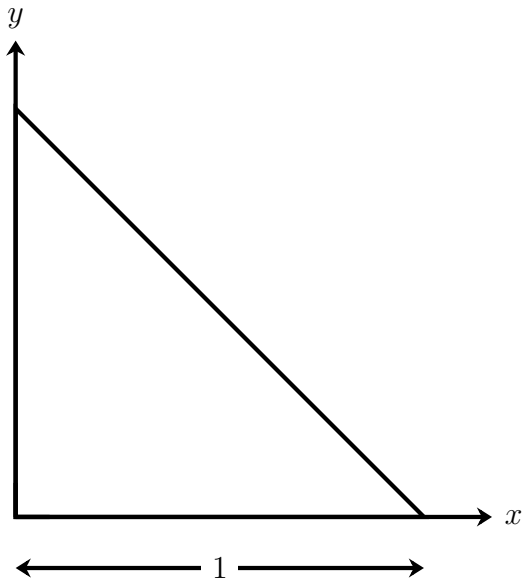

Figure 5.5: Right-angled isosceles triangular duct.

The coefficients α_{mn} and β_{mn}, from Eqs. (5.6) and (5.36), are

$$\alpha_{mn} = \frac{1}{\pi^2}\frac{1-(-1)^m}{n(m+n)}\left[1 - (-1)^n \frac{(m+n)^2 + n^2}{(m+n)^2 - n^2}\right], \qquad \beta_{mn} = \frac{1}{4}. \tag{5.37}$$

It is worth noting that Eq. (11) in Ref. [166] contains a typographical error: the factor $(-1)^m$ appearing in the second term should read $(-1)^n$.

Substituting into Eq. (5.7), the velocity field becomes

$$w = \sum_{m=1}^{\infty}\sum_{n=1}^{\infty} \frac{4}{\lambda_{mn}\pi^2}\frac{1-(-1)^m}{n(m+n)}\left[1 - (-1)^n \frac{(m+n)^2 + n^2}{(m+n)^2 - n^2}\right]\phi_{mn}\left(1 - \mathrm{e}^{-\lambda_{mn}t}\right), \tag{5.38}$$

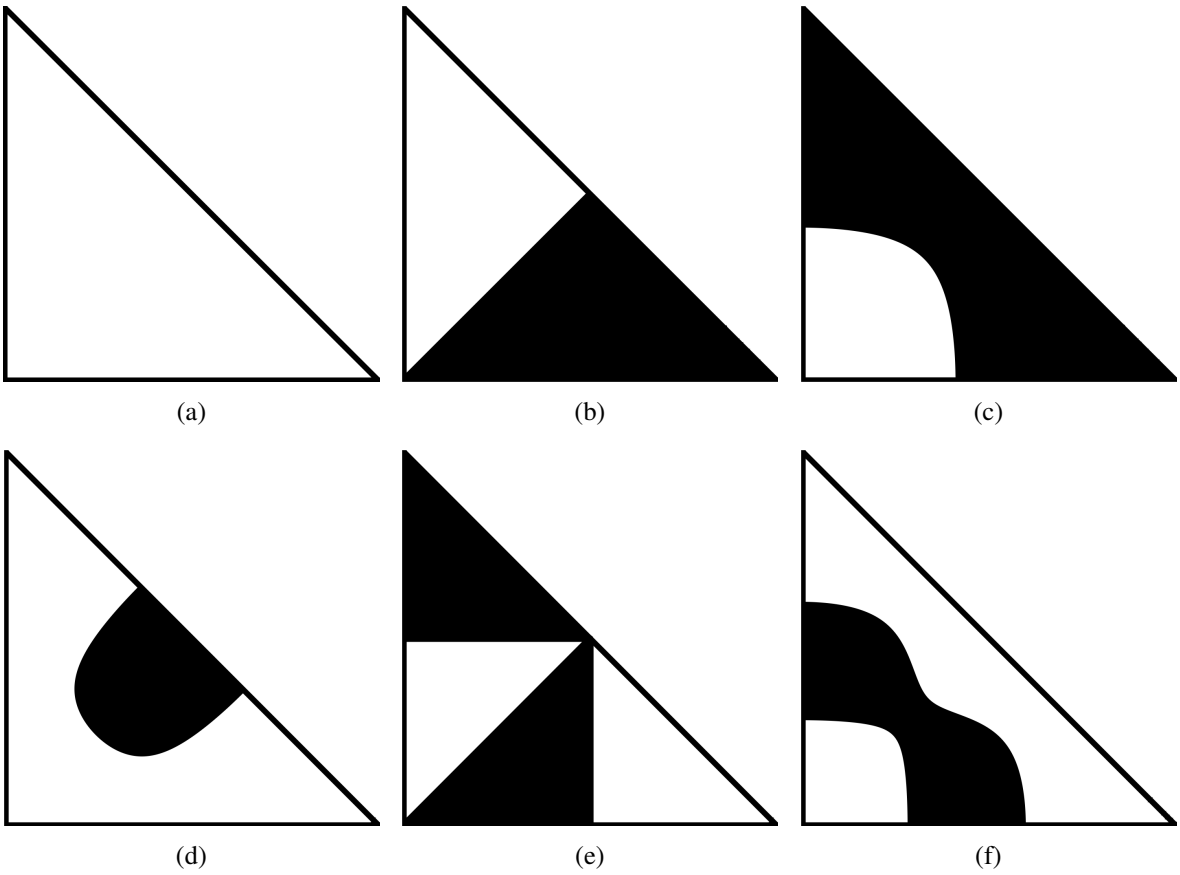

Figure 5.6: Dirichlet eigenfunction nodal domains for the isosceles right triangle: (a) λ_{11}, (b) λ_{21} (c) λ_{12}, (d) λ_{31}, (e) λ_{22} and (f) λ_{13}.

and the corresponding flow rate is

$$Q = \sum_{m=1}^{\infty}\sum_{n=1}^{\infty} \frac{4}{\lambda_{mn}\pi^4} \frac{[1-(-1)^m]^2}{n^2(m+n)^2} \left[1-(-1)^n \frac{(m+n)^2+n^2}{(m+n)^2-n^2}\right]^2 \left(1-\mathrm{e}^{-\lambda_{mn}t}\right). \tag{5.39}$$

In the long-time limit, this series converges to

$$Q_\infty \approx 6.5224 \times 10^{-3}. \tag{5.40}$$

The velocity field given by Eq. (5.38) is illustrated at selected times in Fig. 5.7.

From Eqs. (5.10) and (5.40), with $A = 1/2$ and $P = 2+\sqrt{2}$, it follows that

$$Po \approx 13.1526. \tag{5.41}$$

Alternatively, the steady solution derived by Proudman [167] reads, in our variables,

$$w_\infty = \frac{y(1-x-y)}{2} + \sum_{n=1}^{\infty} \frac{\sin[2N(1-x)]\sinh(2Ny) - \sinh[2N(1-x)]\sin(2Ny)}{2N^3\sinh(2N)}, \tag{5.42}$$

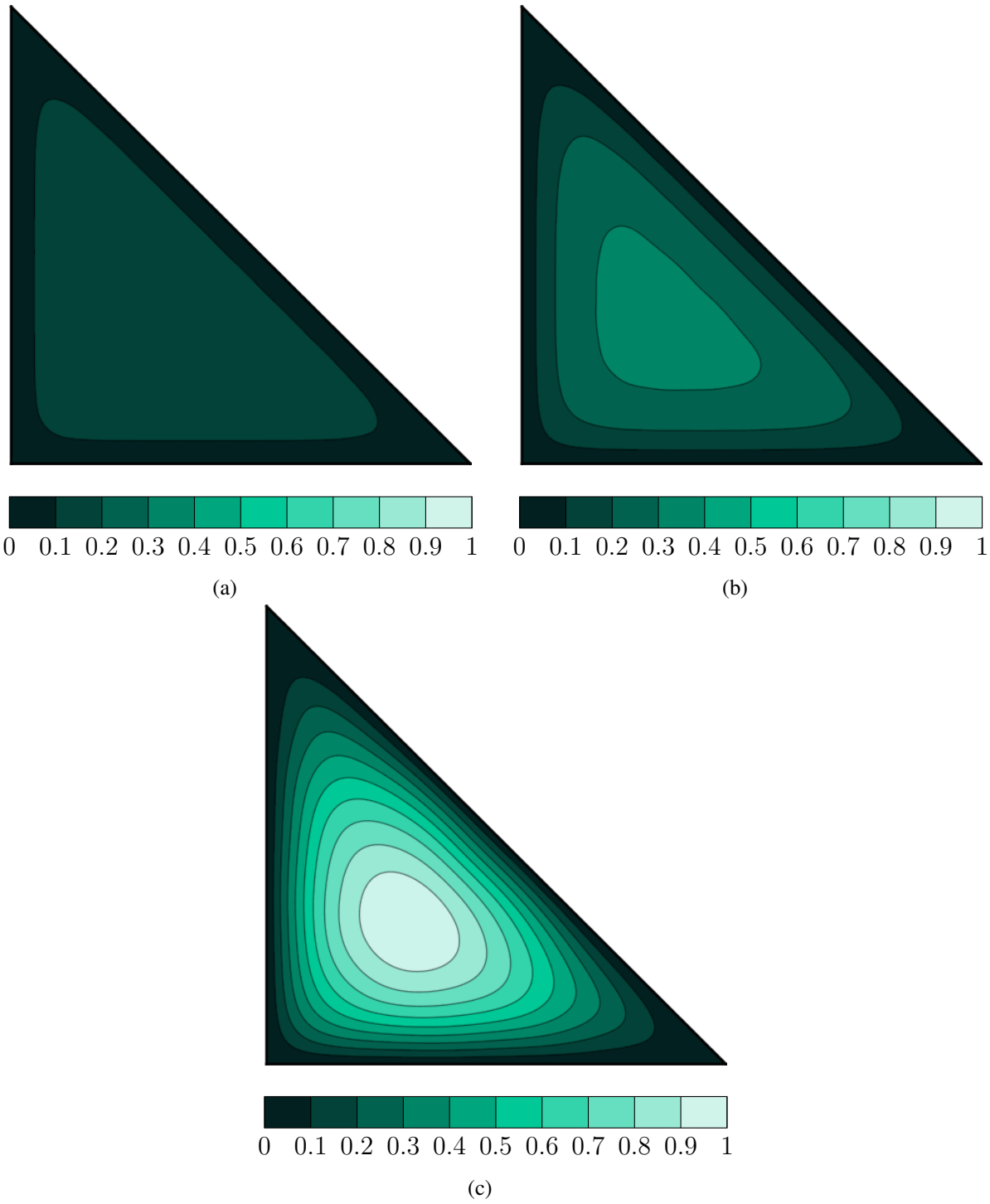

Figure 5.7: Velocity field in the right-angled isosceles triangular duct: (a) $t = 0.005$, (b) $t = 0.01$, and (c) $t = 0.1$. The colour scale is normalized by the steady-state maximum velocity, $w_{\max} \approx 0.0295$.

where

$$N = \frac{(2n-1)\pi}{2}. \tag{5.43}$$

Integration of Eq. (5.42) over the triangular domain yields the steady flow rate

$$Q_\infty = \frac{1}{48} - \sum_{n=1}^{\infty} \frac{\coth(N)}{8N^5}, \tag{5.44}$$

whose numerical value matches that obtained from Eq. (5.39).

On the horizontal segment $(0 \le x \le 1,\ y = 0)$, the shear stress is

$$\tau_{w,1} = \tau_{yz}(x,0) = \sum_{m=1}^{\infty}\sum_{n=1}^{\infty} \frac{\alpha_{mn}}{\beta_{mn}\lambda_{mn}} \frac{\partial \phi_{mn}}{\partial y}(x,0)\left(1 - e^{-\lambda_{mn} t}\right). \tag{5.45}$$

On the vertical segment $(x = 0,\ 0 \le y \le 1)$, the shear stress is

$$\tau_{w,2} = \tau_{xz}(0,y) = \sum_{m=1}^{\infty}\sum_{n=1}^{\infty} \frac{\alpha_{mn}}{\beta_{mn}\lambda_{mn}} \frac{\partial \phi_{mn}}{\partial x}(0,y)\left(1 - e^{-\lambda_{mn} t}\right). \tag{5.46}$$

On the inclined segment $(0 \le x \le 1,\ y = 1 - x)$, the shear stress is

$$\begin{aligned} \tau_{w,3} &= -\frac{1}{\sqrt{2}}\left[\tau_{xz}(x,1-x) + \tau_{yz}(x,1-x)\right] \\ &= -\frac{1}{\sqrt{2}}\sum_{m=1}^{\infty}\sum_{n=1}^{\infty} \frac{\alpha_{mn}}{\beta_{mn}\lambda_{mn}}\left[\frac{\partial \phi_{mn}}{\partial x}(x,1-x) + \frac{\partial \phi_{mn}}{\partial y}(x,1-x)\right]\left(1 - e^{-\lambda_{mn} t}\right). \end{aligned} \tag{5.47}$$

From Eq.(5.11), the mean wall shear stress is

$$\bar{\tau} = \frac{1}{2+\sqrt{2}}\left[\int_0^1 \tau_{w,1}\,dx + \int_0^1 \tau_{w,2}\,dy + \sqrt{2}\int_0^1 \tau_{w,3}\,dx\right]. \tag{5.48}$$

Although each integral in Eq. (5.48) can be evaluated analytically, the explicit formulas are lengthy and are therefore not displayed here. Taking the limit $t \to \infty$ gives

$$\bar{\tau}_{\infty} = \frac{1}{2\left(2+\sqrt{2}\right)} \approx 0.1464, \tag{5.49}$$

and the corresponding steady distribution along the three sides is shown in Fig. 5.8.

5.5 Conclusion

This study presented new exact analytical solutions for the startup of Poiseuille flow in hemi-equilateral and right-angled isosceles triangular ducts. By employing the eigenfunction superposition method, we derived series solutions for the transient velocity field, volumetric flow rate, and wall shear stress distribution, thereby extending the classical steady-state solutions to the time-dependent regime. The analytical expressions obtained here provide valuable benchmarks for validating numerical simulations and for investigating transient phenomena in non-circular ducts.

Together with the equilateral-triangle case previously solved by Wang [151], these results complete the set of triangular cross-sections that admit trigonometric eigenfunctions of the Laplacian under Dirichlet boundary conditions.

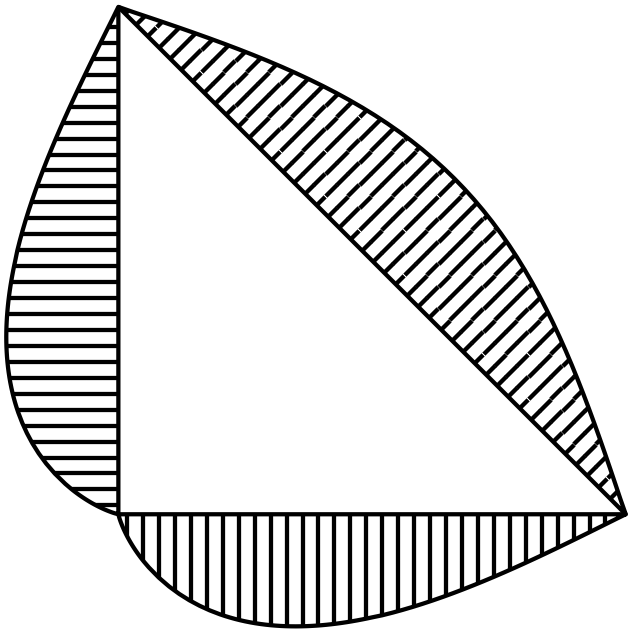

Figure 5.8: Steady-state shear stress distribution in a right-angled isosceles triangular duct.

Chapter 6

Revisiting Darcy–Brinkman flow through an elliptic tube

This chapter is a reproduction of the following publication:

Lopes, A. B.; Far, M. E. F.; Silva, V. C. Revisiting Darcy–Brinkman Flow Through an Elliptic Tube. Transport in Porous Media, Vol. 153, No. 1, pp. 13, 2025.

6.1 Introduction

Fully developed laminar flow through tubes of uniform cross-section under a constant pressure gradient, commonly referred to as Poiseuille flow, has long been a central problem in fluid mechanics. Exact solutions are of considerable interest in engineering applications and continue to serve as benchmarks for both theoretical analysis and numerical validation, with a comprehensive summary for over 30 geometries available in the seminal reference by Shah and London [33]. The extension to porous media, however, remains relatively less explored, particularly in the context of Darcy–Brinkman flow. While Poiseuille flow leads to a Poisson equation, the inclusion of a linear drag term in Darcy–Brinkman flow results in a nonhomogeneous Helmholtz equation. As a consequence, analytical solutions are available only for a limited set of canonical geometries, including parallel plates, rectangular ducts, circular tubes, and concentric annuli, as compiled in the technical report by Ramacharyulu [168]. Other contributions include exact solutions for elliptic tubes [169], semi-circular tubes [170], sector-shaped tubes [171], and, more recently, equilateral triangular tubes [172].

Although the velocity field in an elliptic tube was derived by Narasimhacharyulu and Pattabhiramacharyulu [169], the corresponding Poiseuille number was not. This remains the only Darcy–Brinkman case among those cited without an exact expression for this hydrodynamic parameter, which is of utmost importance in practical applications. The present work revisits the elliptic geometry and completes the analytical description by deriving, for the first time, an exact series expression for the Poiseuille number.

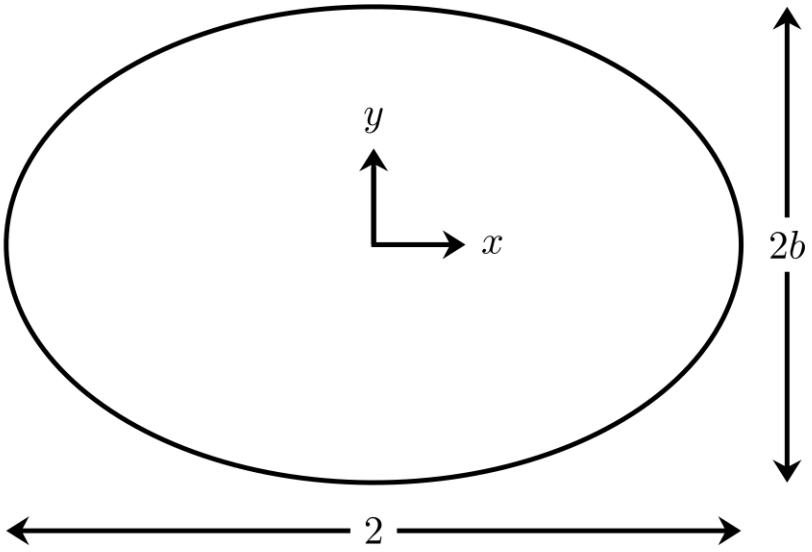

Figure 6.1: Cross-section of the elliptic tube.

Elliptic geometries and their variants arise naturally in heat exchangers, microfluidic systems, and biomedical flows. In the context of Poiseuille flow, recent theoretical contributions include works on semi-elliptic tubes [173, 174, 175], confocal semi-elliptic annuli [79], and quarter-elliptic tubes [144]. For Darcy–Brinkman flow, aside from the classical solution by Narasimhacharyulu and Pattabhiramacharyulu [169], the most notable theoretical contributions are those by Haji-Sheikh and Vafai [176] and Wang [177], who employed the Ritz method to compute approximate solutions for elliptic and super-elliptic cross-sections, respectively.

6.2 Formulation

We consider the steady, fully developed flow of an incompressible fluid through a tube filled with a Darcy-Brinkman medium. The tube has elliptical cross-section with semi-axes L and bL, where b is the aspect ratio. The flow is driven by a constant axial pressure gradient $-G$, and the axial direction is z. The fluid has density ρ and dynamic viscosity μ; the saturated porous matrix has effective viscosity μ_e and permeability K. Lengths are scaled by L, and velocity by GL^2/μ_e. The cross-section of the elliptic tube is shown in Fig. 6.1.

The non-dimensional axial velocity $w(x, y)$ satisfies the Darcy-Brinkman equation

$$\nabla^2 w - s^2 w + 1 = 0, \tag{6.1}$$

where $s = L/\sqrt{\mu_e K/\mu}$ is the porous medium parameter.

We introduce elliptic coordinates (ξ, θ) via the conformal mapping [178]

$$x + iy = c\cosh(\xi + i\theta), \tag{6.2}$$

where $c = \sqrt{1-b^2}$ is the dimensionless linear eccentricity. In these coordinates, Eq. (6.1) becomes

$$\frac{2}{c^2(\cosh 2\xi - \cos 2\theta)}\left(\frac{\partial^2 w}{\partial \xi^2} + \frac{\partial^2 w}{\partial \theta^2}\right) - s^2 w = -1, \tag{6.3}$$

and the wall corresponds to the ellipse $\xi = \xi_0$, with $\xi_0 = \tanh^{-1} b$.

The boundary conditions are the no-slip condition

$$w|_{\xi=\xi_0} = 0, \tag{6.4}$$

along with the symmetry conditions

$$\left.\frac{\partial w}{\partial \xi}\right|_{\xi=0} = \left.\frac{\partial w}{\partial \theta}\right|_{\theta=0} = \left.\frac{\partial w}{\partial \theta}\right|_{\theta=\frac{\pi}{2}} = 0. \tag{6.5}$$

The non-dimensional volumetric flow rate, scaled by GL^4/μ_e, is

$$Q = 2c^2 \int_0^{\xi_0} \int_0^{\frac{\pi}{2}} w\,(\cosh 2\xi - \cos 2\theta)\,\mathrm{d}\theta\,\mathrm{d}\xi, \tag{6.6}$$

and the Poiseuille number is given by

$$Po = \frac{8A^3}{P^2 Q}, \tag{6.7}$$

where

$$A = \pi b, \tag{6.8}$$

is the non-dimensional area, and

$$P = 4E\left(1 - b^2\right), \tag{6.9}$$

is the wetted perimeter. In Eq. (6.9), $E(k)$ is the complete elliptic integral of the second kind [179].

6.3 Solution

The solution to Eqs. (6.3)–(6.5) was first obtained by [169], and is given by

$$w = \frac{1}{s^2}\left[1 + 2\pi \sum_{n=0}^{\infty} \frac{(-1)^{n+1} A_0^{(2n)}}{\mathrm{Ce}_{2n}(\xi_0, -q)\, F_{2n}} \mathrm{Ce}_{2n}(\xi, -q)\ \mathrm{ce}_{2n}(\theta, -q)\right], \tag{6.10}$$

where

$$\mathrm{ce}_{2n}(\theta, -q) = (-1)^n \sum_{r=0}^{\infty} (-1)^r A_{2r}^{(2n)} \cos(2r\theta), \tag{6.11}$$

and

$$\mathrm{Ce}_{2n}(\xi,-q) = (-1)^n \sum_{r=0}^{\infty} (-1)^r A_{2r}^{(2n)} \cosh(2r\xi), \tag{6.12}$$

are even and modified Mathieu functions, respectively [180]. Here, $A_{2r}^{(2n)}$ are Fourier coefficients,

$$F_{2n} = \begin{cases} 2\pi, & n = 0, \\ \pi, & n \geq 1, \end{cases} \tag{6.13}$$

and the Mathieu parameter is

$$q = \frac{c^2 s^2}{4}. \tag{6.14}$$

We note that Eq. (17) in [169] contains a typographical error: the first occurrence of $\mathrm{Ce}_{2n}(\xi,-q)$ should read $\mathrm{Ce}_{2n}(\xi_0,-q)$. The velocity field is thus known. We now derive exact expressions for the flow rate and Poiseuille number.

Rather than substituting Eq. (6.10) directly into Eq. (6.6) to evaluate the non-dimensional volumetric flow rate, we proceed differently. Multiplying both sides of Eq. (6.3) by $\cosh 2\xi - \cos 2\theta$ and integrating θ from 0 to $\pi/2$ and ξ from 0 to ξ_0, we obtain

$$\frac{2}{c^2} \int_0^{\xi_0} \int_0^{\frac{\pi}{2}} \left(\frac{\partial^2 w}{\partial \xi^2} + \frac{\partial^2 w}{\partial \theta^2} \right) \mathrm{d}\theta \, \mathrm{d}\xi - \frac{s^2 Q}{2c^2} = -\frac{\pi \sinh 2\xi_0}{4}, \tag{6.15}$$

from which follows that

$$Q = \frac{1}{2s^2} \left[\pi c^2 \sinh 2\xi_0 + 8 \int_0^{\xi_0} \int_0^{\frac{\pi}{2}} \left(\frac{\partial^2 w}{\partial \xi^2} + \frac{\partial^2 w}{\partial \theta^2} \right) \mathrm{d}\theta \, \mathrm{d}\xi \right]. \tag{6.16}$$

Applying Green's theorem to the double integral in Eq. (6.16), we obtain

$$\int_0^{\xi_0} \int_0^{\frac{\pi}{2}} \left(\frac{\partial^2 w}{\partial \xi^2} + \frac{\partial^2 w}{\partial \theta^2} \right) \mathrm{d}\theta \, \mathrm{d}\xi = \int_0^{\frac{\pi}{2}} \left. \frac{\partial w}{\partial \xi} \right|_{\xi=\xi_0} \mathrm{d}\theta, \tag{6.17}$$

where the symmetry conditions in Eq. (6.5) have been used. Hence,

$$Q = \frac{\pi}{2s^2} \left[c^2 \sinh 2\xi_0 + \frac{8}{\pi} \int_0^{\frac{\pi}{2}} \left. \frac{\partial w}{\partial \xi} \right|_{\xi=\xi_0} \mathrm{d}\theta \right]. \tag{6.18}$$

Substituting Eq. (6.10) into Eq. (6.18) yields

$$Q = \frac{\pi}{2s^2} \left[c^2 \sinh 2\xi_0 + \frac{16}{s^2} \sum_{n=0}^{\infty} \frac{(-1)^{n+1} A_0^{(2n)} \, \mathrm{Ce}'_{2n}(\xi_0,-q)}{\mathrm{Ce}_{2n}(\xi_0,-q) \, F_{2n}} \int_0^{\frac{\pi}{2}} \mathrm{ce}_{2n}(\theta,-q) \, \mathrm{d}\theta \right], \tag{6.19}$$

where $\mathrm{Ce}'_{2n}(\xi,-q)$ is the derivative of the modified Mathieu function with respect to ξ. From the Fourier expansion (6.11), we find

$$\int_0^{\frac{\pi}{2}} \mathrm{ce}_{2n}(\theta,-q) \, \mathrm{d}\theta = \frac{(-1)^n \pi A_0^{(2n)}}{2}, \tag{6.20}$$

which leads to the exact expression

$$Q = \frac{\pi}{2s^2}\left[c^2 \sinh 2\xi_0 - \frac{8\pi}{s^2}\sum_{n=0}^{\infty}\left(A_0^{(2n)}\right)^2 \frac{\mathrm{Ce}'_{2n}(\xi_0,-q)}{\mathrm{Ce}_{2n}(\xi_0,-q)\,F_{2n}}\right]. \tag{6.21}$$

Then

$$Po = \frac{\pi^3 b^3}{2\left[E\left(1-b^2\right)\right]^2 Q}. \tag{6.22}$$

This result has not been reported before.

Direct evaluation of Eq. (6.21) requires the computation of modified Mathieu functions and their derivatives, which is known to be numerically delicate due to their oscillatory nature and stiffness [181]. To ensure numerical stability and accuracy, we employed high-precision symbolic–numerical routines in Maple 2025. The coefficients $A_0^{(2n)}$ were obtained by numerical integration, based on Eq. (6.20).

It is useful to observe that, for a clear viscous fluid ($s = 0$) flowing through an elliptic tube,

$$Po = \frac{2\pi^2(1+b^2)}{\left[E\left(1-b^2\right)\right]^2}. \tag{6.23}$$

For a circular tube ($b = 1$), Eq. (6.22) becomes

$$Po = \frac{2s^2}{1 - \dfrac{2I_1(s)}{sI_0(s)}}, \tag{6.24}$$

as reported by [177], where $I_n(s)$ is the modified Bessel function of the first kind of order n. Both expressions (6.23) and (6.24) follow as limiting cases of Eq. (6.22).

6.4 Results

Once the analytical expressions of interest were obtained, isovelocity curves were plotted to provide a clearer physical interpretation of the phenomena involved. Fig. 6.2 shows the normalized velocity contours for $b = 0.5$ and increasing values of the porous-medium parameter s, as obtained from Eq. (6.10). As s increases from 1 to 10, the velocity profile becomes more flattened, with sharper gradients near the boundary and a nearly uniform core. This behavior reflects the increased damping associated with the porous matrix. In all cases, the contours conform to the elliptic geometry, and the innermost contours shrink significantly with increasing s. The transition to a plug-like profile is evident, consistent with the known behavior of Darcy–Brinkman flows in confined geometries.

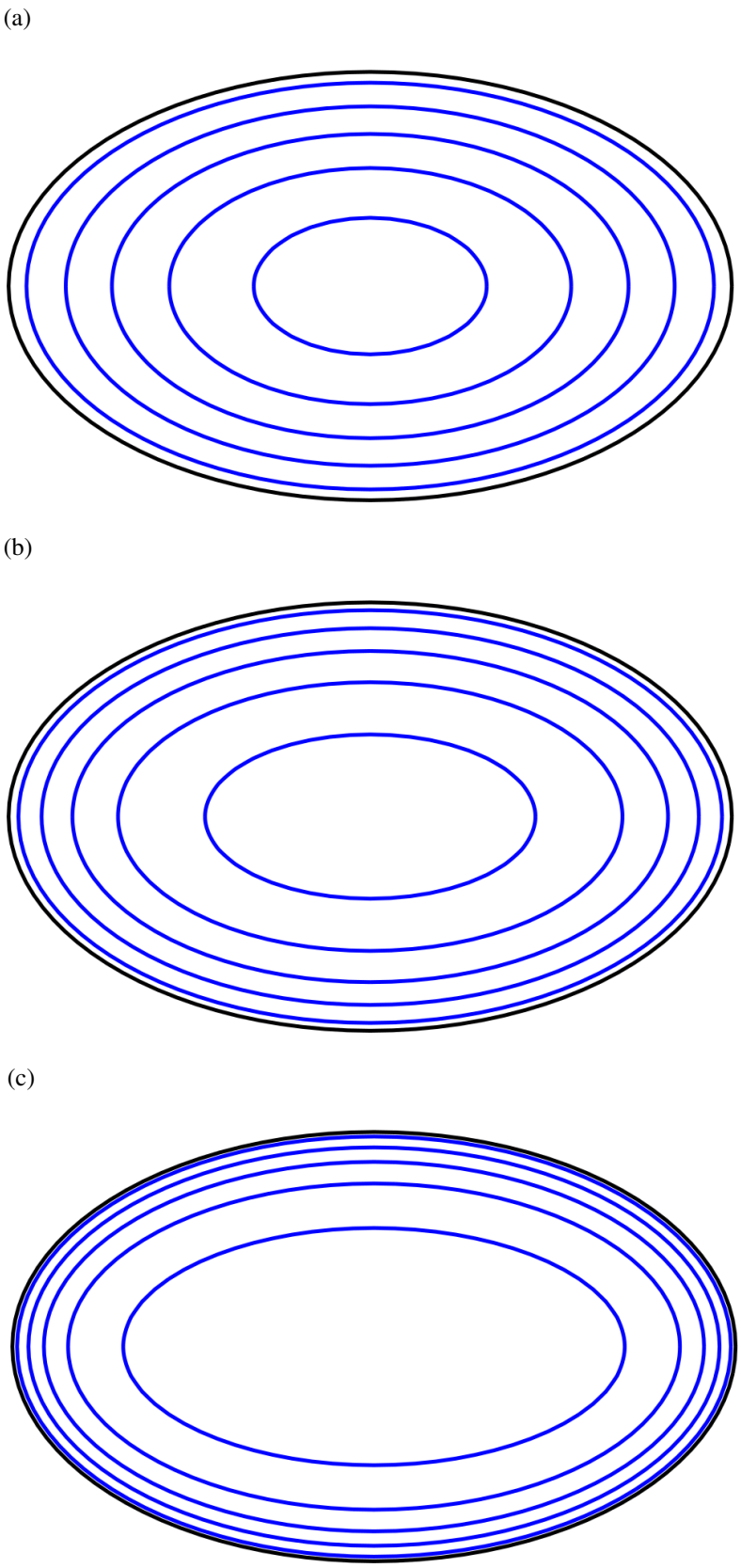

Figure 6.2: Normalized velocity contour lines for $b = 0.5$ and (a) $s = 1$, (b) $s = 5$, and (c) $s = 10$. Contours levels from the outermost to the innermost are 0.1, 0.3, . . ., 0.9.

Since the exact expression for Q in Eq. (6.21) is an infinite series, we truncate at $N = 64$,

which yields ten-digit stability across (s, b). Convergence was checked by doubling the number of retained terms. For small s (e.g. $s \leq 10$), $N = 8$ already suffices, but we adopt $N = 64$ uniformly.

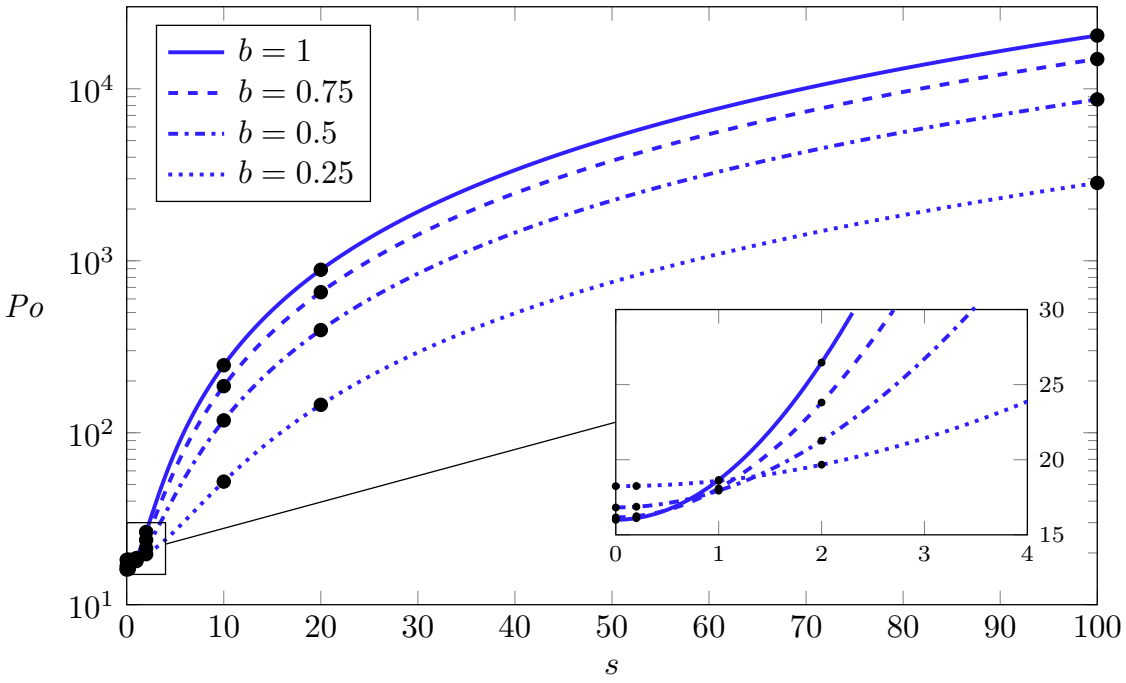

Figure 6.3: Poiseuille number, *Po*, versus s for four elliptic tubes. Lines are finite-element results; circles are analytical values from Table 6.1.

Because [176] and [177] report only 4–5 significant digits, we validate the series by a finite-element computation in FreeFEM [102], solving Eq. (6.3) subject to Eqs. (6.4) and (6.5). Quadratic Lagrange ($P2$) elements are employed on dyadically refined structured meshes 128×128, 256×256, and 512×512, with Richardson extrapolation [182] to 1024×1024; area integrals use FreeFEM's Gaussian quadrature. Fig. 6.3 summarizes the comparison: *Po* is plotted against s for four aspect ratios, with lines from the Richardson–extrapolated FEM solution and circles from the series (Eqs. (6.22), (6.23) and (6.24)); the inset highlights the small-s regime, where the agreement is likewise excellent. Table 6.1 reports *Po* for selected (s, b), listing the series value and, in parentheses, the extrapolated FEM value. In the great majority of cases the two values coincide to all ten reported digits; when differences occur they are usually confined to the last one or two digits. The largest observed relative difference is 1.19×10^{-4} (about 0.012%) at $(s, b) = (100, 0.25)$; elsewhere the differences are smaller.

6.5 Conclusions

We complete the isothermal Darcy–Brinkman analysis for elliptic tubes by deriving an exact series for the flow rate, which yields the Poiseuille number directly. The derivation

Table 6.1: *Po* values for elliptic tubes.

$s \setminus b$	0.25	0.5	0.75	1
0	18.23995922	16.82330362	16.16098937	16.00000000
0.2	18.25426450 (18.25426450)	16.86816121 (16.86816121)	16.23855002 (16.23855002)	16.10664447
1	18.59724972 (18.59724982)	17.94206252 (17.94206115)	18.09293014 (18.09292982)	18.65322447
2	19.66499933 (19.66499906)	21.26712883 (21.26712883)	23.80841718 (23.80841718)	26.47031498
10	51.97189123 (51.97189101)	117.9519419 (117.9519419)	186.6415514 (186.6415514)	246.8282463
20	145.2550660 (145.2550659)	395.3964560 (395.3964560)	656.5604581 (656.5604580)	886.3942316
100	2835.735662 (2836.072976)	8677.515268 (8677.515300)	14892.15736 (14892.15737)	20406.07575

Values in parentheses are numerical.

hinges on the Mathieu-function representation and a Green-identity reduction that converts area integrals to boundary terms. The expression recovers the classical clear-fluid elliptic result and the circular Brinkman limit, and it is consistent with the finite-element solutions reported here. Beyond settling the outstanding analytical case, the formula offers a high-accuracy benchmark for numerical methods and asymptotic approximations in porous-duct flows.

Chapter 7

Numerical Implementation

In this section, we present the FreeFEM implementation associated with each paper in order to clarify the procedures adopted and to highlight the actual technical effort involved, including steps that might not be immediately apparent from the published results.

7.1 FreeFEM

FreeFEM [102] is an open-source finite element software dedicated to the numerical solution of systems of partial differential equations. It is built around a high-level language with a C++ syntax that allows users to define weak (variational) formulations in a way that closely mirrors their mathematical expressions, facilitating a direct translation from theory to implementation. Governing equations, boundary conditions, and coupling terms can be introduced directly at the variational level, without requiring explicit assembly of system matrices. This feature makes FreeFEM particularly well suited for problems involving non-standard operators, customized boundary conditions, or parameter-dependent formulations.

One of the main advantages of FreeFEM is its extensive support for mesh generation and manipulation. The software allows for the construction of meshes directly from geometric descriptions and also supports the import of meshes generated by external tools, ensuring compatibility with other computational softwares, such as Gmsh [183]. Furthermore, adaptive mesh refinement and remeshing procedures are natively available, enabling the user to improve the resolution of localized phenomena such as boundary layers, singularities, and sharp gradients. As an open-source platform, FreeFEM offers integration with external libraries and fast numerical solvers, including interfaces to advanced linear algebra packages and parallel computing frameworks.

Due to these characteristics, FreeFEM has been widely adopted in academic research [184, 185, 186]. For these reasons, it is employed in the present work as the primary computational environment. The algorithm implemented in FreeFEM is guided by the following steps: geometric definition, mesh generation, finite element discretization, time in-

tegration, and post-processing. Selected fragments of the computational script are presented below to illustrate the main implementation steps.

7.1.1 Definition of the computational domain

The boundary of the computational domain is defined parametrically using the `border` keyword. Each border corresponds to a segment of the boundary and is described as a function of a specified parameter, in this case $t \in [0, 1]$ meaning that the time variable follows a path from 0 to 1 and reversing its orientation $t \in [1, 0]$ would correspond to an evolution from 1 to 0.

```
border C01(t=0,1){ x = 1 - t; y = 0; label = 1; }
border C02(t=0,1){ x = 1; y = (1 - t)/sqrt(3); label = 2; }
border C03(t=0,1){ x = t; y = t/sqrt(3); label = 3; }
```

Applying the formulation to a triangular cross section, for illustrative purposes, whose boundary is described by the following parametric border segments, these border definitions describe a closed contour formed by straight line segments that together form an equilateral triangular cross section with vertices at $(0, 0), (1, 0), (1, \sqrt{3}/3)$. The parametric representation facilitates future modifications or extensions, if needed.

In addition, is notable that the contour is defined with a clockwise orientation, determining the direction of the outward normal vector according to FreeFEM's convention. The correct orientation is essential for the evaluation of boundary integrals and for the imposition of boundary conditions in the variational formulation, while the integer labels associated with each border segment allow for the assignment of independent boundary conditions to different portions of the boundary.

7.1.2 Mesh generation

Once the boundary is defined, the mesh is generated using the command `buildmesh`, which internally employs a Delaunay–Voronoi triangulation algorithm. The Delaunay–Voronoi algorithm is a method for generating meshes by connecting points to form triangles. It is based on maximizing the minimum angle of the triangles in the mesh. By doing so, it avoids the formation of long and narrow elements, leading to improved mesh quality and improved numerical stability.

```
mesh Th = buildmesh( C01(40) + C02(40) + C03(40) );
```

The integer arguments inside the border definition specify the number of discretization points on each border segment, controlling the mesh density and the divisions in each bound-

ary. The resulting mesh object `Th` contains the connectivity, nodal coordinates, and element information required for the finite element assembly.

The geometric quantities of the domain, such as the total area and the perimeter, are evaluated directly from the mesh `Th` and later used for obtaining the Poiseuille number.

7.1.3 Numerical integration

The finite element formulation involves the evaluation of domain integrals. Since these integrals generally cannot be computed analytically on arbitrary meshes and curved geometries, numerical quadrature rules are employed.

A quadrature rule is a numerical technique used to approximate integrals when an exact evaluation is not feasible. Instead of computing the integral directly, the idea is to evaluate the function at a finite number of carefully chosen points $f(\xi_\ell)$ inside the domain and combine these values using predefined weights ω_ℓ. In this way, the continuous integral is replaced by a finite weighted sum, which can be efficiently computed by a CPU. Quadrature rules are widely used in numerical methods, particularly in the finite element method, to evaluate integrals arising from variational formulations.

$$\int_D f(\mathbf{x})\, d\mathbf{x} \approx \sum_{\ell=1}^{L} \omega_\ell f(\xi_\ell). \tag{7.1}$$

A quadrature rule is said to be exact for polynomials of degree up to r if (7.1) reproduces exactly the integral of any polynomial f of degree at most r.

In finite element formulations, the integrands typically involve products of basis functions and their gradients. These quantities are polynomial functions when standard Lagrange elements are used. By choosing an appropriate Gaussian quadrature rule, these integrals can be evaluated either exactly or with negligible numerical error, ensuring that the accuracy of the solution is preserved.

The integrals appearing in the variational formulation are decomposed into sums of integrals over individual mesh elements $K \in \mathcal{T}_h$. Each elemental integral is mapped to a reference element, where standard quadrature rules are applied. The choice of the quadrature order is consistent with the polynomial degree of the basis functions in order to preserve the accuracy.

In the present implementation, numerical integration is handled internally by the FreeFEM library, which automatically selects appropriate quadrature rules for each form.

7.1.4 Finite element space

The finite element approximation space V_h is defined as a space of continuous piecewise quadratic functions (`P2`) over the mesh T_h using the keyword `fespace` to define the finite-

dimensional space necessary to find the solution.

```
fespace Vh(Th, P2);
Vh u, v, uold;
```

The unknown field u and the test function v are declared as elements of this space, while `uold` stores the solution from the previous time step, in this case, it is already stored as `uold=` 0.

7.1.5 Variational formulation

The weak form of the transient Poisson equation is implemented inside the `problem` area. The problem is defined by introducing a variational form that incorporates both the spatial discretization and the temporal advancement within a single formulation.

```
problem vPoisson (u, v)
 = int2d(Th)(u*v/dt + grad(u)' * grad(v))
 - int2d(Th)(f * v)
 - int2d(Th)(uold*v/dt)
 + on(1, u=0);
```

Dirichlet boundary conditions are enforced weakly through the variational formulation by prescribing a vanishing velocity at the boundary. The remaining formulation follows the classical Galerkin approach, as the trial and test functions are chosen from the same finite element space.

7.1.6 Time integration loop

At each time step, the solution obtained at the previous instant is stored and employed as initial data for the subsequent iteration. In the present implementation, the time advancement is carried out within the variational formulation itself, as the temporal discretization is embedded in the function `vPoisson`. As a result, a Poisson-type problem is solved repeatedly at each time step, advancing the solution in time through an implicit time discretization scheme.

```
for (int n = 0; n < Nt; n++)
{
    uold = u;
    vPoisson;
}
```

At each iteration, the linear system associated with the variational problem is solved, and the updated solution is stored for the next time step.

7.1.7 Post-processing

Integral quantities of interest are evaluated directly from the numerical solution using Freefem's quadrature integration.

```
Uh ff = 1;
real perim = int1d(Th,1)(ff);
real area = int2d(Th)(ff);
real vaz = int2d(Th)(u);
real maxu = u[].max;
real fre = 8*area^3/perim^2/vaz;;
```

The volumetric flow rate is computed by numerical integration of the velocity field over the cross-section, while the geometric area is obtained directly from the mesh, both using the `int2d` command. In contrast, the wetted perimeter requires integration along the boundary and is therefore computed using the `int1d` command applied to the domain border. These quantities are used to evaluate the Poiseuille number (fRe).

In addition, the maximum value of the velocity field is extracted using the FreeFEM instruction `u[].max`, which provides the peak nodal velocity for comparison with the maximum velocity found analytically.

The numerical solutions developed in the context of this dissertation are employed as a validation and investigation tool for cases where analytical treatment is unavailable. In all papers presented in this work, the consistency between analytical and numerical solutions was verified, although this validation step was not always explicitly reported in the final manuscripts. The level of detail dedicated to numerical validation on each paper depended on the scope of each contribution and journal context, particularly when the primary focus was placed on theoretical developments or analytical advances.

7.2 Discussion

7.2.1 Poiseuille flow through parabolic segment and lens-shaped ducts

In Chapter 3, the Poisson equation with homogeneous Dirichlet boundary conditions is solved for each considered geometry, including both parabolic and parabolic–lens cross sections. For this purpose, a dedicated mesh generation procedure is carried out for every geometry and for the corresponding values of the geometric parameter The parameter α is varied over a wide range, from $\alpha = 0.03$ up to $\alpha = 10^4$, which corresponds to the practical operational limits of the available machine.

The mesh generation is performed independently for each configuration, with the objective of obtaining meshes containing approximately 8×10^5 quadratic (P2) triangular elements.

This upper limit is dictated primarily by the available random access memory (RAM) of the computational platform used to solve the problem.

Since the adopted discretization strategy is based on subdividing each boundary segment into a prescribed number of intervals, the final number of elements in the mesh cannot be determined a priori. To address this issue, preliminary mesh-generation runs are performed for three representative cases: the geometry with the smallest area, the geometry with the largest area, and an intermediate configuration. Based on the resulting element counts, an empirical scaling law of the form

$$n(\alpha) = A - B\,\alpha^{p}, \tag{7.2}$$

was adopted, where n denotes the number of subdivisions imposed on each boundary segment, α is the geometric parameter, and A, B, and p are fitting constants determined from preliminary mesh-generation runs.

It is worth noting that the linear systems arising from the finite element discretization are solved using a direct solver for all problems presented in this work, providing an exact solution of the algebraic system and a sufficient level of accuracy. Nevertheless, if one were willing to relax exactness requirements, the resulting linear systems could alternatively be solved using iterative methods, such as the Conjugate Gradient (CG) or GMRES algorithms. Iterative solvers offer greater flexibility with respect to problem size, as they require significantly less random access memory than direct solvers as they rely primarily on sparse matrix–vector products. As a consequence, they allow the use of meshes with a larger number of elements, at the expense of introducing a controllable error prescribed by convergence tolerance.

The script for running this problem can be found in Listing A.1.

7.2.2 Revisiting Poiseuille flow through lens-shaped and figure-eight ducts

For this work, we solved the Poiseuille problem, subject to the no-slip boundary condition at the walls, now considering circular lens and figure-eight geometries. These domains are generated from the intersection of two circular disks with equal radius, where the relative distance between the disk centers governs the shape of the cross section. For small separations, the intersection yields a convex lens-shaped domain bounded by circular arcs, in contrast to the parabolic lens geometry analyzed in our previous work. In a limiting configuration, the geometry reduces to a circular cross section, and for larger separations, the domain transitions into a figure-eight shape, consisting of two lobes connected through a narrow region.

As in the previous cases, quadratic finite elements (P2) were employed and the mesh is

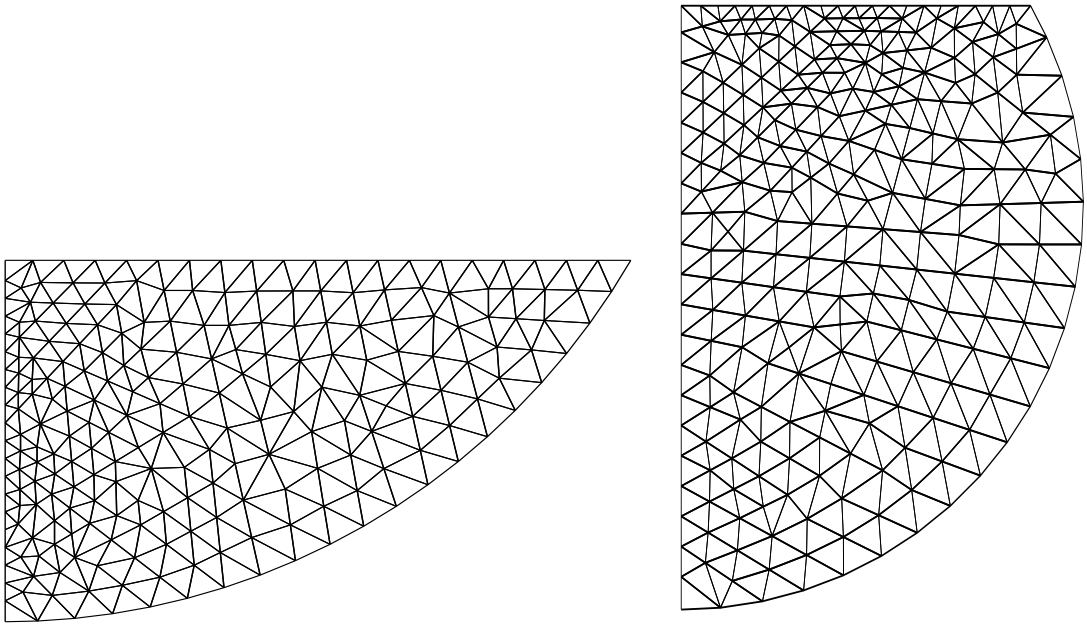

(a) Mesh for $\alpha = \pi/3$.

(b) Mesh for $\alpha = 2\pi/3$.

Figure 7.1: Finite element meshes generated in FreeFEM.

displayed on Figure 7.1. However, these geometries introduce a clear numerical difficulty related to the presence of sharp geometric corners, points formed at the intersection of the circular boundaries in the figure–eight configuration. At these locations, the boundary regularity deteriorates, which adversely affects both mesh generation and the accuracy of the numerical solution, even when higher-order elements are used.

To mitigate this issue, we exploited the inherent symmetry of the domain and solved the problem only on a single quadrant. Symmetry boundary conditions were imposed along both the coordinate axes,

$$\frac{\partial u}{\partial x} = 0 \quad \text{and} \quad \frac{\partial u}{\partial y} = 0, \tag{7.3}$$

This approach significantly reduces the influence of the geometric singularities on the mesh quality and enhances the robustness of the finite element solution.

As shown in Figure 4.4, the Poiseuille number exhibits a markedly different behavior before and after $\frac{\pi}{2}$. This change is directly linked to the geometric transition of the cross section, evolving from a lens to a circular shape and subsequently to a figure-eight geometry. In the latter regime, the so-called dip phenomenon arises, characterized by the presence of two distinct local maxima of the velocity field, each located within one of the lobes. The finite element method captures this behavior with high accuracy, and both the maximum velocity values and their respective locations were verified against the corresponding analytical solution.

The script associated with this problem is shown in Listing A.2.

7.2.3 Startup of Poiseuille flow in triangular ducts

In this chapter, we now turn our attention to the transient Poiseuille flow in two well-defined duct geometries that are particularly favorable for triangular mesh generation, the hemi-equilateral and the right-angled isosceles triangle (Fig. 7.2). In contrast to the steady configurations analyzed previously, the present study focuses on the transient Poiseuille problem given in Eq. 2.34. As a result, the velocity field is time-dependent, producing a distinct solution at each time step. A nondimensional time step of $\Delta t \approx 10^{-3}$ was adopted, and temporal variations become practically negligible after an initial transient, for $t \approx 0.2$.

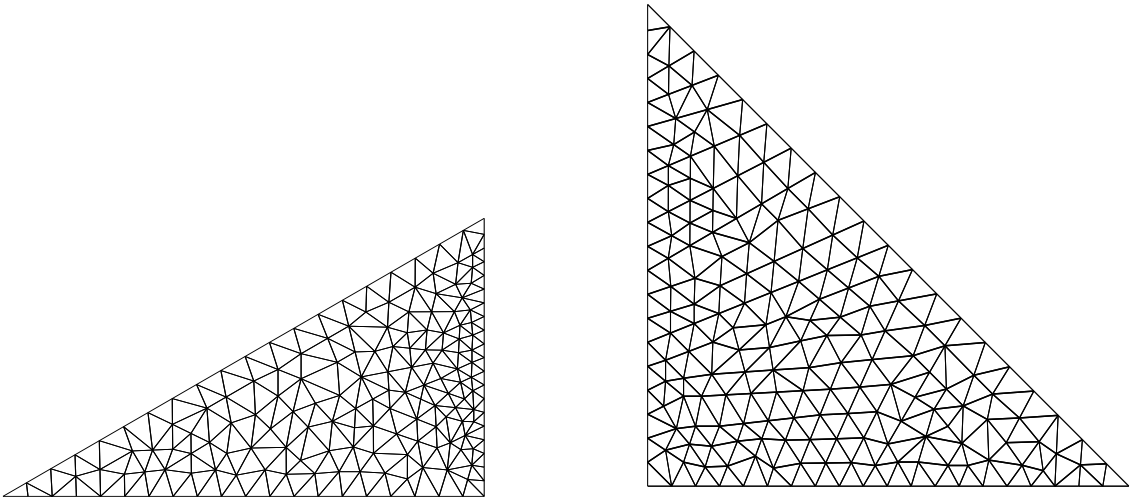

(a) Hemi-equilateral triangle mesh.

(b) Right-angled isosceles triangle mesh.

Figure 7.2: Triangular meshes generated in FreeFEM.

In addition to the velocity field, we compute the wall shear stress, defined as the mean normal derivative of the velocity along the boundary,

$$\tau_w = -\frac{1}{P} \oint_{\partial\Omega} \left(\frac{\partial u}{\partial x} n_x + \frac{\partial u}{\partial y} n_y \right) \mathrm{d}s \tag{7.4}$$

where $\boldsymbol{n} = (n_x, n_y)$ denotes the outward unit normal vector and P is the wetted perimeter. In the numerical implementation, this expression is evaluated as

```
real shear = int1d(Th,1)( -(dx(u)*N.x + dy(u)*N.y) )/P;.
```

Here, `dx(u)` and `dy(u)` represent the spatial derivatives of the velocity field, projected onto the corresponding components of the outward normal vector, and integrated along the triangular boundary segment identified by the prescribed boundary label. It is worth emphasizing that, for boundary segments parallel to the coordinate axes, one of the normal components vanishes, and consequently the associated contribution to the shear stress is zero. In the triangular case, only one boundary segment has a normal vector with both nonzero components, due to the chosen orientation of the geometry.

An additional numerical aspect concerns the choice of finite elements. Since quadratic

(P2) elements are employed, the velocity gradient along the boundary is piecewise linear, ensuring continuity of the shear-stress field. If linear (P1) elements were used instead, the derivative would be piecewise constant, leading to discontinuities in the shear-stress distribution and a characteristic staircase-like profile.

The numerical implementation is provided in Listing A.3.

7.2.4 Revisiting Darcy–Brinkman flow through an elliptic tube

We conclude the analysis by considering a different governing equation, specifically a nonhomogeneous Helmholtz equation arising from the addition of a linear drag term in the Darcy–Brinkman model. In this problem, the computational domain is elliptical and defined by a geometric aspect factor b.

To solve this problem, a coordinate transformation was employed to map the elliptical domain expressed in Cartesian coordinates (x, y) onto a rectangular domain in the Elliptic coordinate system (ξ, θ). With this change, the governing equation of the problem becomes

$$\frac{2}{c^2(\cosh 2\xi - \cos 2\theta)}\left(\frac{\partial^2 w}{\partial \xi^2} + \frac{\partial^2 w}{\partial \theta^2}\right) - s^2 w = -1. \tag{7.5}$$

This transformation enables the construction of a structured triangular mesh with a well-controlled number of elements, as illustrated in Figure 7.3. In addition, domain symmetries were again exploited. In the elliptic coordinate system, these symmetries are represented by the derivatives

$$\left.\frac{\partial w}{\partial \xi}\right|_{\xi=0} = \left.\frac{\partial w}{\partial \theta}\right|_{\theta=0} = \left.\frac{\partial w}{\partial \theta}\right|_{\theta=\frac{\pi}{2}} = 0. \tag{7.6}$$

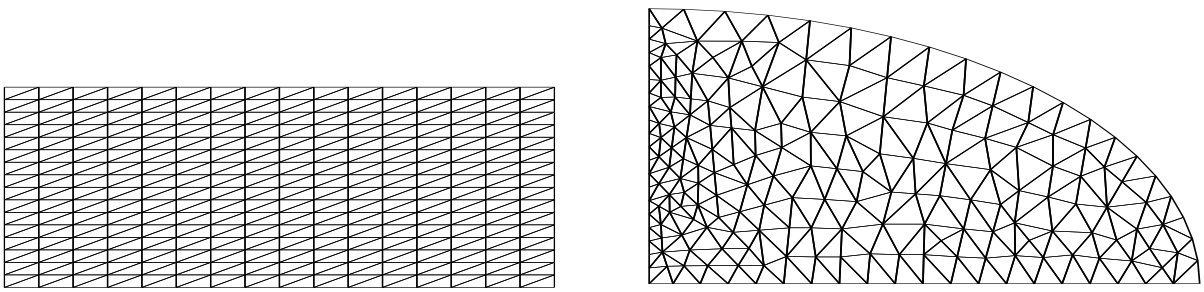

(a) Structured mesh (elliptic coordinates). (b) Unstructured mesh (Cartesian coordinates).

Figure 7.3: Comparison between meshes represented in different coordinate systems.

This strategy allows us to circumvent the plug-like velocity behavior characteristic of elliptical geometries, which would otherwise require a very fine mesh to be accurately resolved.

Despite these advantages, the coordinate transformation introduces a Jacobian that must

be consistently accounted for in the computation of integral quantities, such as the volumetric flow rate. This Jacobian explicitly depends on both Cartesian coordinates x and y and therefore this spatial dependence prevents the Jacobian from being factored out of the integrals and requires its pointwise evaluation within the numerical quadrature.

To further enhance the accuracy of the numerical results of the Poiseuille number, a grid study was conducted using Richardson extrapolation [182]. Three structured meshes were generated with increasing refinement levels, consisting of 128×128 (M_3), 256×256 (M_2), and 512×512 (M_1) elements, yielding a constant refinement ratio of $r = 2$.

The Poiseuille number (Po), which is the primary quantity of interest, was computed for each mesh configuration. Assuming the solutions are in the asymptotic range, the grid-independent value (Po_{ext}) was estimated using the solutions from the two finest meshes (M_1 and M_2) according to the extrapolation formula

$$Po_{\text{ext}} = Po_1 + \frac{Po_1 - Po_2}{r^p - 1}, \tag{7.7}$$

where Po_1 and Po_2 correspond to the values obtained on the 512×512 and 256×256 meshes, respectively, and p represents the order of convergence of the numerical scheme. This procedure yielded results with accuracy up to eight decimal places, which were subsequently compared against the analytical solution.

The numerical implementation is provided in Listing A.4.

Chapter 8

Conclusion

This dissertation investigated the finite element modelling of different configurations of internal flows in various duct geometries. The governing equations were formulated as a Poisson equation for the axial velocity field, with an unsteady contribution or a Brinkman correction depending on the problem and solved using a Galerkin finite element approach.

A complete variational formulation was derived and discretized in space using continuous triangular elements. The numerical implementation was carried out in the FreeFEM environment, which allowed direct construction of geometries borders, automatic mesh generation based on Delaunay–Voronoi triangulation, and easy boundary conditions implementation. The implicit Euler scheme was adopted for time integration, providing stable convergence towards the steady-state solution.

The numerical results demonstrated that the proposed formulation accurately captures the velocity field locally and globally as well as its transient evolution. Mesh refinement analysis reaffirmed the convergence of the method, and the computed integral quantities with quadrature, such as volumetric flow rate and Poiseuille number, showed consistent behaviour with reference solutions. The finite element method was proved to be particularly advantageous for handling geometries defined by implicit equations or parametric boundaries, which are difficult to treat using structured grid approaches.

The finite element methodology outlined in this section underpins all investigations presented in this dissertation. A brief summary of the contributions of each paper is summarized as:

Chapter 3

- Development of new analytical and numerical solutions for steady Poiseuille flow in parabolic segment and parabolic lens-shaped ducts, geometries that are previously unexplored in the literature.
- Derivation of asymptotic solutions using perturbation methods for small aspect ratios, providing explicit approximate expressions for the velocity field, volumetric flow rate,

and friction factor–Reynolds number product in the thin-duct limit.

- Construction of exact analytical solutions in parabolic coordinates for a special case of intermediate aspect ratio, using a change of coordinates that makes the application of separation of variables feasible.
- Application of the Maclaine–Cross approximate formula to determine the limiting behaviour of the friction factor–Reynolds number product for large aspect ratios.
- Numerical investigation using the finite elements method for all aspect ratios, including a analysis of mesh convergence and validation against analytical and asymptotic solutions.
- Identification and characterization of the monotonic and non-monotonic dependence of the volumetric flow rate and friction factor–Reynolds number product on the aspect ratio for both parabolic segment and lens-shaped ducts.
- Construction of polynomial correlations for the friction factor–Reynolds number product in both the small and large aspect ratio limits, achieving relative errors below practical thresholds.
- Extension of the analytical development and results beyond the fluid mechanics framework, highlighting its applicability to a broader class of physical problems governed by the Poisson equation with homogeneous Dirichlet boundary conditions.

Chapter 4

- An explicit analytical formulation is derived for the volumetric flow rate.
- Closed-form values of the Poiseuille number are obtained at specific geometric angles, including the figure-eight configuration.
- A general analytical representation of the Poiseuille number is established, together with an efficient computational strategy based on a trigamma-series expansion which demonstrated to be rapidly convergent.
- A full-domain formulation is developed to quantitatively characterize the existence and transition of the figure-eight regime, allowing a description of the flow behavior over the entire parameter range.
- A uniform $6/6$ Padé approximant is constructed to provide an accurate global approximation of the Poiseuille number, achieving a maximum relative error of approximately 0.012% over the full parameter domain.

Chapter 5

- Derivation of new exact analytical solutions for the transient Poiseuille flow in two triangular ducts not previously treated in the literature: the hemi-equilateral triangle and the right-angled isosceles triangle.
- Application of the eigenfunction superposition method to non-separable geometries, enabling the construction of a series representation of transient solutions in triangular domains that admit complete trigonometric eigenfunctions under homogeneous Dirichlet boundary conditions.
- Explicit determination of wall shear stress distributions as a function of time along each side of the triangular cross sections, together with analytical expressions for the mean wall shear stress in the steady-state limit.
- Validation of the steady solutions by comparison with reference results available in the literature, confirming the accuracy of the proposed formulations.
- Completion of the family of triangular duct geometries admitting exact transient solutions based on trigonometric eigenfunctions, complementing the previously known equilateral triangle case.

Chapter 6

- Establishment of a new formulation that allows the direct computation of the volumetric flow rate and the Poiseuille number for Darcy–Brinkman flow in elliptic tubes, filling a gap in the available analytical results.
- Identification and correction of a typographical inconsistency in the classical solution for the elliptic-tube velocity field, ensuring the mathematical consistency of the previous analytical formulation.
- Recovery of canonical limiting cases, including the clear fluid Poiseuille problem solution and the circular Darcy–Brinkman tube.
- High-precision evaluation of the analytical series using symbolic–numerical computation, addressing the numerical stiffness of Mathieu functions and ensuring convergence across the entire range of porous-medium parameters and aspect ratios.
- Independent validation of the analytical results through finite element simulations with Richardson extrapolation and due mesh convergence, achieving agreement at the level of up to ten significant digits.
- Documentation of a high-accuracy benchmark solution for the verification of numerical solvers and asymptotic approximations in Helmholtz-type equations with homogeneous Dirichlet boundary conditions.

8.1 Future work

The methodology developed in this dissertation provides a flexible basis for several extensions and complementary investigations. Some of the directions outlined below are already being pursued as part of ongoing work:

- **Couette and Rayleigh–Stokes flows.** The treatment of the pure Couette flow in non-circular geometries, such as the isosceles triangular duct, constitutes a natural extension of the present study. In addition, the transient response of a viscous fluid subjected to impulsive boundary motion, the Rayleigh–Stokes problem, can be investigated using the same Freefem script by simply modifying a boundary condition and the source term. These classical problems models phenomena encountered in micro-electromechanical systems (MEMS) startup flows, industrial dip-coating processes and extruders [187, 188, 175].

- **Non-Newtonian fluid models.** The extension of the present transient formulation to non-Newtonian fluids represents an important step toward practical applications. By introducing constitutive models such as the Maxwell and Oldroyd-type fluids, its possible to study elastic effects and additional time scales, leading to a more complex transient dynamics and modified velocity distributions. Regarding industrial applications, specifically, the Maxwell fluid is widely used to predict the behavior of molten plastics in large-amplitude oscillatory shear flow [189, 190]

- **Heat transfer analysis.** The coupling of the momentum equation with the energy equation enables the investigation of forced convection in non-circular ducts. This extension allows for the solution of the thermal boundary value problems classified by Shah and London [33]. Specifically, it is possible to address two heat flux cases (H_1 and H_2 conditions). The combined analysis of velocity and temperature fields is essential for determining the Nusselt number. This parameter is relevant to the design of compact heat exchangers and thermal management in electronic systems. It is particularly applicable to modeling phase-change components, such as evaporators and condensers, as well as in solar thermal collectors [35, 191, 192].

- **Slip-flow regimes and partial slip boundary conditions in ducts.** The extension of the present formulation to slip-flow regimes allows the investigation of rarefied or micro-scale flows in which the no-slip boundary condition is no longer valid. By incorporating partial slip or Navier slip boundary conditions at the duct walls, it becomes possible to capture the velocity jump at the fluid-solid interface. Accurate modeling of this regime is critical in modern engineering applications, such as the design of hard disk drives, where the lubrication film thickness is on the order of nanometers. Furthermore, slip effects play a dominant role in gas transport through nanoporous shale reservoirs and in the thermal management of micro–electromechanical systems

(MEMS), where velocity discontinuity at the wall significantly alters the pressure drop and mass flow rate compared to continuum predictions [193, 194, 195].

- **Three-dimensional extensions and multidisciplinary applications.** Although the present work focuses on two-dimensional cross-sectional formulations, the methodology can be naturally extended to three-dimensional configurations. Furthermore, the underlying mathematical structure of the Poisson equation governs fundamental phenomena beyond fluid mechanics. Consequently, the numerical solutions developed can be directly mapped to other physical domains, such as determining electrostatic potential distributions in dielectrics, modeling steady-state diffusion with reaction terms, and solving gravitational potential problems [105], thereby broadening the applicability of the work.

Bibliography

[1] AMANI, M.; AMERI, M.; KASAEIAN, A. The experimental study of convection heat transfer characteristics and pressure drop of magnetite nanofluid in a porous metal foam tube. *Transport in Porous Media*, v. 116, p. 959–974, 2017.

[2] DHAHBI, A. B. et al. A two-dimensional mathematical model of heat propagation equations and their significance for soil temperature. *Symmetry*, v. 11, n. 4, 2019. ISSN 2073-8994. Disponível em: <https://www.mdpi.com/2073-8994/11/4/478>.

[3] WANG, C. Y. Flow through a lens-shaped duct. *Journal of Applied Mechanics*, v. 75, n. 3, p. 034503, 05 2008. ISSN 0021-8936.

[4] MUZYCHKA, Y. S.; YOVANOVICH, M. M. Pressure drop in laminar developing flow in noncircular ducts: A scaling and modeling approach. *Journal of Fluids Engineering*, v. 131, n. 11, p. 111105, 10 2009. ISSN 0098-2202. Disponível em: <https://doi.org/10.1115/1.4000377>.

[5] SARVIHA, A.; BARATI, E. Piezoelectric energy harvester for scavenging steady internal flow energy: a numerical investigation. *Journal of the Brazilian Society of Mechanical Sciences and Engineering*, Springer, v. 45, n. 8, p. 398, 2023.

[6] MCKETTA, J. J. J. *Encyclopedia of Chemical Processing and Design: Volume 37 – Pipeline Flow: Basics to Piping Design*. [S.l.]: CRC Press, 1976.

[7] KRZACZEK, M.; FLORCZUK, J.; TEJCHMAN, J. Improved energy management technique in pipe-embedded wall heating/cooling system in residential buildings. *Applied Energy*, Elsevier, v. 254, p. 113711, 2019.

[8] HERRÁN-GONZÁLEZ, A. et al. Modeling and simulation of a gas distribution pipeline network. *Applied Mathematical Modelling*, Elsevier, v. 33, n. 3, p. 1584–1600, 2009.

[9] KAYNAKLI, O. Economic thermal insulation thickness for pipes and ducts: A review study. *Renewable and Sustainable Energy Reviews*, v. 30, p. 184–194, 2014. ISSN 1364-0321. Disponível em: <https://www.sciencedirect.com/science/article/pii/S1364032113006977>.

[10] APAK, M. Y. et al. Applications of utility tunnels for natural gas pipelines. *Tunnelling and Underground Space Technology*, v. 122, p. 104243, 2022. ISSN 0886-7798. Disponível em: <https://www.sciencedirect.com/science/article/pii/S088677982100434X>.

[11] ÖMüR, C. et al. Incorporation of manufacturing constraints into an algorithm for the determination of maximum heat transport capacity of extruded axially grooved heat pipes. *International Journal of Thermal Sciences*, v. 123, p. 181–190, 2018. ISSN 1290-0729. Disponível em: <https://www.sciencedirect.com/science/article/pii/S1290072917307329>.

[12] ENFINGER, K. L. Working with combined sewers: Geometric and hydraulic elements of egg-shaped sewers. In: ____. *Pipelines 2024*. [s.n.], 2024. p. 282–290. Disponível em: <https://ascelibrary.org/doi/abs/10.1061/9780784485583.030>.

[13] MÂRZA, C.; CORSIUC, G.; GRAUR, A.-M. Study regarding the geometry of some pieces used in flat-oval ducts. *Journal of Industrial Design and Engineering Graphics*, v. 17, n. 2, p. 41–46, 2022.

[14] MALOZYOMOV, B. V. et al. Overview of methods for enhanced oil recovery from conventional and unconventional reservoirs. *Energies*, MDPI, v. 16, n. 13, p. 4907, 2023.

[15] WELSH, W. D. *Groundwater Balance Modelling with Darcy's Law*. Tese (PhD thesis) — Australian National University, 2007. Disponível em: <http://hdl.handle.net/1885/48015>.

[16] HO, C. K.; WEBB, S. W. *Gas transport in porous media*. [S.l.]: Springer, 2006.

[17] MACINI, P.; MESINI, E. Darcy's law from water to the petroleum industry: When and who? In: ____. *Henry P. G. Darcy and Other Pioneers in Hydraulics*. [S.l.: s.n.]. p. 78–89.

[18] KENDOUCI, M. A. et al. Simulation of water filtration in porous zone based on darcy's law. *Energy Procedia*, Elsevier, v. 36, p. 163–168, 2013.

[19] DORHJIE, D. B. et al. Deviation from darcy law in porous media due to reverse osmosis: pore-scale approach. *Energies*, MDPI, v. 15, n. 18, p. 6656, 2022.

[20] CHRISTENSEN, D. A. *Introduction to Biomedical Engineering: Biomechanics and Bioelectricity*. [S.l.]: Morgan & Claypool Publishers, 2009.

[21] GALAL, A. M. et al. Design the modeling of synovial fluid with two viscosity models on a surface: Biomedical engineering applications. *Results in Engineering*, Elsevier, p. 108158, 2025.

[22] FISH, J.; BELYTSCHKO, T. *A first course in finite elements*. [S.l.]: Wiley New York, 2007.

[23] LOGAN, D. L. *A first course in the finite element method*. [S.l.]: Thomson, 2011.

[24] MELOSH, R. J. Structural analysis of solids. *Journal of the Structural Division*, v. 89, p. 205–248, 1963. Disponível em: <https://api.semanticscholar.org/CorpusID:118357372>.

[25] REDDY, J. N. *An Introduction to nonlinear finite element analysis: with applications to heat transfer, fluid mechanics, and solid mechanics*. 2. ed. ed. [S.l.]: Oxford University Press, 2015. ISBN 9780191789557; 0191789550; 9780199641758; 0199641757.

[26] SILVA, V. C. et al. Poiseuille flow through parabolic segment and lens-shaped ducts. *IMA Journal of Applied Mathematics*, v. 90, n. 4, p. 347–369, 2025.

[27] SILVA, V. C.; LOPES, A. B. Revisiting poiseuille flow through lens-shaped and figure-eight ducts. *Mechanics Research Communications*, v. 150, p. 104570, 2025.

[28] SILVA, V. C.; LUSTOSA, B. P.; LOPES, A. B. Startup of poiseuille flow in triangular ducts. *Zeitschrift für Angewandte Mathematik und Physik*, v. 76, n. 6, p. 241, 2025.

[29] LOPES, A.; FAR, M. E. F.; SILVA, V. C. Revisiting darcy–brinkman flow through an elliptic tube. *Transport in Porous Media*, v. 153, n. 1, p. 13, 2025.

[30] POISEUILLE, J. L. *Recherches expérimentales sur le mouvement des liquides dans les tubes de très-petits diamètres*. [S.l.]: Imprimerie Royale, 1844.

[31] HAGEN, G. Ueber die bewegung des wassers in engen cylindrischen röhren. *Annalen der Physik*, Wiley Online Library, v. 122, n. 3, p. 423–442, 1839.

[32] SHAH, R. K.; LONDON, A. L. *Laminar Flow Forced Convection in Ducts: A Source Book for Compact Heat Exchanger Analytical Data*. [S.l.]: Academic Press, 1976.

[33] SHAH, R. K.; LONDON, A. L. *Laminar Flow Forced Convection in Ducts: A Source Book for Compact Heat Exchanger Analytical Data*. [S.l.]: Academic Press, 1978.

[34] WANG, C. Exact solutions of the steady-state Navier-Stokes equations. *Annual Review of Fluid Mechanics*, v. 23, n. 1, p. 159–177, 1991.

[35] WANG, C. Y. H1 and h2 forced convection in semi-elliptic ducts. *Journal of Heat Transfer*, v. 144, n. 10, p. 104501, 08 2022. ISSN 0022-1481. Disponível em: <https://doi.org/10.1115/1.4055147>.

[36] SAHA, S. K.; AGRAWAL, A.; SONI, Y. Heat transfer characterization of rhombic microchannel for h1 and h2 boundary conditions. *International Journal of Thermal Sciences*, Elsevier, v. 111, p. 223–233, 2017.

[37] MORINI, G. L. Laminar-to-turbulent flow transition in microchannels. *Microscale Thermophysical Engineering*, v. 8, n. 1, p. 15–30, 2004.

[38] WANG, C. Y. H1 and h2 forced convection in semi-elliptic ducts. *Journal of Heat Transfer*, v. 144, n. 10, p. 104501, 08 2022. ISSN 0022-1481. Disponível em: <https://doi.org/10.1115/1.4055147>.

[39] KARNIADAKIS, G. E.; BESKOK, A.; ALURU, N. *Microflows and Nanoflows: Fundamentals and Simulation*. [S.l.]: Springer, 2005.

[40] AZIZI, Y.; FATTAHI, M.; SADEGHI, A. Fluid flow and heat transfer in two-segmented microchannels within the slip flow regime. *Thermal Science and Engineering Progress*, Elsevier, v. 63, p. 103751, 2025.

[41] SI, X. et al. The periodic secondary flow of oldroyd-b fluids driven by direct electric field in a rectangular curved channel. *Physics of Fluids*, AIP Publishing, v. 35, n. 3, 2023.

[42] FAROOQ, A. et al. On the flow of mhd generalized maxwell fluid via porous rectangular duct. *Open Physics*, De Gruyter, v. 18, n. 1, p. 989–1002, 2020.

[43] WANG, W.; DU, B.; JIA, Y. Numerical study of flow and heat transfer for pulsating flow in a square duct with ribs. In: BEGEL HOUSE INC. *International Heat Transfer Conference Digital Library*. [S.l.], 2018.

[44] NAZAR, M. et al. Flow through an oscillating rectangular duct for generalized maxwell fluid with fractional derivatives. *Communications in Nonlinear Science and Numerical Simulation*, v. 17, n. 8, p. 3219–3234, 2012. ISSN 1007-5704. Disponível em: <https://www.sciencedirect.com/science/article/pii/S100757041100551X>.

[45] SUN, X.; WANG, S.; ZHAO, M. Oscillatory flow of maxwell fluid in a tube of isosceles right triangular cross section. *Physics of Fluids*, v. 31, n. 12, p. 123101, 12 2019. ISSN 1070-6631. Disponível em: <https://doi.org/10.1063/1.5128764>.

[46] NADEEM, S. et al. The rayleigh stokes problem for rectangular pipe in maxwell and second grade fluid. *Meccanica*, Springer, v. 43, n. 5, p. 495–504, 2008.

[47] KAHSHAN, M. et al. Darcy-brinkman flow of a viscous fluid through a porous duct: Application in blood filtration process. *Journal of the Taiwan Institute of Chemical Engineers*, v. 117, p. 223–230, 2020. ISSN 1876-1070. Disponível em: <https://www.sciencedirect.com/science/article/pii/S1876107020303898>.

[48] WANG, C. The starting flow in ducts filled with a darcy-brinkman medium. *Transport in porous media*, Springer, v. 75, n. 1, p. 55–62, 2008.

[49] Neves, R. A. *Escoamento laminar em dutos circulares com incrustações: Análise do perfil de velocidade e fator de atrito*. Trabalho de Conclusão de Curso (Licenciatura em Física) — Universidade Estadual da Paraíba, 2020.

[50] WANG, Y. Solutions for elastic torsion problems involving prismatic bars of generalized cardioid cross-section. *International Journal of Mechanical Engineering Education*, SAGE Publications Sage UK: London, England, v. 37, n. 3, p. 175–180, 2009.

[51] SALIH, A. A. *Finite Element Method*. Thiruvananthapuram, India, 2012.

[52] KALIAKIN, V. N. *Introduction to approximate solution techniques, numerical modeling, and finite element methods*. [S.l.]: CRC Press, 2018.

[53] JOHNSON, C. *Numerical solution of partial differential equations by the finite element method*. [S.l.]: Courier Corporation, 2009.

[54] İNç, M.; BILDIK, N.; BULUT, H. A comparison of numerical ode solvers based on euler methods. *Mathematical and Computational Applications*, v. 3, n. 3, p. 153–159, 1998. ISSN 2297-8747. Disponível em: <https://www.mdpi.com/2297-8747/3/3/153>.

[55] PETERESON, M. Two-dimensional finite element simulation of the thermal problem at railway block braking. *Proceedings of the Institution of Mechanical Engineers, Part C: Journal of Mechanical Engineering Science*, SAGE Publications Sage UK: London, England, v. 216, n. 3, p. 259–273, 2002.

[56] RASOULI, E.; FRICKE, E.; NARAYANAN, V. High efficiency 3-D printed microchannel polymer heat exchangers for air conditioning applications. *Science and Technology for the Built Environment*, Taylor & Francis, v. 28, n. 3, p. 289–306, 2022. Disponível em: <https://doi.org/10.1080/23744731.2022.2026693>.

[57] ANDRADE, I. R. de et al. Multi-objective numerical analysis of horizontal rectilinear earth–air heat exchangers with elliptical cross section using constructal design and TOPSIS. *Fluids*, v. 9, n. 11, 2024. ISSN 2311-5521. Disponível em: <https://www.mdpi.com/2311-5521/9/11/257>.

[58] HAQUE, M. E.; HOSSAIN, M. S.; ALI, H. M. Laminar forced convection heat transfer of nanofluids inside non-circular ducts: A review. *Powder Technology*, v. 378, p. 808–830, 2021. ISSN 0032-5910. Disponível em: <https://www.sciencedirect.com/science/article/pii/S0032591020309918>.

[59] POLASCHEGG, H. D. Pressure drops in cannulas for hemodialysis. *The International Journal of Artificial Organs*, v. 24, n. 9, p. 614–623, 2001. PMID: 11693417. Disponível em: <https://doi.org/10.1177/039139880102400908>.

[60] COWARD, A. V.; PAPAGEORGIOU, D. T. Stability of oscillatory two-phase Couette flow. *IMA Journal of Applied Mathematics*, v. 53, n. 1, p. 75–93, 01 1994. ISSN 0272-4960. Disponível em: <https://doi.org/10.1093/imamat/53.1.75>.

[61] ABEDI, B. et al. Startup flow of gelled waxy crude oils in pipelines: The role of volume shrinkage. *Fuel*, v. 288, p. 119726, 2021.

[62] AWOJOYOGBE, O. B. et al. Mathematical models of real geometrical factors in restricted blood vessels for the analysis of CAD (Coronary Artery Diseases) using Legendre, Boubaker and Bessel polynomials. *Journal of Medical Systems*, v. 35, p. 1513–1520, 2011.

[63] WANG, C. Y. Exact solutions of the steady-state Navier-Stokes equations. *Annual Review of Fluid Mechanics*, v. 23, p. 159–177, 1991.

[64] WILLATZEN, M.; VOON, L. C. L. Y. *Separable boundary-value problems in Physics*. [S.l.]: John Wiley & Sons, 2011.

[65] PROUDMAN, J. Notes on the motion of viscous liquids in channels. *The London, Edinburgh, and Dublin Philosophical Magazine and Journal of Science*, v. 28, p. 30–36, 1914.

[66] GUO, J.; MERONEY, R. Theoretical solution for laminar flow in partially-filled pipes. *Journal of Hydraulic Research*, v. 51, p. 408–416, 2013.

[67] FULLARD, L. A.; WAKE, G. C. An analytical series solution to the steady laminar flow of a Newtonian fluid in a partially filled pipe, including the velocity distribution and the dip phenomenon. *IMA Journal of Applied Mathematics*, v. 80, n. 6, p. 1890–1901, 2015. ISSN 0272-4960. Disponível em: <https://doi.org/10.1093/imamat/hxv025>.

[68] SOKOLNIKOFF, I. S.; SOKOLNIKOFF, E. S. Torsion of regions bounded by circular arcs. *Bulletin of the American Mathematical Society*, p. 384–387, 1938.

[69] HAY, G. E. The method of images applied to the problem of torsion. *Proceedings of the London Mathematical Society*, s2-45, p. 382–397, 1939.

[70] FRANCů, J.; NOVáčKOVá, P.; JANíčEK, P. Torsion of a non-circular bar. *Engineering Mechanics*, v. 19, p. 45–60, 2012.

[71] SETH, B. R. Motion of a liquid contained in rotating cylinders of triangular cross-section. *The Quarterly Journal of Mathematics*, os-5, p. 161–171, 1934.

[72] LAMB, H. *Hydrodynamics*. 5th. ed. Cambridge: University Press, 1924.

[73] PIERCY, N. A. V.; HOOPER, M. S.; WINNY, H. F. Viscous flow through pipes with cores. *The London, Edinburgh, and Dublin Philosophical Magazine and Journal of Science*, Taylor & Francis, v. 15, n. 99, p. 647–676, 1933. Disponível em: <https://doi.org/10.1080/14786443309462212>.

[74] ALASSAR, R. S.; ABUSHOSHAH, M. Hagen-Poiseuille flow in semi-elliptic microchannels. *Journal of Fluids Engineering*, v. 134, p. 124502, 2012.

[75] WANG, C. Y. On viscous flow in semi-elliptic ducts. *Journal of Fluids Engineering*, v. 137, 2015.

[76] ALASSAR, R. S. Fully developed forced convection through semi-elliptic ducts. *Applied Mathematics and Mechanics*, Springer, v. 37, p. 37–44, 2016.

[77] LOPES, A. B.; SIQUEIRA, I. R. Couette-Poiseuille flow in semi-elliptic channels. *Journal of Fluids Engineering*, v. 144, p. 101302, 2022.

[78] WANG, C. Y. H1 and H2 forced convection in semi-elliptic ducts. *Journal of Heat Transfer*, American Society of Mechanical Engineers, v. 144, n. 10, p. 104501, 2022.

[79] KUNDU, K.; SARKAR, U. K. Analytical and numerical investigation of Poiseuille flow through semi-elliptic annulus. *Physics of Fluids*, AIP Publishing, v. 34, n. 8, p. 083603, 2022.

[80] BACELAR, M. D. et al. Hagen–Poiseuille flow in a quarter-elliptic tube. *Fluids*, v. 8, p. 247, 2023.

[81] BOUSSINESQ, J. Mémoire sur l'influence des frottements dans les mouvements réguliers des fluids. *Journal de Mathématiques Pures et Appliquées*, v. 13, n. 2, p. 377–424, 1868.

[82] STOKES, G. G. On the theories of the internal friction of fluids in motion, and of the equilibrium and motion of elastic solids. *Transactions of the Cambridge Philosophical Society*, v. 8, p. 287–341, 1845.

[83] ECKERT, E. R. G.; JR, F. I. Flow in corners of passages with noncircular cross sections. *Transactions of the American Society of Mechanical Engineers*, v. 78, n. 4, p. 709–718, 2022. ISSN 0097-6822. Disponível em: <https://doi.org/10.1115/1.4013793>.

[84] KYRITSI-YIALLOUROU, S.; GEORGIOU, G. Newtonian Poiseuille flow in ducts of annular-sector cross-sections with Navier slip. *European Journal of Mechanics - B/Fluids*, v. 72, p. 87–102, 2018. ISSN 0997-7546. Disponível em: <https://www.sciencedirect.com/science/article/pii/S0997754618302279>.

[85] LOPES, A. B.; ALASSAR, R. S. Comment on "Newtonian Poiseuille flow in ducts of annular-sector cross-sections with Navier slip". *European Journal of Mechanics - B/Fluids*, v. 96, p. 105–107, 2022. ISSN 0997-7546. Disponível em: <https://www.sciencedirect.com/science/article/pii/S0997754622001017>.

[86] BOUSSINESQ, J. Mémoire sur l'influence des frottements dans les mouvements réguliers des fluides. *Journal de Mathématiques Pures et Appliquées*, v. 13, p. 377–438, 1868.

[87] JOG, C. S. *Fluid Mechanics: Foundations and Applications of Mechanics*. 3. ed. [S.l.]: Cambridge University Press, 2015.

[88] MOSHINSKII, A. I. Liquid flow in prismatic channels resting on a parabolic contour. *Journal of Engineering Physics and Thermophysics*, Springer, p. 1–11, 2024.

[89] Lew Yan Voon, L. C.; WILLATZEN, M. Helmholtz equation in parabolic rotational coordinates: application to wave problems in quantum mechanics and acoustics. *Mathematics and Computers in Simulation*, v. 65, n. 4, p. 337–349, 2004. ISSN 0378-4754. Wave Phenomena in Physics and Engineering: New Models, Algorithms, and Applications. Disponível em: <https://www.sciencedirect.com/science/article/pii/S0378475404000217>.

[90] JANNUSSIS, A. D.; LEODARIS, A. D.; BRODIMAS, G. N. Study of the Stark and Zeeman effects in parabolic coordinates. *Physics Letters A*, v. 71, n. 2, p. 205–207, 1979. ISSN 0375-9601. Disponível em: <https://www.sciencedirect.com/science/article/pii/0375960179901634>.

[91] GOLIKOV, Y. K.; SOLOV'EV, K. V. Electrostatic ion traps with separation of variables in parabolic coordinates. *Technical Physics Letters*, v. 36, p. 333–336, 2010.

[92] ZIRAKASHVILI, N. Exact solution of some exterior boundary value problems of elasticity in parabolic coordinates. *Mathematics and Mechanics of Solids*, v. 23, n. 6, p. 929–943, 2018.

[93] NUNEZ-FERNANDEZ, Y.; TRALLERO-GINER, C.; BUCHLEITNER, A. Liquid surface waves in parabolic tanks. *Physics of Fluids*, AIP Publishing, v. 20, n. 11, 2008.

[94] KACIMOV, A. R.; OBNOSOV, Y. V. Steady water flow around parabolic cavities and through parabolic inclusions in unsaturated and saturated soils. *Journal of Hydrology*, v. 238, n. 1, p. 65–77, 2000. ISSN 0022-1694. Disponível em: <https://www.sciencedirect.com/science/article/pii/S0022169400003103>.

[95] MIRONENKO, A. P.; WILLARDSON, L. S.; JENAB, S. A. Parabolic canal design and analysis. *Journal of Irrigation and Drainage Engineering*, v. 110, n. 2, p. 241–246, 1984.

[96] LAYCOCK, A.; SWAYNE, C.; MARQUES, J. E. J. Pehur high-level canal, NWFP, Pakistan. *Proceedings of the Institution of Civil Engineers, Water Management*, v. 158, n. 3, p. 93–102, 2005.

[97] CHENG, M. S.; COFFMAN, L. S.; CLAR, M. L. Low-impact development hydrologic analysis. In: *Urban Drainage Modeling*. [S.l.: s.n.], 2001. p. 659–681.

[98] WANG, C. Y. Darcy–Brinkman flow in narrow crevices. *Transport in Porous Media*, v. 120, p. 101–113, 2017. Disponível em: <https://doi.org/10.1007/s11242-017-0911-3>.

[99] MACLAINE-CROSS, I. L. An approximate method for calculating heat transfer and pressure drop in ducts with laminar flow. *Journal of Heat Transfer*, v. 91, n. 1, p. 171–173, 02 1969. ISSN 0022-1481.

[100] WANG, C. Y. Flow through a lens-shaped duct. *Journal of Applied Mechanics*, v. 75, n. 3, p. 034503, 05 2008. ISSN 0021-8936.

[101] MOON, P.; SPENCER, D. E. *Field Theory Handbook: Including Coordinate Systems, Differential Equations and Their Solutions*. [S.l.]: Springer, 2012.

[102] HECHT, F. New development in FreeFem++. *Journal of Numerical Mathematics*, v. 20, n. 3-4, p. 251–265, 2012. ISSN 1570-2820. Disponível em: <https://freefem.org/>.

[103] SERRA, L. E. C.; SIQUEIRA, I. R.; LOPES, A. B. A novel lower bound for the friction factor-Reynolds number product in laminar flows of newtonian fluids through singly connected ducts. *Results in Engineering*, v. 21, p. 101948, 2024. ISSN 2590-1230. Disponível em: <https://www.sciencedirect.com/science/article/pii/S2590123024002019>.

[104] SHAH, R. K.; LONDON, A. L. *Laminar flow forced convection in ducts: A source book for compact heat exchanger analytical data*. New York: Academic Press, 1978.

[105] BAZANT, M. Z. Exact solutions and physical analogies for unidirectional flows. *Physical Review Fluids*, APS, v. 1, n. 2, p. 024001, 2016.

[106] TANNER, R. I. Pressure losses in viscometric capillary tubes of slowly varying diameter. *British Journal of Applied Physics*, v. 17, n. 5, p. 663–671, 1966.

[107] MANTON, M. J. Low reynolds number flow in slowly varying axisymmetric tubes. *Journal of Fluid Mechanics*, v. 49, n. 3, p. 451–459, 1971.

[108] KOTORYNSKI, W. P. K. Slowly varying channel flows in three dimensions. *Journal of the Institute of Mathematics and Its Applications*, v. 24, p. 71–80, 1979.

[109] DYKE, M. V. Laminar flow in a meandering channel. *SIAM Journal on Applied Mathematics*, v. 43, n. 4, p. 696–702, 1983.

[110] Van Dyke, M. Slow variations in continuum mechanics. In: WU, T. Y.; HUTCHINSON, J. W. (Ed.). [S.l.]: Elsevier, 1987, (Advances in Applied Mechanics, v. 25). p. 1–45.

[111] NUTTALL, H. Torsion of uniform rods with particular reference to rods of triangular cross section. *Journal of Applied Mechanics*, v. 19, n. 4, p. 554–557, 2021. ISSN 0021-8936.

[112] IRVINE, S.; FULLARD, L. A. The effect of slip on the discharge from partially filled circular and fully filled lens and figure 8 shaped pipes. *Journal of Fluids Engineering*, v. 138, n. 11, p. 111104, 2016.

[113] WANG, C. Y. Darcy–brinkman flow in narrow crevices. *Transport in Porous Media*, v. 120, p. 101–113, 2017.

[114] SILVA, V. C. et al. Poiseuille flow through parabolic segment and lens-shaped ducts. *IMA Journal of Applied Mathematics*, p. hxaf022, 2025.

[115] CARERI, F. et al. Additive manufacturing of heat exchangers in aerospace applications: A review. *Applied Thermal Engineering*, v. 235, p. 121387, 2023.

[116] VIJETHA, K. K. et al. Fabrication of microchannel heat sink using additive manufacturing technology: A review. *Proceedings of the Institution of Mechanical Engineers, Part E: Journal of Process Mechanical Engineering*, 2024.

[117] KETBI, S. A. et al. Simulation based investigation of Nusselt number and Poiseuille number in helical microchannels. *International Journal of Thermofluids*, v. 21, p. 100532, 2024.

[118] BAZANT, M. Z. Exact solutions and physical analogies for unidirectional flows. *Physical Review Fluids*, v. 1, p. 024001, 2016.

[119] WANG, C. Y. Exact solutions of the steady-state Navier–Stokes equations. *Annual Review of Fluid Mechanics*, v. 23, p. 159–177, 1991.

[120] GUO, J. K.; MERONEY, R. N. Theoretical solution for laminar flow in partially-filled pipes. *Journal of Hydraulic Research*, v. 51, n. 4, p. 408–416, 2013.

[121] FULLARD, L. A.; WAKE, G. C. An analytical series solution to the steady laminar flow of a Newtonian fluid in a partially filled pipe, including the velocity distribution and the dip phenomenon. *IMA Journal of Applied Mathematics*, v. 80, n. 6, p. 1890–1901, 2015.

[122] NG, H. C.-H. et al. Partially filled pipes: experiments in laminar and turbulent flow. *Journal of Fluid Mechanics*, v. 848, p. 467–507, 2018.

[123] ROHSENOW, W. M.; HARTNETT, J. P.; CHO, Y. I. *Handbook of Heat Transfer*. 3. ed. New York: McGraw-Hill, 1998.

[124] MUZYCHKA, Y. S.; YOVANOVICH, M. M. Pressure drop in laminar developing flow in noncircular ducts: A scaling and modeling approach. *Journal of Fluids Engineering*, v. 131, p. 111105, 2009.

[125] MORTENSEN, N. A.; OKKELS, F.; BRUUS, H. Reexamination of Hagen–Poiseuille flow: Shape dependence of the hydraulic resistance in microchannels. *Physical Review E*, v. 71, n. 5, p. 057301, 2005.

[126] BAHRAMI, M.; YOVANOVICH, M. M.; CULHAM, J. R. A novel solution for pressure drop in singly connected microchannels of arbitrary cross-section. *International Journal of Heat and Mass Transfer*, v. 50, n. 13–14, p. 2492–2502, 2007.

[127] SOKOLNIKOFF, I. S.; SOKOLNIKOFF, E. S. Torsion of regions bounded by circular arcs. *Bulletin of the American Mathematical Society*, v. 44, p. 384–387, 1938.

[128] GREENWELL, R. N.; WANG, C. Y. Fluid flow through a partially filled cylinder. *Applied Scientific Research*, v. 36, n. 1, p. 61–75, 1980.

[129] ABRAMOWITZ, M.; STEGUN, I. A. *Handbook of Mathematical Functions*. New York: Dover Publications, 1964. Dover Edition, 1964.

[130] FINCH, S. R. *Mathematical Constants*. Cambridge: Cambridge University Press, 2003. 232–233 p.

[131] MAPLESOFT. *Maple*. Version 2025.1. Waterloo, ON, 2025.

[132] WOLFRAM RESEARCH, INC. *Mathematica*. Version 14.3. Champaign, IL, 2025.

[133] PYTHON SOFTWARE FOUNDATION. *Python Language Reference*. Version 3.14.0. [S.l.], 2025.

[134] The mpmath developers. *mpmath: a Python library for arbitrary-precision floating-point arithmetic*. 2023. Version 1.3.0.

[135] YU, M.; MODESTI, D.; PIROZZOLI, S. Direct numerical simulation of flow in open rectangular ducts. *Journal of Fluid Mechanics*, v. 977, p. A32, 2023.

[136] KAYA, K.; ÖZCAN, O. An approximate analytic solution of uniform laminar flow in a circular open channel. *Journal of the Brazilian Society of Mechanical Sciences and Engineering*, v. 43, p. 328, 2023.

[137] HECHT, F. New development in FreeFem++. *Journal of Numerical Mathematics*, v. 20, n. 3–4, p. 251–265, 2012.

[138] ANDRIANOV, I.; SHATROV, A. Padé approximants, their properties, and applications to hydrodynamic problems. *Symmetry*, v. 13, n. 10, p. 1869, 2021.

[139] DRAZIN, P. G.; RILEY, N. *The Navier-Stokes equations: A Classification of Flows and Exact Solutions*. [S.l.]: Cambridge University Press, 2006.

[140] WANG, C. Y. Exact solutions of the unsteady Navier-Stokes equations. *Applied Mechanics Reviews*, v. 42, 1989.

[141] JOG, M. A. *Fluid Mechanics: Fundamentals and Applications*. Cambridge: Cambridge University Press, 2015. ISBN 9781107074704.

[142] BERKER, R. Intégration des équations du mouvement d'un fluide visqueux incompressible. In: FLüGGE, S. (Ed.). *Handbuch der Physik*. Berlin: Springer, 1963. v. 3, p. 1–384.

[143] LEKNER, J. Laminar flow in epicycloidal corrugated pipes. *Zeitschrift für Angewandte Mathematik und Mechanik*, Wiley, v. 102, n. 12, p. e202100352, 2022.

[144] BACELAR, M. D. et al. Hagen-Poiseuille flow in a quarter-elliptic tube. *Fluids*, v. 8, n. 9, 2023. ISSN 2311-5521.

[145] SZYMANSKI, P. Quelques solutions exactes des equations de l'hydrodynamique du fluide visqueux dans le cas d'un tube cylindrique. *Journal de Mathématiques Pures et Appliquées*, v. 11, p. 67–107, 1932.

[146] MUELLER, W. Zum problem der Anlaufströmung einer Flüssigkeit im geraden Rohr mit Kreisring und Kreisquerschnitt. *Zeitschrift für Angewandte Mathematik und Mechanik*, v. 16, p. 227–238, 1936.

[147] ERDOğAN, E. On the flows produced by sudden application of a constant pressure gradient or by impulsive motion of a boundary. *International Journal of Non-linear Mechanics*, v. 38, p. 781–797, 07 2003.

[148] ERDOĞAN, M. E.; İMRAK, C. E. Effects of the side walls on starting flows in ducts. *International Journal of Non-Linear Mechanics*, Elsevier, v. 40, n. 1, p. 103–111, 2005.

[149] WANG, C. Y. Unsteady flow in a circular sector duct. *International Journal of Non-Linear Mechanics*, v. 46, n. 1, p. 291–295, 2011. ISSN 0020-7462.

[150] WANG, C. Y. Exact solutions for starting and oscillatory flows in an equilateral triangular duct. *Journal of Fluids Engineering*, v. 138, n. 8, p. 084503, 05 2016. ISSN 0098-2202.

[151] WANG, C. Y. Starting flow in regular polygonal ducts. *Fluid Dynamics Research*, IOP Publishing, v. 48, n. 3, p. 035505, 2016.

[152] WANG, C. Y. Starting flow in an elliptic duct. *International Journal of Fluid Mechanics Research*, v. 45, n. 2, p. 163–170, 2018. ISSN 2152-5102.

[153] WANG, C. Unsteady flow in a flattened tube. *European Journal of Mechanics - B/Fluids*, v. 82, p. 47–53, 2020. ISSN 0997-7546.

[154] WANG, C. Y. Starting flow in regular polygonal ducts. *Fluid Dynamics Research*, IOP Publishing, v. 48, n. 3, p. 035505, may 2016.

[155] RAY, S.; MISRA, D. Laminar fully developed flow through square and equilateral triangular ducts with rounded corners subjected to H1 and H2 boundary conditions. *International Journal of Thermal Sciences*, v. 49, n. 9, p. 1763–1775, 2010. ISSN 1290-0729.

[156] KU, D. N. Blood flow in arteries. *Annual Review of Fluid Mechanics*, v. 29, n. 1, p. 399–434, 1997.

[157] TABALVANDANI, A. H. et al. A general analytical solution for fluid flow and heat convection through arbitrary-shaped triangular ducts: A variational analysis. *Heliyon*, Elsevier, v. 10, n. 4, p. e25293, 2024.

[158] KOSE, D.; SAHIN, B.; YILMAZ, M. Parametric study and optimization of microchannel heat sinks with various shapes. *Applied Thermal Engineering*, Elsevier, v. 212, p. 118368, 2022.

[159] MORSE, P. M.; FESHBACH, H. *Methods of Theoretical Physics*. New York: McGraw-Hill, 1953.

[160] WANG, C. Y.; WANG, C. *Structural Vibration: Exact Solutions for Strings, Membranes, Beams, and Plates*. [S.l.]: CRC Press, 2013.

[161] MCCARTIN, B. J. On polygonal domains with trigonometric eigenfunctions of the Laplacian under Dirichlet or Neumann boundary conditions. *Applied Mathematical Sciences*, v. 2, n. 58, p. 2891–2901, 2008.

[162] WAKASUGI, S. Bucklng of a simply supported triangular plate having inner angles of 30, 60 and 90 degrees. *Bulletin of JSME*, v. 4, n. 13, p. 16–20, 1961.

[163] AGGARWALA, B. D.; IQBAL, M. On limiting Nusselt numbers from membrane analogy for combined free and forced convection through vertical ducts. *International Journal of Heat and Mass Transfer*, Elsevier, v. 12, n. 6, p. 737–748, 1969.

[164] SETH, B. R. Motion of a liquid contained in rotating cylinders of triangular cross-section. *The Quarterly Journal of Mathematics*, Oxford University Press, n. 1, p. 161–171, 1934.

[165] HAY, G. E. The method of images applied to the problem of torsion. *Proceedings of the London Mathematical Society*, Oxford University Press, v. 2, n. 1, p. 382–397, 1939.

[166] TSANGARIS, S.; VLACHAKIS, N. W. Exact solution of the Navier-Stokes equations for the oscillating flow in a duct of a cross-section of right-angled isosceles triangle. *Zeitschrift für Angewandte Mathematik und Physik*, v. 54, n. 6, p. 1094–1100, 2003.

[167] PROUDMAN, J. Notes on the motion of viscous liquids in channels. *The London, Edinburgh, and Dublin Philosophical Magazine and Journal of Science*, Taylor & Francis, v. 28, n. 163, p. 30–36, 1914.

[168] RAMACHARYULU, N. C. P. *A non-Darcian approach to flows through porous media*. [S.l.], 1976.

[169] NARASIMHACHARYULU, V.; PATTABHIRAMACHARYULU, N. C. Steady flow of a viscous liquid in a porous elliptic tube. *Proceedings of the Indian Academy of Sciences – Section A*, v. 87, n. 2, p. 79–83, 1978.

[170] WANG, C. Y. Analytical solution for forced convection in a semi-circular channel filled with a porous medium. *Transport in Porous Media*, v. 73, n. 3, p. 369–378, 2008.

[171] WANG, C. Y. Analytical solution for forced convection in a sector duct filled with a porous medium. *Journal of Heat Transfer*, v. 132, n. 8, p. 084502, 06 2010.

[172] WANG, C. Y. Closed-form Nusselt numbers for ducts filled with porous medium. *Journal of Thermophysics and Heat Transfer*, American Institute of Aeronautics and Astronautics, v. 31, n. 2, p. 478–482, 2017.

[173] ALASSAR, R. S.; ABUSHOSHAH, M. Hagen–Poiseuille flow in semi-elliptic microchannels. *Journal of Fluids Engineering*, ASME, v. 134, n. 12, p. 124502, 2012.

[174] WANG, C. Y. On viscous flow in semi-elliptic ducts. *Journal of Fluids Engineering*, American Society of Mechanical Engineers Digital Collection, v. 137, n. 11, p. 114502, 2015.

[175] LOPES, A. B.; SIQUEIRA, I. Couette–Poiseuille flow in semi-elliptic channels. *Journal of Fluids Engineering*, American Society of Mechanical Engineers, v. 144, n. 10, p. 101302, 2022.

[176] HAJI-SHEIKH, A.; VAFAI, K. Analysis of flow and heat transfer in porous media imbedded inside various-shaped ducts. *International Journal of Heat and Mass Transfer*, v. 47, n. 8, p. 1889–1905, 2004. ISSN 0017-9310.

[177] WANG, C. Y. Flow through super-elliptic ducts filled with a Darcy–Brinkman medium. *Transport in Porous Media*, Springer, v. 81, n. 2, p. 207–217, 2010.

[178] LAMB, H. *Hydrodynamics*. 6. ed. Cambridge: Cambridge University Press, 1932.

[179] ABRAMOWITZ, M.; STEGUN, I. A. *Handbook of Mathematical Functions with Formulas, Graphs and Mathematical Tables*. [S.l.]: Dover Publications, 1965.

[180] MCLACHLAN, N. W. *Theory and Application of Mathieu Functions*. London: Oxford University Press, 1947.

[181] BIBBY, M. M.; PETERSON, A. F. *Accurate Computation of Mathieu Functions*. [S.l.]: Springer, 2014. 123 p. (Synthesis Lectures on Computational Electromagnetics, v. 1). ISBN 978-3-031-00589-3.

[182] CELIK, I. B. et al. Procedure for estimation and reporting of uncertainty due to discretization in cfd applications. *Journal of Fluids Engineering*, v. 130, n. 7, p. 078001, 07 2008. ISSN 0098-2202.

[183] GEUZAINE, C.; REMACLE, J.-F. Gmsh: A 3-d finite element mesh generator with built-in pre- and post-processing facilities. *International Journal for Numerical Methods in Engineering*, v. 79, n. 11, p. 1309–1331, 2009. Disponível em: <https://onlinelibrary.wiley.com/doi/abs/10.1002/nme.2579>.

[184] GMATI, I. E. et al. A novel 3-d-printed passive microfluidic temperature sensor for medical applications. *IEEE Transactions on Components, Packaging and Manufacturing Technology*, v. 15, n. 7, p. 1432–1445, 2025.

[185] GALVIS, A. F. Phase-field modelling of quasi-static and dynamic brittle fracture: A freefem++ implementation. *Engineering Fracture Mechanics*, Elsevier, p. 111846, 2026.

[186] VILLA-MORALES, J. Spectral bounds and exit times for a stochastic model of corruption. *Mathematical and Computational Applications*, v. 30, n. 5, 2025. ISSN 2297-8747. Disponível em: <https://www.mdpi.com/2297-8747/30/5/111>.

[187] BAO, F.; LIN, J.; SHI, X. Burnett simulation of flow and heat transfer in micro couette flow using second-order slip conditions. *Heat and mass transfer*, Springer, v. 43, n. 6, p. 559–566, 2007.

[188] DAMEAN, N.; REGTIEN, P. A study of fluid flow in a mems designed for the determination of fluid and flow characteristics. In: *Proceedings of the 17th IEEE Instrumentation and Measurement Technology Conference [Cat. No. 00CH37066]*. [S.l.: s.n.], 2000. v. 2.

[189] SUN, X.; WANG, S.; ZHAO, M. Oscillatory flow of Maxwell fluid in a tube of isosceles right triangular cross section. *Physics of Fluids*, AIP Publishing, v. 31, n. 12, p. 123106, 2019.

[190] GIACOMIN, A. J. et al. Viscous heating in large-amplitude oscillatory shear flow. *Physics of Fluids*, AIP Publishing, v. 24, n. 10, p. 103101, 2012.

[191] MORINI, G. L. Viscous heating in liquid flows in micro-channels. *International Journal of Heat and Mass Transfer*, v. 48, n. 17, p. 3637–3647, 2005. ISSN 0017-9310. Disponível em: <https://www.sciencedirect.com/science/article/pii/S0017931005000888>.

[192] RAY, S.; MISRA, D. Laminar fully developed flow through square and equilateral triangular ducts with rounded corners subjected to h1 and h2 boundary conditions. *International Journal of Thermal Sciences*, v. 49, n. 9, p. 1763–1775, 2010. ISSN 1290-0729. Disponível em: <https://www.sciencedirect.com/science/article/pii/S1290072910000840>.

[193] JAVADPOUR, F. Nanopores and apparent permeability of gas flow in mudrocks (shales and siltstone). *Journal of Canadian Petroleum Technology*, OnePetro, v. 48, n. 08, p. 16–21, 2009.

[194] BAHRAMI, M.; TAMAYOL, A.; TAHERI, P. Slip-flow pressure drop in microchannels of general cross section. *Journal of Fluids Engineering*, ASME, v. 132, n. 11, p. 111201, 2010.

[195] PENG, Z.-C.; LU, X.-J. Nanoscale air bearing modeling via lattice boltzmann method. *IEEE Transactions on Magnetics*, IEEE, v. 49, n. 6, p. 2537–2542, 2013.

Appendix A

Codes

A.1 Poiseuille flow through parabolic segment and lens-shaped ducts

```
for (real alpha = 0.5; alpha <= 2.0; alpha+=0.001){

// Parameters
func f = 1.;
cout.precision(10);
alpha = 1/alpha;

// Mesh
int out = 1;

border C01(t=-1, 1){x=t; y=-(t^2-1)*alpha; label=out;}
border C02(t=-1, 1){x=-t; y=(t^2-1)*alpha; label=out;}

int n11 = 2500 - 1000*pow(alpha,0.15);

mesh Th = buildmesh(C01(-n11) + C02(-n11));
plot(Th);

// Fespace
func Pk = P2;
fespace Uh(Th, Pk);
Uh u;

// Macro
macro grad(A) [dx(A), dy(A)] //

// Problem
varf vPoisson (u, uh)
  = int2d(Th)(grad(u)' * grad(uh))
  + int2d(Th)(f * uh)
```

```
  + on(out, u=0)
  ;
matrix<real> Poisson = vPoisson(Uh, Uh, solver=sparsesolver);
real[int] PoissonBoundary = vPoisson(0, Uh);
u[] = Poisson^-1 * PoissonBoundary;
plot(u);

// Plot
Uh ff = 1;
real perim = int1d(Th,1)(ff);
real vaz= int2d(Th)(u);
real areaa= int2d(Th)(ff);
real fre= 8*areaa^3/perim^2/vaz;
real maxi = u[].max;

cout << alpha << " " << maxi << " " << vaz/areaa << " " << fre << endl;
}
```

Listing A.1: FreeFEM implementation of the parabolic segment and lens-shaped ducts.

A.2 Revisiting Poiseuille flow through lens-shaped and figure-eight ducts

```
for (real degrees = 120.3; degrees <= 179.8; degrees += 3.1) {
// Parameters
func f = 1.;
cout.precision(13);

real alpha = degrees*pi/180;
real ca = cos(alpha);
real sa = sin(alpha);

border C01(t = pi, alpha)
{
    x = sin(t)/sa;
    y = (-ca + cos(t))/sa;
    label = 1;
}

real ytop = (-ca - 1)/sin(alpha);

border C02b(s = 1,0)
{
    x = 0;
    y = ytop*(1 - s);
    label = 3;
}
```

```
25
26 border C02a(s = 1,0)
27 {
28     x = 0 + sa*s/sin(alpha);
29     y = 0;
30     label = 2;
31 }
32
33 int nn = 20;
34 mesh Th = buildmesh(
35       C01(nn)
36     + C02b(nn)
37     + C02a(nn)
38 );
39
40 // Fespace
41 func Pk = P2;
42 fespace Uh(Th, Pk);
43 Uh u;
44
45 // Macro
46 macro grad(A) [dx(A), dy(A)] //
47 // Problem
48 varf vPoisson (u, uh)
49   = int2d(Th)(grad(u)' * grad(uh))
50   + int2d(Th)(f * uh)
51   + int1d(Th,2)(uh*0)
52   + int1d(Th,3)(uh*0)
53   + on(1, u=0)
54   ;
55 matrix<real> Poisson = vPoisson(Uh, Uh, solver=sparsesolver);
56 real[int] PoissonBoundary = vPoisson(0, Uh);
57 u[] = Poisson^-1 * PoissonBoundary;
58
59 //Post-processing
60 real maxi = u[].max;
61 int idx = u[].imax;
62 Uh cx = x, cy = y;
63 real xatmax = cx[](idx);
64 real yatmax = cy[](idx);
65
66 Uh ff = 1;
67 real perim = int1d(Th,1)(ff);
68 real vaz= int2d(Th)(u);
69 real areaa= int2d(Th)(ff);
70 real fre= 8*areaa^3/perim^2/vaz;
71
72 // Plot
73 cout << " "  << degrees << " " << areaa << " " << perim << " " << maxi <<
```

```
    " " << vaz << " " << fre << " coord = (" << xatmax << ", " << yatmax
   << ")" << endl;
plot(u, nbiso=10, fill=false, value=true, cmm="A",wait=0);
}
```

Listing A.2: FreeFEM implementation of the lens-shaped and figure-eight Poiseuille problem.

A.3 Startup of Poiseuille flow in triangular ducts

```
// Parameters
cout.precision(9);
func f = 1.;
real dt = 0.001;
real t0 = 0;
real tf = 0.200;

// Mesh
int out = 1;

//Hemi
border C01(t=0, 1){x=1-t; y=0; label=1;}
border C02(t=0, 1){x=1; y=(1-t)/sqrt(3); label=1;}
border C03(t=0, 1){x=t; y=t/sqrt(3); label=1;}

int nn = 50;

plot(C01(-nn) + C02(-nn) + C03(-nn), wait=false);
mesh Th = buildmesh(C01(-nn) + C02(-nn) + C03(-nn));

// Fespace
func Pk = P2;
fespace Uh(Th, Pk);
Uh u = t0, v, uold;

// Macro
macro grad(A) [dx(A), dy(A)]

// Problem
problem vPoisson (u, v)
  = int2d(Th)(u*v/dt + grad(u)' * grad(v))
  - int2d(Th)(f * v)
  - int2d(Th)(uold*v/dt)
  + on(1, u=0);

Uh ff = 1;
real perim = int1d(Th,1)(ff);
real area = int2d(Th)(ff);
```

```
real fre;
real vaz;

for(real t = 0; t < tf; t += dt)
{

uold = u;
vPoisson;
plot(u);

real maxu = u[].max;
vaz = int2d(Th)(u);
fre = 8*area^3/perim^2/vaz;
cout << t << " " << vaz << " " << fre << " " << maxu << endl;

}

// Shear
real shear1 = int1d(Th,1)( -(dx(u)*N.x + dy(u)*N.y) );
real shear2 = int1d(Th,2)( -(dx(u)*N.x + dy(u)*N.y) );
real shear3 = int1d(Th,3)( -(dx(u)*N.x + dy(u)*N.y) );

cout << (shear1+shear2+shear3)/(perim) << endl;
```

Listing A.3: FreeFEM implementation of the transient Poisson problem.

A.4 Revisiting Darcy–Brinkman flow through an elliptic tube

```
for (real s = 20; s<=100; s=s+1){
for (int n=16; n<=512; n = n*2){

// Parameters
func f = 1.;
real alpha = 1.;
real b = 0.5;
cout.precision(15);

// Mesh
real x0 = 0;
real x1 = atanh(b);
real y0 = 0;
real y1 = pi/2;

int[int] lab = [1,2,3,4];
mesh Th = square(n, n, [x0+(x1-x0)*x, y0+(y1-y0)*y], label = lab);

```

```
19 // Fespace
20 func Pk = P2;
21 fespace Uh(Th, Pk);
22 Uh u,uh;
23
24 // Macro
25 macro grad(A) [dx(A), dy(A)] //
26 func coef = (1.0 - b*b)/2*(cosh(2*x) - cos(2*y));
27
28 // Problem
29 problem vPoisson (u, uh)
30   = int2d(Th)((grad(u)' * grad(uh)))
31   - int2d(Th)(coef * uh)
32   + int2d(Th)(coef * (s^2)*u*uh)
33   + int1d(Th,1)(uh*0)
34   + int1d(Th,3)(uh*0)
35   + int1d(Th,4)(uh*0)
36   + on(2, u=0)
37   ;
38
39 vPoisson;
40 // Plot
41 real vaz = int2d(Th)(u*(1-b^2)*2*(cosh(2*x)-cos(2*y)));
42 real areaa = pi*b;
43 real h = pow(1-b,2)/pow(1+b,2);
44 real perim = pi*(1+b)*(1 + 3*h/(10 + sqrt(4 - 3*h)));
45 real fre = 8*areaa^3/perim^2/vaz;
46 real maxi = u[].max;
47
48 // Plot
49
50 cout << n << " " << b << " " << s << " " << vaz << " " << maxi << " " <<
      fre << endl;
51 plot(u, nbiso=30, fill=1, value=true, cmm="A",wait=1);
52
53 }
54 }
```

Listing A.4: FreeFEM implementation of the Darcy-Brinkman problem.